UNIVERSITY OF CALIFORNIA
Santa Barbara

Wavelength Tunable Monolithic InP Receivers and Switches for Optical Communication Systems

A Dissertation submitted in partial satisfaction
of the requirements for the degree of

Doctor of Philosophy

in

Electrical and Computer Engineering

by

Phillip Joseph Skahan

Committee in Charge:

Professor Daniel J. Blumenthal, Chair

Professor John E. Bowers

Professor Larry A. Coldren

Dr. Douglas M. Baney

September 2016

The Dissertation of Phillip Joseph
Skahan is approved:

Professor John E. Bowers

Professor Larry A. Coldren

Dr. Douglas M. Baney

Professor Daniel J. Blumenthal, Committee Chairperson

September 2016

Wavelength Tunable Monolithic InP Receivers and Switches for Optical Communication Systems

by

Phillip Joseph Skahan

This dissertation is dedicated to my family: Kevin, Mary, Denise, Caroline, and Rachel, for always pushing me to do my best.

Acknowledgements

My experience in the graduate engineering program at UCSB has shaped my professional and personal approach more than any other point in my life, and I am eternally grateful for it. The experience in independent analysis of complex, multifaceted engineering problems has made me not only a better engineer, but a better individual as well, and there are many people I have to thank for their input and support along the way.

First I must thank Professor Dan Blumenthal for inviting me to join his research group at UCSB and providing a wealth of interesting research projects for me to work on during my time here. His enthusiasm for cutting edge research in the field of photonics always got me excited about the work I was doing and drove me to come to UCSB in the first place, and his continuous belief in my potential and subsequent motivation along the way drove me to achieve what I have.

Along with Dan, the rest of my committee members provided invaluable feedback and support towards my dissertation. Dr. Doug Baney in particular was invaluable for his patience, guidance, and support of the coherent receiver project. His continuous feedback gave much needed direction and focus on key aspects of the device, and his suggestions were always helpful towards solving particular problems. Professor John Bowers was a steady presence whose grounded viewpoint and

practical insight made vital aspects of my work much clearer to identify and understand. The foundational knowledge provided through coursework provided by Professor Larry Coldren and feedback on fundamental device characteristics and design contributed greatly to my understanding of photonic devices.

One of the best parts of being a graduate student at UCSB was the close interaction other researchers both in and out of the photonics groups. I am thankful for older students in the OCPN group such as John Garcia and Demis John who served as mentors early on as well as my predecessor on the coherent receiver project, Kim Nguyen, who got me started on characterization, processing, and simulation and laid the groundwork for the coherent receiver 2.0. I must also thank several other photonics students including Wenzao Li for his valuable insight into coherent link characterization; Sarat Gundavarapu, the automation master, for his assistance with testing; Michael Davenport for his insight into process engineering; Daryl Spencer and Molly Piels for their lab expertise; Renan Moreira and his wife Julie Hoy Moreira for BBQs and coffee; and of course my groupmate/roommate Michael Belt for providing everything from technical discussions to sous-vide meatstravaganzas as well as being the best housemate I've ever had.

Others who have made a significant impact on my educational experience include former postdocs Jon Barton, Henrik Paulsen, and Milan Mašanović; undergraduate researcher Alex So; the UCSB cleanroom staff, including Adam Abrahamsen, Brian

Thibault, Bill Mitchell, Don Freeborn, Tony Bosch, Aidan Hopkins, Brian Lingg, Tom Reynolds, Mike Silva, and especially Biljana Stamenic for countless processing Q+A sessions;, Bowers group members Minh Tran, Alan Liu, Jock Bovington, Siddharth Jain, Geza Kurczveil, Jared Bauters, Sudha Srinivasan, Alex Spott, Tin Komljenovic, and Martijn Heck; Coldren group members Mingzhi Lu, Abi Sivananthan, and John Parker; and other classmates/cleanroom colleagues Steven Weinecke, Matt Laurent, Prateek Choudhary, Ludovico Megalini, Sang Ho Oh, and Joe Nedy.

I can't conclude the acknowledgements section without mentioning all of my friends and 'family' from the ballroom dance class and Cotillion Dance Club at UCSB. Their dance events and competition team were a much-needed outlet for de-stressing as well as personal development and social interaction, and they introduced me to an extracurricular activity that I will pursue for the rest of my life. These include fellow ballroom class TAs Miny, Hannah, Celeste, Michael, Alyssa and Andrew; competition partners Jeannin, Elena, Ariadne, and Letitia; and far too many fellow competitors and social dance partners to name.

Finally, to my family for all of their enthusiasm and support towards me not only moving to Santa Barbara but also advancing my studies so far: I would never have gotten this far without your love and help. Thank you to my parents, Mary and Kevin, for their yearly visits; thank you to my sisters, Denise, Caroline, and Rachel, for each making it out once but always staying in the loop; and thank you to my grandparents, Charles and Virginia Seiter, for being my inspiration in life and celebrating my accomplishments every step of the way.

Curriculum Vitae

Phillip Joseph Skahan

Education

2016	Doctor of Philosophy in Electrical and Computer Engineering, University of California, Santa Barbara
2011	Master of Science in Electrical and Computer Engineering, University of California, Santa Barbara
2010	Bachelor of Science in Electrical and Computer Engineering, University of Tennessee, Knoxville

Experience

2010-2015	Graduate Research Assistant, U. C. Santa Barbara
2009-2010	Undergraduate Research Assistant, University of Tennessee, Knoxville

Journal Publications

Skahan, P. J., Gundavarapu, S., Nguyen, K. N., Baney, D. M., Blumenthal, D. J., "Monolithically integrated dual-channel coherent receiver with widely tunable local oscillator for 100 Gbps DP-QPSK applications." Opt. Lett. **40(**18), 4313-4316 (2015). DOI: 10.1364/OL.40.004313

Nguyen, K. N., **Skahan, P. J.**, Garcia, J. M., Lively, E., Poulsen, H. N., Baney, D. M., Blumenthal, D. J., "Monolithically integrated dual-quadrature coherent receiver on InP with 30 nm tunable SG-DBR local oscillator," Opt. Express **19**(26), B716-B721 (2011). DOI: 10.1364/OE.19.00B716

Abstract

Wavelength Tunable Monolithic InP Receivers and Switches for Optical Communication Systems

Phillip Joseph Skahan

Demand for information technology continues to grow, and with it the need for continuous improvement in telecommunication infrastructure. Recent interest in coherent modulation schemes, wavelength conversion, and large scale photonic integration for feasible, cost-effective scaling of existing network infrastructure has generated an intriguing area idea in which several technologies are combined at once to create a solution more capable than any individual approach. By leveraging these technologies together, a scalable path capable of providing sustainable growth in the telecommunication field may be realized.

This dissertation explores this concept by the applying principles of monolithic integration to coherent receiver and optical switch technology with the goal of improving the size, cost, and performance of existing communication components as well as drive forward the state of the art in photonic integration. To this end, a monolithic coherent receiver was developed by integrating local oscillator, mixer, and high speed detection functions together on a single chip in an architecture capable of supporting polarization multiplexing and phase shift keying modulation

formats. With an integrated local oscillator, the receiver's capability is scalable, supporting higher capacity modulation formats through the use of more advanced feedback electronics and digital signal processing.

In addition, a monolithic all-optical switch was developed by integrating both wavelength conversion and wavelength filtering functions onto a single chip. The architecture is capable of high speed switching of optical signals without costly optical-electrical conversion by utilizing an array of optical-optical modulators with scalable channel capacity and a static arrayed-waveguide grating router. By integrating these functions on the same chip, costly packaging issues may be avoided, greatly reducing development and production costs.

By moving an increased number of components onto single die while maintaining similar performance to discrete solutions, the coherent receiver and all-optical switch devices presented in this work advance the state of the art by improving the cost and manufacturability of optical communication devices. Even more, these technologies represent a path toward manageable growth of optical communication systems for long haul, datacenter, and short reach solutions by demonstrating scalable architectures for each application. Development of such technology is not only vital but essential for the continued growth of the telecommunications industry. The novel application of photonic integration, coherent modulation, and optical switching technologies are a viable solution to maintaining sustainable growth in the telecommunications field.

Contents

Appendices

Chapter 1

Introduction

1.1 Background

The advent of Internet technology has fundamentally changed the way we interact with the world. Long distance communication based on fiber optic cabling have enabled cheap and seamless communication between individuals across the globe, accelerating human development through the exchange of ideas. Underlying this fundamental shift is the rise of optical communications as a viable solution to the transfer of information. Over the past 30 years, most of this growth has been driven by advancements in discrete optical components such as high quality laser sources and photodiodes and improved fiber optic cable properties.

To continue this growth in to the 21st century, telecommunication research and development has begun to look beyond the continuous improvement of discrete components to the development of larger-scale integrated optical systems. This shift has largely come about due to projected growth in demand for high-performance optical communication systems beyond traditional long-haul applications where they are most commonly used today. In datacenters, an industry dominated by multi-mode fiber, LEDs, and VCSEL sources, increasing capacity requirements have begun to generate demand for more advanced optical systems capable of handling increased data loads. Beyond data communications, server manufacturers have begun to investigate optical systems for on-board communications in parallel computing applications where transmission capacity and power dissipation exceed the limits of electrical wiring. Regardless of whether these developments continue in the short-term, it remains clear that there remains substantial opportunity for advancement and application in this field making its research investment worthwhile.

In the past several years the increase in demand on internet service providers has been substantial and continues to grow. According to the Cisco Visual Networking Index, annual global IP traffic will reach 2 zettabytes by the year 2019, representing a threefold increase from 2014 to 2019 for a compound annual growth rate of 23 percent, driven by video on demand and on-demand gaming resulting from increased adaptation of personal smartphones and tablets as well as traditional television service with ultra-high definition formats [1]. On-demand video streaming providing high-definition content such as Netflix, YouTube, and Amazon Prime have quickly becoming the most popular form of media delivery, driving bandwidth consumption. Additionally, teleconferencing and telecommuting for business applications are contributing to the increased load as well as cloud services which utilize mobile technology to monitor everyday activity. This demonstrates that the market for optical communications will continue to grow, relying on technological advancements for improved network capabilities to do so.

Two particular areas which have seen great interest over the past several years and could potentially transform the optical communications industry are wavelength conversion and coherent encoding schemes. The work in this thesis explores these two technologies aimed at the improvement of optical network efficiency and cost-effectiveness through the development of an all-optical switch and coherent optical receiver with all components monolithically integrated onto a single chip. By monolithically integrating all components required, the manufacturing costs can be greatly reduced, making advanced systems more viable.

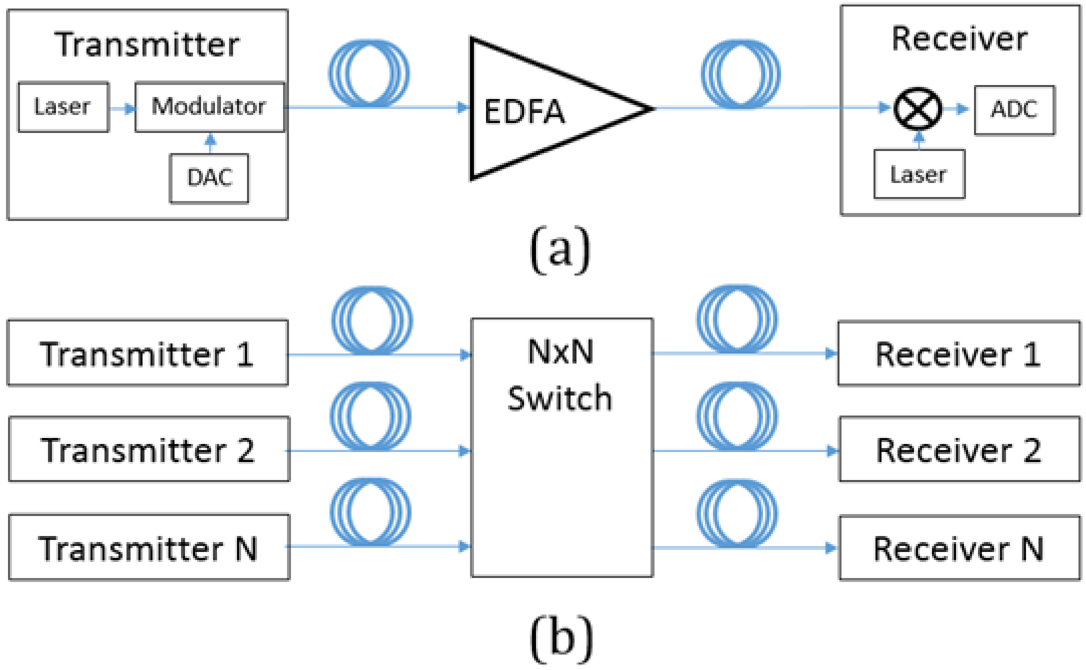

Figure 1.1. System diagrams of (a) a coherent transmission link and (b) an all-optical switch node.

1.2 Coherent Receivers

Optical transmission systems based on coherent communication schemes have recently become of great interest due to their inherent advantages over direct detection. These systems are theoretically capable of providing excellent receiver characteristics including best theoretical sensitivity, high spectral efficiency, and longest transmission distances making them suitable for both free space and fiber applications [2].

Initial research into coherent schemes from the 1980s through the 1990s focused on increasing link distance by maximizing the receiver sensitivity and typically operated with an optical phase-lock loop and local oscillator [2]. This focus fell to the wayside as wavelength division multiplexing (WDM) systems using erbium doped fiber amplifiers (EDFAs) and receiver pre-amplifiers made other methods for increasing link distance and sensitivity largely irrelevant [2].

Renewed interest in coherent receivers was sparked by research into self-heterodyned differential phase-shift keying (DPSK) using a delay interferometer to allow a signal to reference itself to recover the phase information, eliminating the need for a local oscillator. These systems are particularly useful for situations where pre-amplifiers are impractical, such as deep space communications or for wavelengths at which viable amplifiers do not exist [2]. Recovery of the phase component of the incoming wave also enables full recovery of the electric field information, which can be digitally manipulated to improve tolerance to optical nonlinearities induced in a fiber [2]. Finally, phase shift keying includes an inherent filtering function in the down mixing process providing superior channel selectivity to typical WDM filters and allow for dynamic network allocation through the use of a tunable local oscillator [2]. These advantages make phase shift keying a suitable candidate for improved network infrastructure utilization.

Since most of these improvements are realized post-transmission, receiver technology has received the largest development focus in coherent systems. This has been enabled as digital signal processing (DSP) electronics have become mature enough for real-time compensation of fiber nonlinearities. DSP technology has long been utilized in wireless and DSL systems where orthogonal frequency division multiplexing (OFDM) and multiple-input and multiple-output (MIMO) encoding schemes have greatly improved the spectral efficiency to make use of their limited bandwidth [3], and optical transmission systems are a logical next step for its application.

1.2.1 Receiver Requirements

There are several design aspects which are important for a coherent receiver; these are detailed in Table 1.1 alongside performance goals and associated components. First, the linewidth of the local oscillator should be minimized to reduce phase noise that causes signal degradation. Its wavelength must also be stable to enable maximum spectral efficiency through narrowband filtering and with minimal guard bands to avoid channel cross-talk. To maximize receiver sensitivity, the loss in the passive functions of the device such as the polarization splitters and signal mixers must be minimized, and the photodetectors should be designed for maximum responsivity. For flexible allocation of available fiber spectrum, both the local oscillator and photodiode should have a wide operating wavelength window that can be quickly re-allocated, and the photodiode's response time should be minimized for compatibility with high signal clock speeds. Additional design goals include polarization diversity, allowing any polarization state to be recovered by the receiver, greatly reducing system complexity and fiber cost, as well as low power consumption, minimal size, and low cost for commercial adaptation, all of which are enabled by monolithic integration.

Table 1.1. Attributes of a monolithically integrated coherent receiver with performance goals and contributing components for a 100 Gbps 100GBASE-ZR compatible receiver [4].

Design Attribute	Performance Goal	Contributing Component(s)
Linewidth	< 10 MHz [5]	Local Oscillator
Wavelength	± 0.1 nm	Local Oscillator
Wavelength Range	> 40 nm	Local Oscillator
Sensitivity	-20 dBm [4]	Photodiodes, Hybrids, Amplifiers, Local Oscillator
Bandwidth	> 25 GHz	Photodiodes
Power Dissipation	< 1 W	Amplifiers, Local Oscillator
Physical Size	< 5 mm^2	Hybrids, Local Oscillator

1.2.2 State of the Art

Until recently, coherent receivers consisted of bulk optic solutions with separate laser local oscillator, polarization beam splitter, 90° optical hybrids, and photodiodes. Recently, however, several examples of monolithically integrated coherent receivers have been developed particularly on the InP substrate; these are compared in Table 1.2. Receiver design has focused in particular on achieving

100 Gbps operation on a single chip which is the general limit of contemporary DSP electronics. The PICs typically include on- or off-chip polarization demultiplexing, 90° optical hybrids, and balanced photodiodes but tend to utilize an off-chip local oscillator due to the difficulty of designing an epitaxial structure featuring layers with both a high absorption coefficient for optimized photodiodes as well as high gain for lasers [6-12]. Several examples exist with on-chip local oscillators, including one with a 10 channel array of distributed feedback (DFB) lasers for operation in a WDM system [13], a single channel receiver utilizing a sampled-grating distributed Bragg reflector (SG-DBR) laser and a second regrowth to allow for both high gain and high absorption material on a single die [14], and two more receivers with single- or dual-channels featuring an integrated SG-DBR laser and photodiodes using the same layer for gain and absorption which suffered from relatively poor RF performance in their photodiodes [15, 16]. In this thesis, we improved upon the design in [16] and were able to demonstrate the first dual-channel coherent receiver with an integrated widely tunable local oscillator and photodiodes capable of operating greater than 25 GHz fabricated using a single epitaxial structure and requiring no second regrowth. Furthermore, the integrated receiver described here demonstrates one of the largest examples of data capacity over a single wavelength for a monolithic device with 100 Gbps total theoretical single wavelength capacity as well as a wavelength range of over

40 nm. Further improvements to the local oscillator and photodiode design could scale this receiver design to quadrature amplitude modulation (QAM) operation at greater than 40 Gbaud allowing for single-wavelength data throughput beyond 320 Gbps on a DP-16QAM format.

Table 1.2. Prior art for monolithically integrated DP-QPSK receivers on InP and relevant performance metrics.

Organization [Reference]	**UCSB [16]**	**u2t [7]**	**Bell Labs [9]**	**Infinera [13]**	**Fraunhofer [6]**
Polarization Multiplexing	No	Off-chip	On-chip	Off-chip	Off-chip
Integrated Local Oscillator (Linewidth)	30 nm tunable (25 MHz)	No	No	Static DFB array (157 kHz)	No
Format	QPSK	DP-QPSK	DP-QPSK	DP-QPSK	DP-QPSK
f_{3dB}	10 GHz	26 GHz	N/A	26 GHz	50 GHz
Bitrate/Channel (per polarization)	20 Gbps	56 Gbps	43 Gbps	50 Gbps	50 Gbps
Bitrate (# of channels)	20 Gbps (1)	112 Gbps (1)	172 Gbps (4)	500 Gbps (10)	100 Gbps (1)

1.3 All-Optical Switches

All-optical switches have long been of interest for optical computing as the energy required to route a photon is theoretically much less than that of an electron. In practice, computers based on optical switches would be impractical due to the large interaction length of photons, but they have found a more suitable use in communication systems where network bandwidth exceeds that of available electronics [17]. Rather than perform costly electrical to optical (OE) conversion, switches utilizing all-optical architectures can transparently re-route data as required, reducing system complexity.

Research into all-optical switches has primarily focused on increasing switching speed and reducing power consumption as there are several different applications that become possible depending on switch rate. At millisecond response times, optical switches are suitable for network protection applications, while at nanosecond response times, all-optical packet switching using header rewrite becomes possible. In the picosecond range, switches can perform bit-by-bit data rewrites for optical time division multiplexing (OTDM) applications [18]. In addition, all-optical switches require low crosstalk and insertion loss, polarization insensitivity, bit rate and protocol transparency, and a wide operating bandwidth [18]. For network applications, it is also beneficial for switches to have a small physical footprint, large scalability, and non-blocking capability [18].

Several optical switch technologies have been explored in recent years, including those based on microelectromechanical system (MEMS) mirror arrays, thermo-optic and electro-optic waveguide switches, and acousto-optic waveguide interferometers [17]. Perhaps the most promising approaches are those based on nonlinear optical processes including four-wave mixing, cross-gain modulation, cross-phase modulation, and cross-absorption modulation. These nonlinearities occur in either fiber or semiconductor waveguides at high photon densities and allow for ultrafast switching speeds, and the relative stability and short response time of semiconductor-based nonlinear optical switches in particular have made them a prime area of research. Most of this research has focused on the use of semiconductor optical amplifiers (SOAs) to generate photon densities required for nonlinear operations as SOA converters meet not only the requirements listed above but are also scalable and non-blocking, making them a suitable candidate for all-optical networking.

1.3.1 All-Optical Switch Requirements

There are several important aspects of an all-optical switch for a packet-switching application; These are laid out in Table 1.3 following that discussed by Ma *et al.* As previously discussed, switching speed largely dictates potential applications for optical switches and is the most vital metric for switch performance. Minimal channel crosstalk on the order of 40-50 dB is desirable as well as low insertion loss to enable cascading of multiple switches. It is useful for switches to have low polarization-dependent loss to improve reliability and minimize monitoring overhead.

Table 1.3. Attributes for an SOA-based monolithically integrated all-optical switch along with performance goals and contributing components [18].

Design Attribute	Performance Goal	Contributing Component(s)
Switching Speed	< 1 ns	SOA, Local Oscillator
Channel Crosstalk	< -20 dB	Arrayed Waveguide Grating Router (AWGR)
Insertion Loss	< 5 dB	AWGR, SOA, Waveguides
Wavelength Range	> 40 nm	SOA, Local Oscillator
Bitrate/Protocol Transparent	> 40 Gbps on-off keying	SOA, MZI
Nonblocking	Yes	SOA, MZI
Power Dissipation	< 2 W	SOA, Local Oscillator
Physical Size	< 50 mm^2	AWGR, MZI, Local Oscillator

Beyond operating metrics, several more practical design goals for an all-optical switch include wide temperature stability, minimal power dissipation, and low production/operating costs [18].

1.3.2 State of the Art

Despite many technological offerings for all-optical switches in research, few have been developed into commercial offerings or even fully integrated switches devices. A table of existing technologies, performance, and progress towards commercialization is presented in Table 1.4. These include electro-optic and thermo-optic waveguide directional coupler-based switches that modulate waveguide index to control output port; liquid crystal switches that use liquid crystal modulators to switch the polarization of incoming signals and direct it through a downstream polarization beam splitter; static on/off SOA arrays; and bubble switches that use liquid to deflect light to a desired output [19]. By far the most commonly used switches today are reconfigurable add-drop multiplexers (ROADMs) consisting of tunable MEMs mirror arrays spatially directing incoming light; the speed of such devices is limited by the switching speed of the mirrors and typically on the order of milliseconds.

Table 1.4. Prior art of all-optical switch demonstrations and relevant performance metrics.

Switch Technology	Response Time	Switch Size	Channel Crosstalk	Insertion Loss
PLC Thermo-Optic [20]	4.9 ms	8x8	50.4 dB	7.4 dB
Liquid Crystal [21]	35.3 μs	2x2	< -34.13 dB	< 2 dB
SOA Array [22]	200 ps	1x8	< -12 dB	0 dB
Bubble [23]	7.7 ms	32x32	< -50 dB	3.9 dB
MEMs Mirror Array [24]	7 ms	8x8	< -50 dB	< 1.7 dB
SOA Wavelength Conversion [25]	< 100 ps	8x8	< -15 dB	Not reported

Recently, substantial research and development has been focused applying wavelength conversion to produce an all-optical switch, culminating in the demonstration of an 8x8 monolithically tunable optical router (MOTOR) capable of routing 40 Gbps data through an on-chip 8x8 arrayed waveguide grating router (AWGR) [25]. The work presented in this thesis builds upon this design by doubling the amount of input and output ports resulting in a 16x16 MOTOR chip monolithically integrating 545 optical components performing 81 discrete optical functions on a single die, making it one of the largest examples of photonic integration to date.

1.4 Photonic Integration

The work in this thesis explores the application of photonic integration to coherent receivers and all-optical switches for more advanced functionality and network scalability. Density scaling of photonic integrated circuits over the past two decades has closely resembled a Moore's Law exponential increase in complexity [26]. However, unlike in the microelectronics industry, photonics technology has remained fragmented and lacked a true driver application capable of unifying architectures under a common development platform. This has resulted in a field more closely resembling that of the analog electronics industry than that of digital electronics. Several solutions to provide a unified photonic architecture have been proposed in recent years. Smit *et al.* detailed a foundry model for integrated photonic circuits on InP using a set of standardized components and commercial foundry system to support it [26]. Heck *et al.* summarized results of hybrid III-V/silicon devices rapidly approaching device densities of existing mono-substrate platforms demonstrating the viability of leveraging mature CMOS process technology together with bonded III-V material [27]. Sun *et al.* recently demonstrated a large-scale integrated optical phase array highlighting the immediate scalability of pure silicon photonic devices using existing CMOS infrastructure [28]. All of these approaches are viable and have significant overlap, and over time more advanced integrated photonic solutions will likely come from a combination of all three.

Table 1.5. Several available photonic integration platforms and available components.

Platform	Demonstrated Component Count	Available Components
Indium Phosphide [26]	> 273 [25]	Polarization splitter, converter; SOA, MZI switch, laser, arrayed waveguide grating (AWG), phase modulator
Silicon [28]	> 12,288 [28]	Polarization splitter, converter; MZI switch, arrayed waveguide grating (AWG), phase modulator
Hybrid InP/Silicon [27]	> 410 [29]	Polarization splitter, converter; SOA, MZI switch, laser, arrayed waveguide grating (AWG), phase modulator

The work in this thesis is based on integration technology most closely following that outlined by Smit *et al.* [26]. Here a monolithic InP substrate is used to form complex photonic integrated circuits from a set of standardized building blocks. As the photonic integrated circuits (PICs) presented here represent novel applications of these components enabling new functionality, their operation must be closely investigated to account for unexpected interactions. For example, while discrete InGaAs photodiodes have extremely low dark currents on the order of 10 nA, integration on the same waveguide as other active devices such as SOAs and electro-optic phase shifters introduces electrical cross-talk from imperfect electrical isolation and results in a dark current three orders of magnitude higher. These and other effects must be studied and understood to overcome inevitable roadblocks to a viable photonic integration platform.

1.5 Dissertation Preview

Several examples of coherent receivers have been demonstrated to date, but few to none have been capable of integrating a local oscillator and receiving 100 Gbps data on a single wavelength. This thesis presents results on a monolithic tunable coherent receiver implemented with a widely tunable local oscillator capable of operating over the entire C-band for flexible bandwidth allocation and tunable selective filtering. This PIC integrates all of the components necessary for 100 Gbps DP-QPSK data reception on a single die, including local oscillator, mixer, and detector functions. A DSP is used in conjunction with the coherent receiver to recover data rates up to 100 Gbps, which also enables digital compensation of fiber nonlinearities. System testing with 50 Gbps QPSK data reception per polarization showed that operation down to an error floor of 10^{-8} was possible, limited by local oscillator noise.

In addition to receiver work, the design, fabrication and testing of an integrated 16x16 all-optical switch is covered. The switch design consists of an array of wavelength converters in series with an AWG router to perform wavelength-based switching and routing in a larger next generation version of what has previously been reported in [25]. Each of 16 wavelength converters perform 5 optical functions for a total of 81 optical functions including the on-chip AWGR filter. The chip consists of 545 optical components making it one of the largest examples of monolithic photonic integration on the InP platform to date. The switch utilized an electro-optically tuned SG-DBR laser with a 40 nm operating window with switching speeds in the nanosecond range for use in packet switching applications, and the laser bandwidth extended across the optical C-band (1525-1565 nm) for suitability in WDM applications. In addition, the wavelength conversion process resulted in signal regeneration beneficial for cascading switch networks.

The dissertation begins in Chapter 2 by reviewing the theory behind the operation of the coherent receiver and all-optical switch and the briefly describing the systems in which they will be used.

Chapter 3 and 4 define the requirements for each and discuss building block components required including improvements to the photodiode circuit to enable greater than 30 GHz operation, design work towards an integrated on-chip polarization demultiplexer, and design considerations for the lasers, wavelength converters, and AWGR. Chapter 5 presents the integration platform used for monolithic integration and gives an overview of device fabrication as well as various process improvements. In Chapters 6 and 8, the results of component characterization on the two PICs are given and discussed. System testing is presented and discussed in Chapters 7 and 9, and Chapter 10 concludes the dissertation with a summary and discussion of future research directions.

Chapter 2

Theory of Coherent Receivers and All-Optical Switches

2.1 Optical Transmission Link

Before jumping into the design and fabrication of the coherent receiver and all-optical switch, it is useful to review theory of two reference systems representing their main operating aspects. For the receiver, a typical optical communication link is presented in Figure 2.1 consisting of a transmitter, fiber optic cable, and receiver. In an intensity modulated/direct detection (IM/DD) scheme, an optical light source is directly modulated to generate a signal by shifting the amplitude of the carrier wave, known as amplitude-shift keying (ASK). The signal is then coupled to a fiber optic cable and transmitted to an end-point receiver. The cables have very low propagation loss on the order of 0.2 dB/km allowing the signal to propagate extremely long distances before needing to be regenerated. At the end of the link, a receiver directly converts the incoming signal from optical power into current, generating a voltage across a load resistor which is then fed to a decision circuit to recover the data.

In ultra-long range transmission systems with link lengths greater than 80 km, erbium-doped fiber amplifiers (EDFAs) are added to re-amplify the signal and increase reach. These amplifiers are broadband in nature and capable of amplifying all optical signals simultaneously within the optical C- and L-band from 1530-1565 nm and 1565-1625 nm, respectively. Traditionally, each carrier wave in a WDM system represented its own static channel with an independent transmitter and receiver; in more recent superchannel applications, however, the optical spectrum can be dynamically re-allocated based on demand. All channels are then multiplexed onto a single fiber, maximizing available spectrum carried in a single fiber. The narrowband filtering functionality and tunability of coherent receivers is particularly useful for reducing system complexity in superchannel applications by reducing filtering components down to a local oscillator.

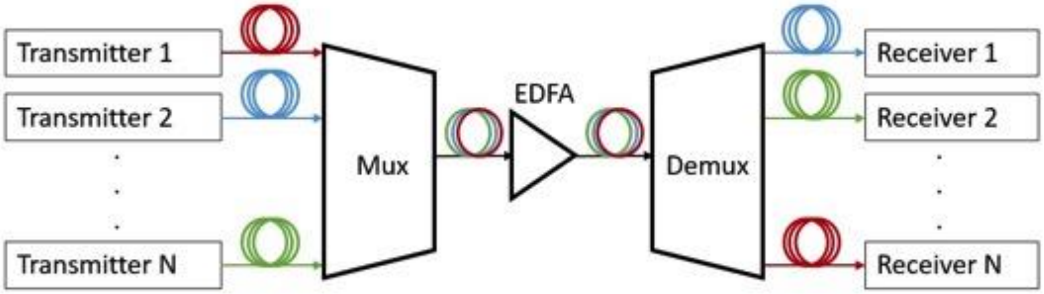

Figure 2.1. Block diagram of a simple WDM transmission link. The system may be further reduced by replacing the output demultiplexer with a tunable coherent receiver array.

2.2 Coherent Digital Modulation

As direct modulation bandwidth begins to push the limits of existing drive electronics, additional degrees of modulation freedom are useful to extend network bandwidth as well as improve spectral bandwidth and enhance tolerance to dispersion and other transmission distortion through the DSP electronics used. Several modulation formats utilizing both the amplitude and phase of a carrier wave are presented in Figure 2.2, including amplitude-shift keying, phase-shift keying, frequency-shift keying, and quadrature amplitude modulation. In Figures 2.2 (b), (c), and (d), only one dimension of the carrier wave is modulated, while in (e) both the amplitude and phase are modulated for maximum efficiency improvement.

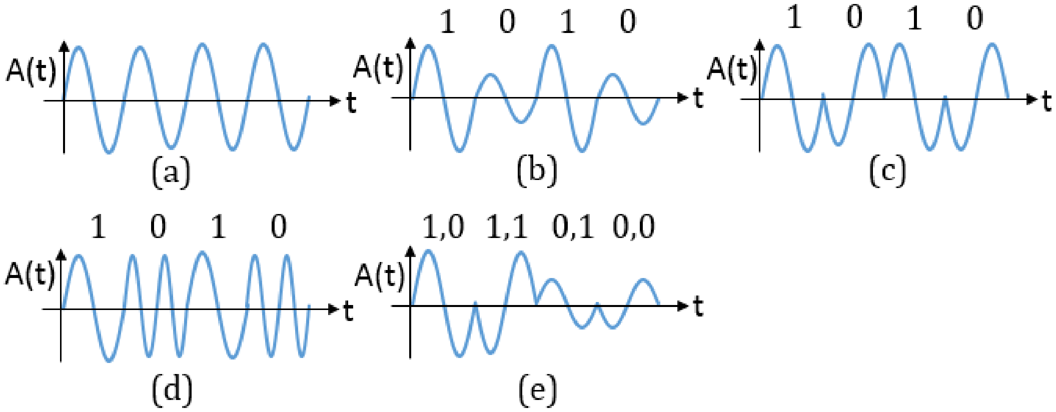

Figure 2.2. A sinusoidal carrier wave with various modulation formats: (a) no encoding (b) amplitude-shift keying (c) phase-shift keying (d) frequency-shift keying and (e) quadrature amplitude modulation.

In the amplitude-shift keyed format, only the magnitude of the wave is modulated and there is no change to the phase or frequency of the wave. The phase-shifted signal features a constant amplitude but periodically shifted phase to encode bits of data. For the phase-shifted signal in Figure 2.2 (c), a full π phase shift is used to denote the difference between a one and zero, but other phase shifts may be employed. Figure 2.2 (d) shows an example of a frequency-shift encoded signal where a higher and lower frequencies represent zeros and ones, respectively. Finally, Figure 2.2 (e) presents a quadrature amplitude modulated (QAM) signal where the modulation schemes of Figure 2.2 (b) and (c) are combined to enable two degrees of encoding freedom.

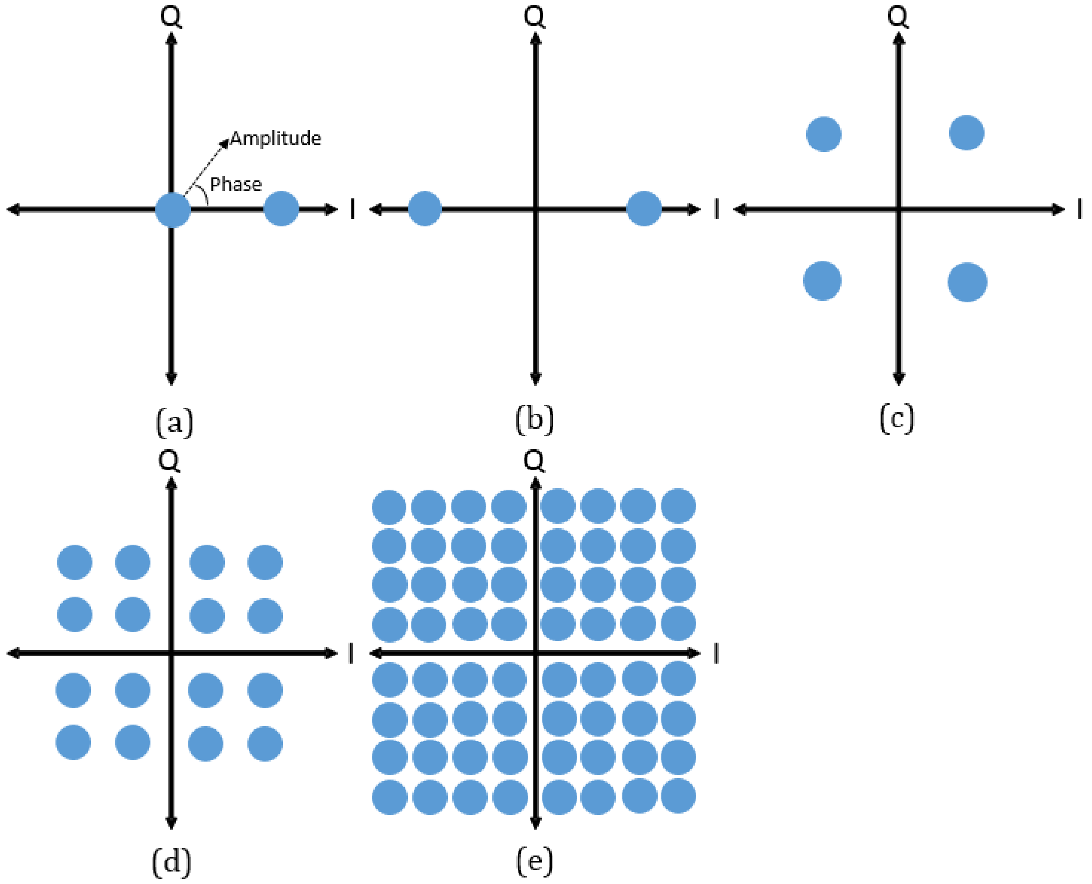

Figure 2.3. Constellation diagrams of several digital modulation formats, including (a) amplitude-shift keying, (b) binary phase-shift keying using a π phase shift, (c) quadrature phase-shift keying, (d) 16QAM, and (e) 64QAM.

Figure 2.3 presents constellation diagrams of several modulation formats utilizing both the amplitude and phase of a carrier wave for the QAM format. Here the magnitude of the points represents the amplitude and their angle represents the phase. Figure 2.3 (a) shows an ASK signal where only the magnitude varies and there is no change to the phase. In Figure 2.3 (b), a π phase shift is used to create a binary phase-shift keyed (BPSK) signal. Because there is greater separation between the BPSK points than the ASK format, this modulation format is more resilient to signal degradation.

Figure 2.3 (c) presents a quadrature phase-shift keyed (QPSK) encoding scheme. Similar to the BPSK signal, the carrier wave is phase shifted by π, but with an additional signal represented by two points at a π/2 phase offset from the first two points, placing it on the quadrature plane. Since two signals have now been encoded onto the same carrier wave, the spectral efficiency has doubled, and there are now two bits encoded for each symbol generated. By employing even more points, the spectral efficiency can continue to be scaled in this manner, limited only by the overlap of adjacent points due to noise. In Figures 2.3 (d) and (e), Gray coding is employed to equally space out adjacent points and improve resilience to noise. These constellations represent 16QAM and 64QAM, respectively.

In addition to the phase and amplitude of a carrier wave, an additional degree of modulation freedom exists in the wave's polarization. Due to the circular nature of a fiber optic cable, two orthogonal polarization modes exist which may be independently modulated allowing for twice the data on a single wavelength and again doubling the spectral efficiency. One drawback of dual polarization formats is increased system complexity, as each polarization requires its own set of modulators and receivers, but monolithic photonic integration makes such systems more feasible to realize.

2.3 Coherent Optical Communication Link

Coming back to the transmission system described in Section 2.1, a typical implementation of a coherent communication link is presented in Figure 2.4. Here the system is capable of supporting dual-polarization quadrature phase-shift keyed (DP-QPSK) formats. In the transmitter, the CW laser source is split into an X and Y arm representing the two independent polarizations. Each arm splits the signal in two again into I and Q components, and data is phase modulated onto each component of the carrier wave. A π/2 phase shift is induced on the Q signal, and I and Q components are recombined. The polarization of the X component is rotated 90° to be orthogonal to the Y component, and the X and Y polarizations are then combined, creating the full DP-QPSK signal.

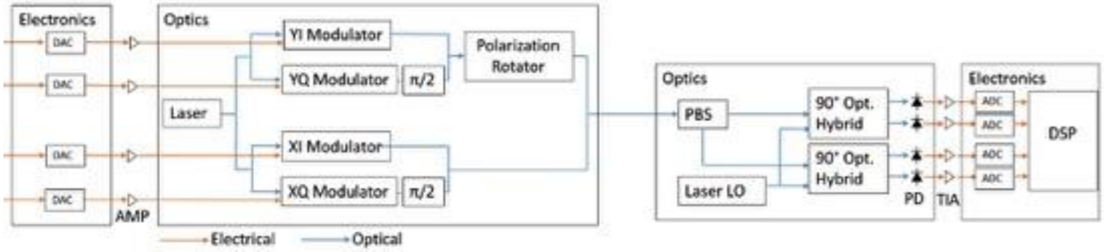

Figure 2.1. Block diagram of a DP-QPSK transmission link including transmitter, receiver, and required electronics.

In the receiver, the two polarizations are first split apart using a polarization beam splitter, which directs the light of the two polarizations on two different paths based on their interaction with the crystal plane. The signal is then mixed with a local oscillator tuned close to the wavelength of the incoming carrier, to produce an intermediate beat frequency between the two lasers that carries the phase data at a frequency low enough to be measured by electronics.

In the receiver, the electric fields of the signal and local oscillator may be described as

$$E_{signal} = \sqrt{P_{signal}(t)}e^{j(\omega_{signal}t+\phi_{signal})}$$

$$E_{LO} = \sqrt{P_{LO}(t)}e^{j(\omega_{LO}t+\phi_{LO})}$$

where P_{signal} and P_{LO} are the average optical power, ω_{signal} and ω_{LO} are the frequency where $\omega = 2\pi f$, and ϕ_{signal} and ϕ_{LO} are the absolute phase of the signal and local oscillator waves, respectively. The two fields are mixed in a 90° optical hybrid, which produces the output fields

$$E_1 = \frac{1}{2}\left(E_{signal} - E_{LO}\right)$$

$$E_2 = \frac{1}{2}\left(E_{signal} + E_{LO}\right)$$

$$E_3 = \frac{1}{2}\left(E_{signal} - jE_{LO}\right)$$

$$E_3 = \frac{1}{2}\left(E_{signal} + jE_{LO}\right)$$

The fields are then converted to electrical current in a photodetector given by

$$i_{photo} = \mathcal{R}P_{incident}$$

where the conversion is determined by the responsivity $\mathcal{R}$ of the photodiode which can be expressed as

$$\mathcal{R} = \frac{\eta q}{h\nu} = \eta \frac{\lambda(\mu m)}{1.24}$$

where η is the internal quantum efficiency of the photodiode, q is the electron charge, h is Planck's constant, and ν is the frequency of the incident wave [30]. The second expression in this equation uses the relationship

$$\lambda = \frac{c}{\nu}$$

to express the responsivity in a form conveniently relating conversion efficiency to the wavelength of the incident light.

By connecting the ends of the photodiodes detecting the I and Q components in series, the sum of their photocurrents will cancel out common mode noise generated by the local oscillator as well as double the signal amplitude. For a balanced photodiode configuration, the received photocurrents are

$$i_I = i_1 - i_2 = \mathcal{R}\sqrt{P_{signal} P_{LO} \cos\big((\omega_{signal} - \omega_{LO}\big)\, t + (\phi_{signal} - \phi_{LO}))}$$

$$i_Q = i_3 - i_4 = \mathcal{R}\sqrt{P_{signal} P_{LO} \sin\big((\omega_{signal} - \omega_{LO}\big)\, t + (\phi_{signal} - \phi_{LO}))}$$

[3].

After conversion of the in-phase and quadrature components from an optical to electrical signal, the photocurrent may be amplified and converted to voltage through a trans-impedance amplifier, then sampled to convert from an analog to digital format for compatibility with DSP software/hardware. In the work of this thesis, the analog-to-digital conversion (ADC) was performed using a Keysight Infiniium 90000-X digital storage oscilloscope (DSO). The oscilloscope is capable of digital sampling at rates up to 40 GSA/s and has a 33 GHz analog bandwidth and 2.1 mV noise floor [31], which was more than sufficient to meet the 25 Gbaud design goal for the coherent receiver.

2.4 Digital Signal Processing and Kalman Filter Carrier Phase Recovery

Digital signal processing was implemented using Keysight 89601B vector signal analysis (VSA) software. Together with the DSO and heterodyne receiver, this system functions as an optical modulation analyzer (OMA) capable of analyzing optical links carrying advanced high speed digital modulation formats as well as characterizing and compensating deleterious effects such as chromatic dispersion and polarization mode dispersion (PMD).

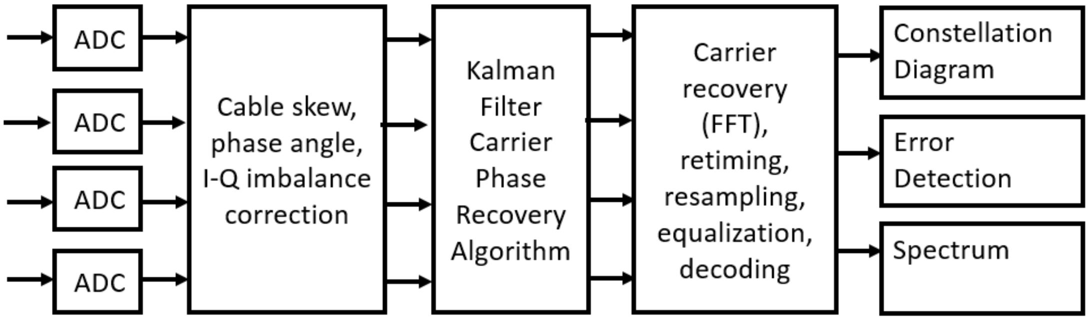

Figure 2.5. Block diagram of the VSA software-based DSP implemented in the OMA [32].

A block diagram detailing the implementation of the digital signal processor in the OMA is presented in Figure 2.5 [32]. After sampling in the ADC, the signal is pre-distorted to account for imperfections in the receiver optics and ADC electronics. Next the signal may be modified by user-defined algorithms to further compensate for link imperfections such as carrier phase noise and dispersion. In the receiver implementation presented in this dissertation, a Kalman filter-based carrier phase recovery algorithm provided in the DSP software [33] was used to compensate for the phase noise of the receiver's local oscillator. Such software-based approaches to phase tracking have recently become attractive as faster electronics (DSPs in particular) have enabled higher sampling rates for real-time compensation of higher bitrates.

A Kalman filter was required for phase recovery in the optical receiver due to a relatively large amount of phase noise in the local oscillator. In the process of down-converting the carrier wave to a recoverable frequency, the phase of the signal becomes obscured by phase noise generated due to the flicker noise of both the carrier and local oscillator. Using a phase-lock control loop, the phase difference between the carrier wave and LO can be tracked through either a hardware optical phase-lock loop that uses an error signal from the receiver photodiode to lock the local oscillator to the carrier or a software-based feed-forward loop that filters out the flicker noise.

The DSP implementation of a feed-forward control loop uses the received signal to produce a phase noise estimate $\widehat{\Phi}_{noise}$. This estimate is subtracted from the baseband signal to produce the desired phase. The phase noise estimate is generated using

$$\widehat{\Phi}_{noise}(k) = \Phi_n(k) + \frac{2\pi}{M}\left(-\frac{M}{2} + \hat{\imath}\right)$$

where $\Phi_n(k)$ is the phase component extracted from the signal at sample k, M represents the number of constellation points, and $\hat{\imath}$ is chosen such that

$$\underset{0 \le i \le M-1}{min} \left|\widehat{\Phi}_{noise}(k-1) - \left[\Phi_n(k) + \frac{2\pi}{M}\left(-\frac{M}{2} + \hat{\imath}\right)\right]\right|$$

which assumes the smallest change in $\widehat{\Phi}_{noise}$ to overcome the M-fold uncertainty of the measurement [2]. The phase noise component is extracted from the signal by raising it to the M-th power to remove the phase information and then low pass filtering to remove high frequency noise. With the phase noise removed, the underlying phase information may be recovered. Since the resulting measurement contains both the amplitude and phase of the carrier wave, additional deleterious effects may be compensated in the DSP, providing additional benefit over an envelope detector that can only measure amplitude.

The alternative to the Kalman filter approach is a hardware implementation of an optical phase-lock loop. Here the phase difference between the two lasers is kept constant by using an electronic control loop to actively adjust the frequency of the local oscillator to match the carrier wave, overcoming any individual drift between the two lasers. Historically this approach was not commonly utilized due to the large loop bandwidth and short loop delay required for the control electronics, but it has recently been demonstrated in [34] using an integrated electronic IC and loop filter with a tunable local oscillator.

After phase tracking has been employed, the signal may be broken up into a variety of formats such as its frequency components using a fast Fourier transform (FFT) or its modulation format using a demodulator [35]. The VSA software performs carrier recovery using an FFT to measure and track the absolute phase of the incoming signal which it then uses for clock recovery, resampling, equalization, and decoding of the original signal. From here the signal may be analyzed in the form of a constellation diagram or error detection when using a pseudo-random bit sequence (PRBS); this information may then be used to optimize the link compensation algorithms and improve the quality of the signal.

2.5 Receiver Sensitivity, Loss Budget, and Noise Figure

An important aspect of a receiver is its sensitivity, the minimum amount of power required to recover an input signal. In the case of a simple photodetector, the ideal sensitivity is defined by

$$Sensitivity = 10\log(i_{thermal}\mathcal{R}_{\text{RX Max}}) + SNR$$

where $i_{thermal}$ represents the thermal noise of the photodetector circuit typically consisting of the photodiode in series with a 50 Ω load and SNR is the desired signal-to-noise ratio of the recovered signal. For this ideal circuit, the thermal noise may be defined as

$$i_{thermal} = \sqrt{\frac{4k_B TB}{R}}$$

where k_B is the Boltzmann constant, T is the ambient temperature of the circuit, B is the bandwidth of the detector, and R is the load resistance. If the photodetector dark noise is large enough, the detector becomes limited by shot noise, and the $i_{thermal}$ term is replaced with i_{shot} where

$$i_{shot} = \sqrt{2qI_{dark}B}$$

given that q is the charge of an electron and I_{dark} is the dark current.

For a heterodyne receiver, the sensitivity becomes more complex due to additional splitting loss in the 90° optical hybrid as well as non-idealities such as coupling waveguide loss and shot noise from the local oscillator. These non-idealities may be summed into a resulting noise figure (NF) representing the additional power required over the theoretical thermal noise floor to recover the incoming optical signal. Now the sensitivity may be defined as

$$Sensitivity\ (dBm) = 10\log\left(\frac{i_{thermal}(mA)}{\mathcal{R}_{\mathrm{RX\ Max}}(\frac{mA}{mW})}\right) + NF\ (dB) + SNR\ (dB)$$

where $\mathcal{R}_{\mathrm{RX\ Max}}$ accounts for additional losses from coupling, hybrid splitting, and waveguide loss in the expression

$$\mathcal{R}_{RX\ Max}(\frac{mA}{mW}) = \mathcal{R}_{PD}(\lambda_{Max})(\frac{mA}{mW}) \times \alpha_{WG} \times \alpha_{Coupling} \times \alpha_{Hybrid}$$

where $\mathcal{R}_{PD}(\lambda)$ is the responsivity of the photodiode at wavelength λ and α_{WG}, $\alpha_{coupling}$, and α_{hybrid} are dimensionless loss factors expressing excess loss in the receiver's waveguides, fiber coupling, and hybrid, respectively. Thus the sensitivity of the receiver is strongly dependent on the wavelength-dependent net responsivity, described as

$$\mathcal{R}_{RX}(\frac{mA}{mW}) = \mathcal{R}_{PD}(\lambda)(\frac{mA}{mW}) \times \alpha_{WG} \times \alpha_{Coupling} \times \alpha_{Hybrid}$$

The sensitivity required for a given SNR may be found by measuring the noise equivalent power (NEP) of the receiver defined as the input power at which the signal and noise are equal. The sensitivity may then be defined as

$$Sensitivity\ (dBm) = NEP(\lambda)\ (dBm) + SNR(dB)$$

With the sensitivity calculated, the resulting noise figure may also be found by the relationship

$$NF(\lambda)(dB) = Sensitivity(dBm) - 10\log\left(\frac{i_{thermal}(mA)}{\mathcal{R}_{\text{RX Max}}\left(\frac{mA}{mW}\right)}\right) - SNR(dB)$$

which defines the additional noise due to receiver non-idealities.

2.6 High Speed RF Photodetector Circuits Using Inductance Peaking

For high-speed communication systems, the photodiode must be designed to effectively convert as much incoming optical power to electrical current as possible while simultaneously having a large bandwidth to support high speed signals. One way to maximize the RF response of a given semiconductor photodiode is by using inductance peaking as demonstrated in [36] to improve response time by optimizing the detector circuit with an additional inductive load to create a peak in the response of the resulting RLC circuit that pushes out the bandwidth.

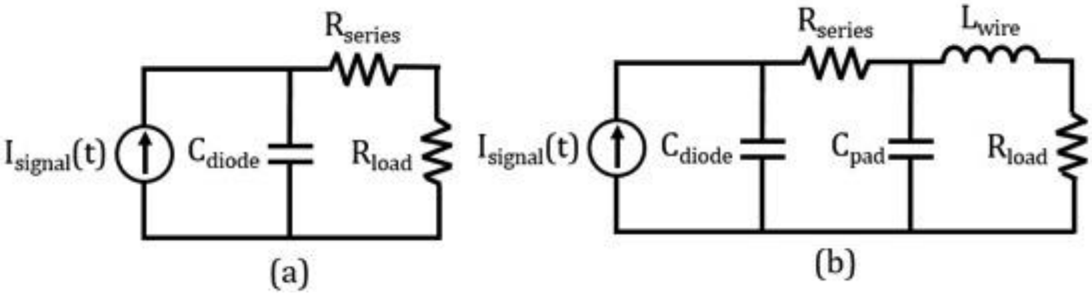

Figure 2.6. Equivalent circuits of the photodiode. These include (a) the circuit of an ideal photodiode connected to a resistive load and (b) non-idealistic photodiode circuit including the parasitic pad capacitance and wire bond inductance from connecting to the load [36].

The bandwidth of the detector is determined by the RC constant of the diode circuit, the transit time through the depletion region, and any carrier trapping at the heterojunction interfaces that can cause additional capacitance in the circuit. The equivalent circuit of an ideal photodiode in parallel with a resistive load is shown in Figure 2.6 (a). Here the photodiode is represented as an ideal current source with current $i_{signal}(t)$ in parallel with diode capacitance of the depletion region C_{diode} as well as any capacitance generated from carrier trapping. A series resistor R_{series} represents resistance in the semiconductor material. To analyze the photodiode itself, this circuit assumes ideal wires with no inductance or capacitance added to the circuit. In this case, the cutoff frequency of the circuit is

$$f_{3dB\ RC} = \frac{1}{2\pi C_{diode}(R_{series} + R_{load})}$$

For a 30x3.65 µm area waveguide InGaAsP photodetector with a 1.2 µm thick depletion region, the approximate diode capacitance is 10 femtoFarad (fF).

Assuming an additional 30 Ω series resistance and 50 Ω load, the resulting cutoff frequency of the circuit is 199 GHz. However, one must also take into account the transit time response of the photodiode resulting in the relationship

$$f_{3dB\ total} = \frac{f_{RC} f_{transit}}{f_{RC} + f_{transit}}$$

From [37] the transit-time-limited bandwidth for a photodetector with a thin absorber such that $\alpha L << 1$ is

$$f_{3dB\ \eta} = 0.45 \alpha \nu (1 - R)$$

where α is the absorption coefficient, ν is the carrier velocity, and R is the Fresnel reflectivity of the detector. Thus for an anti-reflective coated InGaAsP quantum well absorber using an approximated carrier velocity of $\nu = 1.7 \times 10^5$ m/s [38] and absorption coefficient $\alpha \approx 10000\ cm^{-1}$ [39], the theoretical transit time bandwidth is 76.5 GHz and the theoretical cutoff frequency of the photodiode circuit is 55.26 GHz.

In reality, the photodiode is connected to an electrical pad with a finite capacitance as well as a wire bond with an inductance of 0.7 nH/mm; these elements are included in Figure 2.6 (b). In this case, the transfer function of the circuit is

$$\frac{i_{out}(\omega)}{i_{in}(\omega)} = \frac{1 + j\omega R_{series} C_{diode}}{1 + \frac{C_{diode}}{C_{pad}} + j\omega R_{series} C_{diode}} + j\omega R_{load} C_{pad} - \omega^2 L_{wire} C_{pad}$$

and the resulting frequency response is plotted in Figure 2.7 using the same photodiode parameters of the previous example with the addition of a 10 fF pad capacitance and 150 pH wire inductance. With the additional elements, the circuit's response is limited to 150 GHz for a theoretical cutoff frequency of 50.66 GHz including the photodiode transit time. A resonance occurs due to interaction between the inductor and capacitor with a peak at roughly 80 GHz.

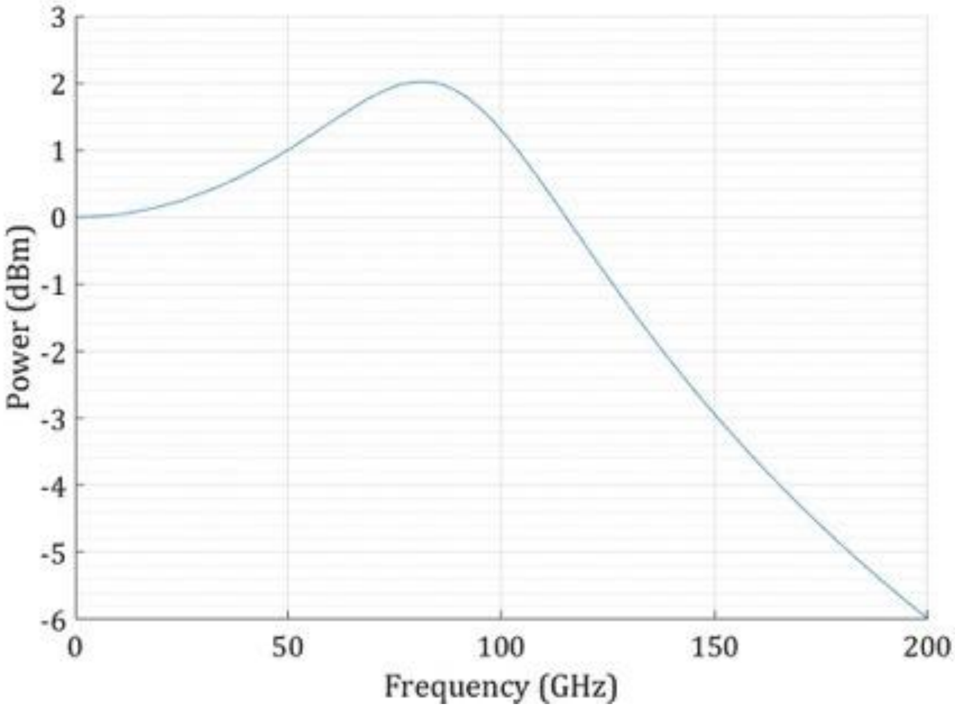

Figure 2.7. Frequency response of the photodiode circuit including the pad capacitance and wire bond plotted using MATLAB. Simulation code may be found in Appendix B.

To compensate for the parasitic elements of the circuit, inductance peaking may be employed to optimize the wire inductance to match the capacitor elements. Figure 2.8 shows the response of the same circuit with wire inductances varying from 500 pH down to 50 pH.

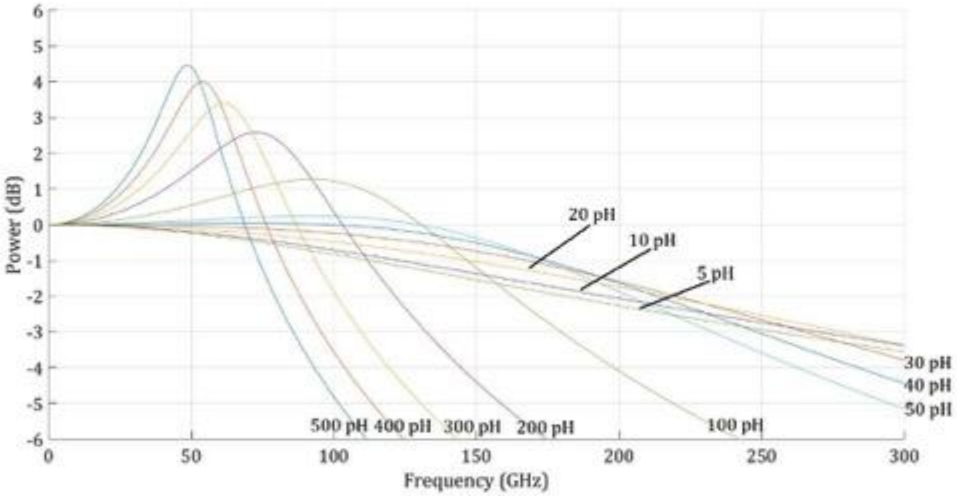

Figure 2.8. Photodiode equivalent circuit response with varying wire bond inductance. Inductance values vary from 500 pH to 50 pH. Simulation code may be found in Appendix B.

From the model, an optimal cutoff frequency occurs for an inductance of 20 pH. The cutoff frequency increases greatly with decreasing inductance from 500 pH to 50 pH and then begins to increase again for inductances below 20 nH. At 20 nH, the cutoff frequency of the circuit is 278 GHz resulting in a 60 GHz 3 dB response including transit time. As the ideal circuit in Figure 2.6 (a) had a response of only 55.26 GHz, this results in a 5 GHz improvement from simply optimizing the circuit design. From [36], the same equivalent circuit without a parasitic capacitance should have an optimal inductance of

$$L_{wire} = \frac{C_{diode}(R_{series} + R_{load})^2}{2}$$

resulting in an optimal inductance of 32 pH, closely matching the model. To achieve this inductance using a 1 mil diameter gold wire, the wire bond would need to measure just 29 μm long between the photodiode pad and transmission line. While difficult, this length could be achieved using a custom carrier designed for the transmission lines to sit at the same height as the photodetector pads.

2.7 All-Optical Switching Node

Building upon the static link presented in Section 2.1, an updated communication link featuring a switch node is presented in Figure 2.9. Here an all-optical switch is utilized to re-route incoming data to the desired destination. An optical wavelength (frequency) demultiplexer is used to split out the incoming wavelengths that are then fed into individual channels of the switch. Each input may be individually configured to route the signal to the desired output. As multiple signals may be sent to the same port, the multiplexing function at the output is inherently performed.

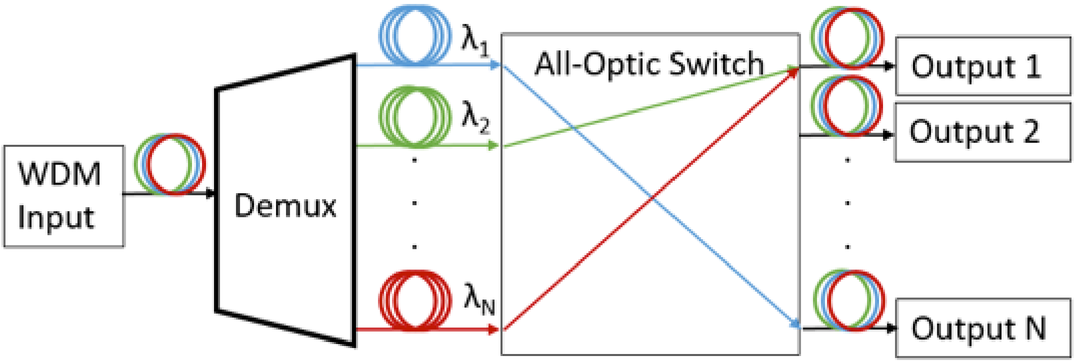

Figure 2.9. Block diagram of an all-optical switching node for a WDM communication link.

Several attractive functions may be implemented by an all-optical switch depending on the architecture used. Add-drop multiplexing, for example, allows the switch to add new data to an existing data stream while dropping off others. An add-drop multiplexing scheme using an all-optical switch is presented in Figure 2.10. In this configuration, the switch has several input ports dedicated to adding and several output ports dedicated to dropping. This functionality is particularly useful for transmitting/receiving data in fiber optic ring networks where there are several endpoints along a circular path.

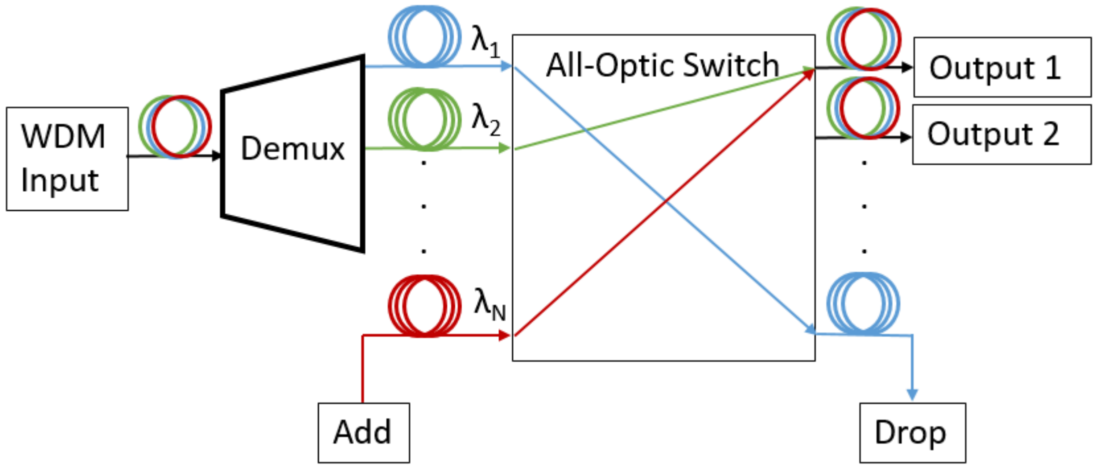

Figure 2.10. Block diagram of an all-optical switch used in an optical add-drop multiplexer configuration.

For larger networks with more connection points, it is useful for the switch to be able to perform signal regeneration, particularly in cases where multiple switches are cascaded together causing additive insertion loss and signal degradation. Three regenerative properties of all-optical switches are clock recovery/re-timing, re-amplifying, and re-shaping [17]; these are illustrated in Figure 2.11. The re-timing function is typically performed by feeding the incoming signal into a mode-lock laser with a similar pulse length to the original signal. This provides feedback that causes the laser's pulse to synchronize with the timing of the incoming signal. The resulting pulse train is used in conjunction with the original signal to gate an amplifier, recreating the original signal [17].

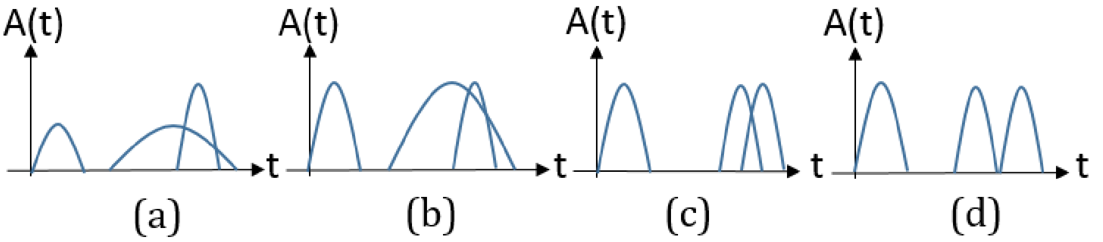

Figure 2.11. Plots of several optical pulses representing various stages of 3R regeneration including (a) a degraded signal, (b) re-amplification, (c) re-shaping, and (d) re-timing.

Implementation of the re-amplifying function is much simpler, requiring only an amplifier to re-amplify the incoming signal at the cost of additional amplified spontaneous noise (ASE) from the amplifier. The re-shaping function goes one step beyond re-amplification by generating a new signal that removes the additive ASE noise inherent in re-amplification; this functionality is typically implemented through optical nonlinearities used to convert the incoming signal to a new wavelength. Because several of the nonlinear processes allow wavelength switching, the conversion process may also be used as a switching function [17].

2.8 SOA Wavelength Conversion

There are several nonlinear processes which may be used to perform all-optical switching, including cross-gain modulation, cross-phase modulation, and four-wave mixing [17]. As these nonlinearities occur at large optical intensities, an amplifier such as an SOA or EDFA is typically required. SOA-based wavelength converters are typically preferred for optical switching due several advantages over EDFAs in the area of integration, including size, power consumption, and scalability.

In cross-gain modulation (XGM), an incoming signal is used to deplete carriers in an optical amplifier, as shown in Figure 2.12 (a). When a continuous wave (CW) signal is passed through at the same time, the carrier depletion changes the gain available to it, which modulates its amplitude, regenerating the original signal. The bandwidth of the resulting switch is limited by the gain recovery time of the amplifier. For SOAs on indium phosphide, this is typically on the order of 100 ps, theoretically limiting the switch to 10 GHz operation, but more complex gain dynamics have been utilized to enable switching beyond 100 Gbps [17].

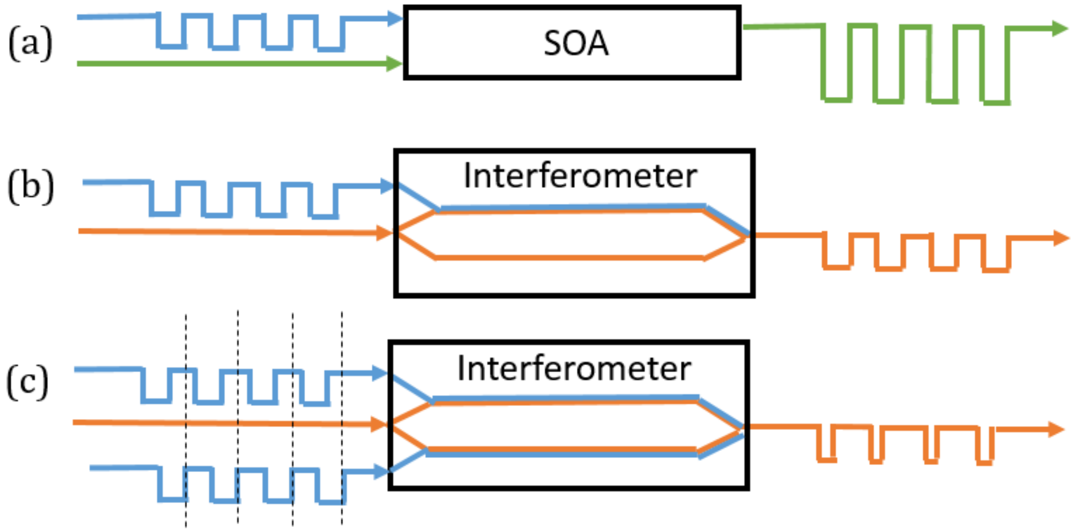

Figure 2.12. Several wavelength conversion schemes based on nonlinear optical processes, including (a) cross-gain modulation, (b) cross-phase modulation, and (c) differential cross-phase modulation.

In cross-phase modulation (XPM), a large optical intensity is used to induce an index shift in a waveguide caused by the optical Kerr effect. This phase shift may be used to modulate a CW wave passed through the waveguide [17]. By introducing the large optical intensity to only one arm of a Mach-Zehnder interferometer as shown in Figure 2.12 (b), the incoming optical signal gates the CW signal on that arm, resulting in optical-optical modulation. In this case, the bandwidth is limited by the index response of the material to the large optical intensities. While these are typically much faster than the gain mechanism used in XGM, the large optical intensities required are usually achieved through use of SOAs in the interferometer that are once again limited by their gain recovery times. However, more complex interferometer configurations may be used to overcome the inherent limitations of the SOAs; for example, a differential interferometer such as that in Figure 2.12 (c) can split the incoming optical signal to drive both arms of an interferometer in a push-pull configuration allowing for much faster operation by setting the delay between the two inputs to achieve the desired switch bandwidth.

2.9 All-Optical Switch

Building upon the wavelength conversion approaches discussed in the previous section, an all-optical switch based on an XPM wavelength converter is presented in Figure 2.13. In this configuration, a tunable laser is used to choose the CW signal into the interferometer. By using a wavelength selective filter downstream of the converter, the signal may be routed to any desired output based on its wavelength, and output multiplexing may also be performed as all signals routed to individual outputs are combined in the filter. In this approach to all-optical switching, most of the system complexity is tied up in the wavelength converter that performs the routing function by selecting the new wavelength. As all of these components may be monolithically integrated, this makes it a suitable candidate technology for monolithic integration of an all-optical switch.

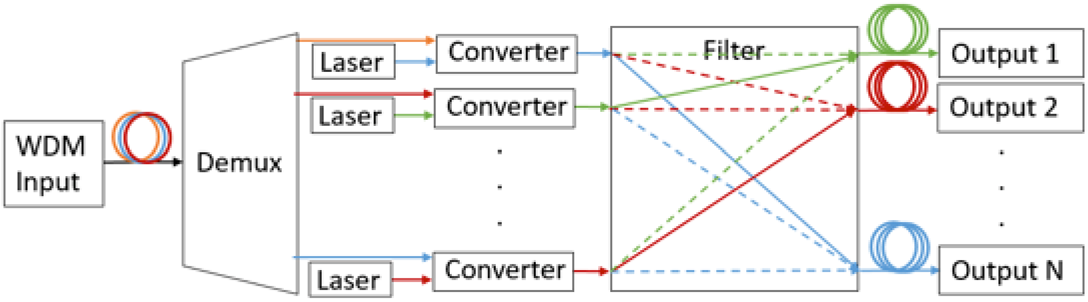

Figure 2.13. Diagram of a WDM all-optical switch based on an array of wavelength converters with a downstream wavelength selective filter.

2.10 Chapter Summary

In this chapter, the theory behind a simple communication link was built up to include both coherent communication schemes and switch network implementations. Several coherent modulation formats were discussed and the operation behind a coherent receiver was described. After this an all-optical switching node was described and different operating configurations were detailed. Finally, several forms of nonlinear optical processes were discussed for use in a wavelength converter all-optical switch, and the architecture for an all-optical switch based on such mechanisms was laid out. With the design of the receiver and router complete, Chapters 3 and 4 will continue by discussing the building block components required for implementation of a monolithic tunable coherent receiver and all-optical switch.

Chapter 3

Design of a Monolithically Integrated Coherent Receiver

3.1 Monolithically Integrated Coherent Receiver Requirements

There are several attributes necessary for the functionality of a monolithically integrated coherent receiver. These break down into three broad performance categories: optical gain, propagation loss, and response time. The tunable coherent receiver consists of 5 overall functional blocks that were briefly outlined in Chapter 2: an SG-DBR laser local oscillator (LO), amplifier SOAs, photodiodes, 90° optical hybrids, and interconnecting waveguides and splitters that are summarized in Figure 3.1. For the SG-DBR laser, optical gain is necessary to allow for stimulated emission of photons as well as efficient electrical pumping to facilitate current injection into the gain material, large optical confinement to make more effective use of available gain, and high index tuning efficiency for efficient mirror operation. In the on-chip amplifiers, optical gain is required as well as large optical confinement for more effective amplification of small signals. The photodiodes require an absorption region designed for both minimal carrier transit time and a small RC constant to avoid limiting RF performance of the circuit response. It is also beneficial to have a high absorption coefficient for reduced diode area.

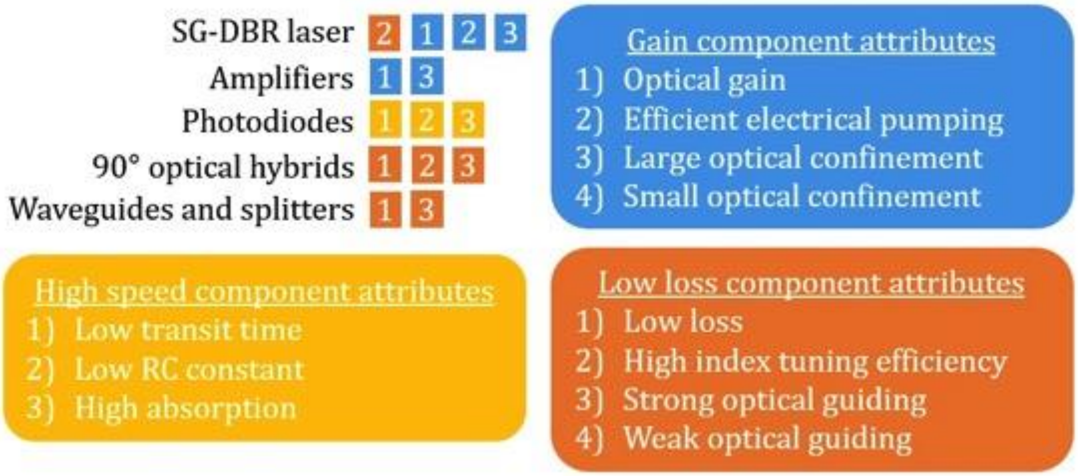

Figure 3.1. Chart summarizing monolithically integrated coherent receiver functional blocks and operating requirements separated by the categories of gain, high speed, and low loss.

In the 90° optical hybrids, sufficiently low loss is required to enable an incoming signal to be received without significant attenuation as well as high index tuning efficiency for adjusting the quadrature point of the hybrid splitter and strong optical confinement for compact PIC layout. For the splitters and waveguides, both low loss and strong optical guiding are beneficial for seamless connection of interacting components.

3.2 Monolithically Integrated Coherent Receiver Components

Recalling the overall requirements for coherent receiver from Section 1.2.1, the coherent receiver should have minimal LO linewidth, maximum wavelength stability, minimal loss (particularly through the 90° optical hybrid), high responsivity, minimal photodiode response time, and a wide wavelength range. The following sections detail design work on individual components towards meeting these specifications.

3.2.1 90° Optical Hybrid

Two typical types of 90° optical hybrids that have been demonstrated in monolithic receivers are those based on 2x4 multi-mode interferometers (MMI) [40] and 2x2 3-dB coupler arrays [41]. Schematic diagrams of the two approaches are presented in Figure 3.2. Each hybrid operates by splitting the input data and LO signals and mixing them together through a series of mixing stages. In the process, one half of the LO signal is phase shifted 90° to the quadrature point while the other is left in-phase; each of these is mixed with the incoming signal to recover the quadrature and in-phase components of the data.

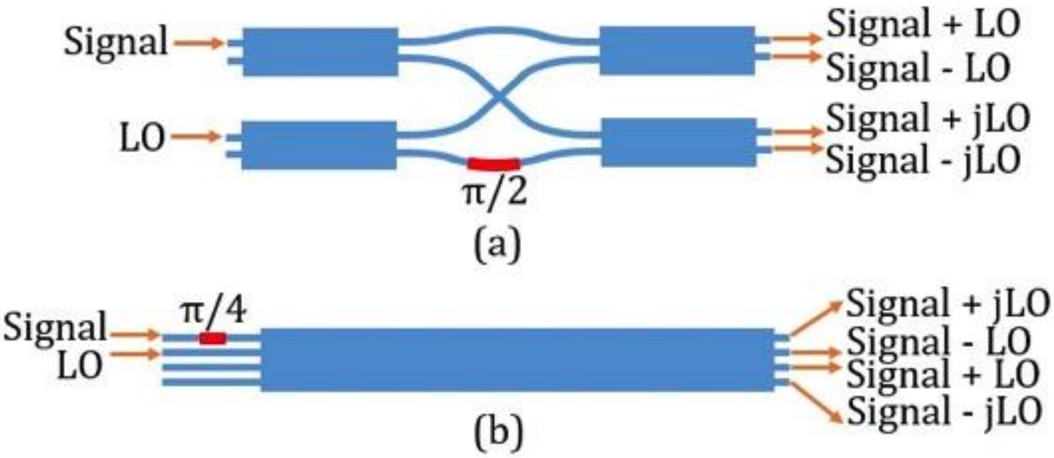

Figure 3.2. Diagrams of two implementations of an integrated 90° optical hybrid: (a) a 2x2 MMI-based design [41] and (b) a 4x4 MMI-based design [40].

Several design parameters for the hybrid are listed in Table 3.1. For minimal overhead in the DSP equalization step, the hybrid outputs should be balanced, as any residual imbalance can skew the received signal and cause an increase in detection errors. The phase of the quadrature outputs must be close to 90° to avoid ambiguity in the adjacent phase decision points that can also cause an increase in detection errors. To avoid signal jitter and feedback to the LO, the hybrid must also have minimal back reflections, and low excess loss facilitates maximum sensitivity.

Table 3.1. Requirements for several parameters of the monolithically integrated 90° optical hybrid.

Design Attribute	Goal
Output Imbalance	< 1 dB
Quadrature Phase	90 ± 1°
Back Reflection	< -40 dBm
Excess Loss	< 1 dB
Wavelength Range	> 100 nm

The hybrid design of Figure 3.2 (a) was ultimately chosen as phase shifters may be placed on the routing arms to enable active tuning of the quadrature point, greatly increasing resilience to fabrication errors. A diagram of the MMI with including critical dimensions is presented in Figure 3.3. The MMIs were designed for a broad range of operation from 1500-1600 nm to ensure good performance over the full C-band.

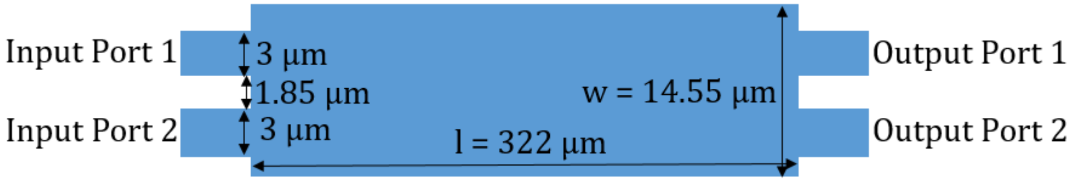

Figure 3.3. Schematic diagram of the MMI used in the 90° optical hybrid.

The MMI's design was simulated and verified using commercial FIMMWAVE mode solving software. Simulation covered the splitting of a TE_0 mode input into the upper arm of the MMI over the wavelength range from 1500 to 1600 nm.

Simulation results showing the mode evolution through the multi-mode section at 1525, 1550, and 1565 nm are presented in Figure 3.4. Excess loss and output imbalance measured at output ports 1 and 2 are plotted in Figure 3.5 from 1500 to 1600 nm. Back reflected power to input port 1 was not plotted and remained below -60 dBm across all wavelengths.

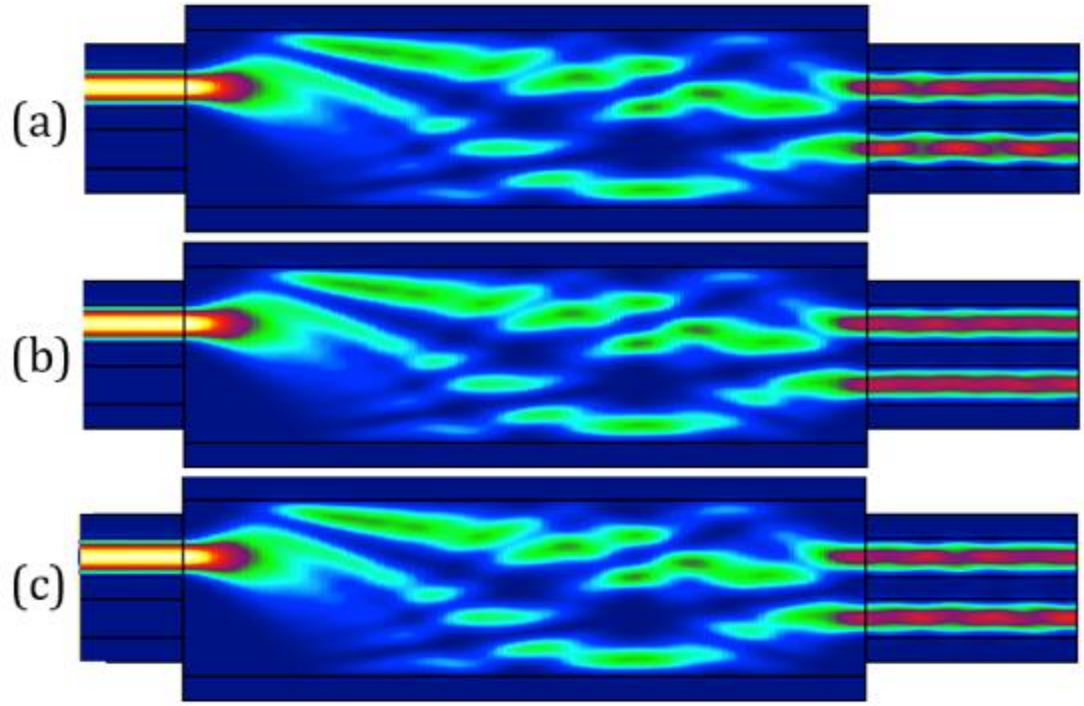

Figure 3.4. Simulated propagation of a TE_0 mode through the MMI from input port 1 into output ports 1 and 2 at (a) 1525 nm, (b) 1550 nm, and (c) 1565 nm.

Simulation performed with FIMMWAVE mode solver software using the film mode matching (FMM) method.

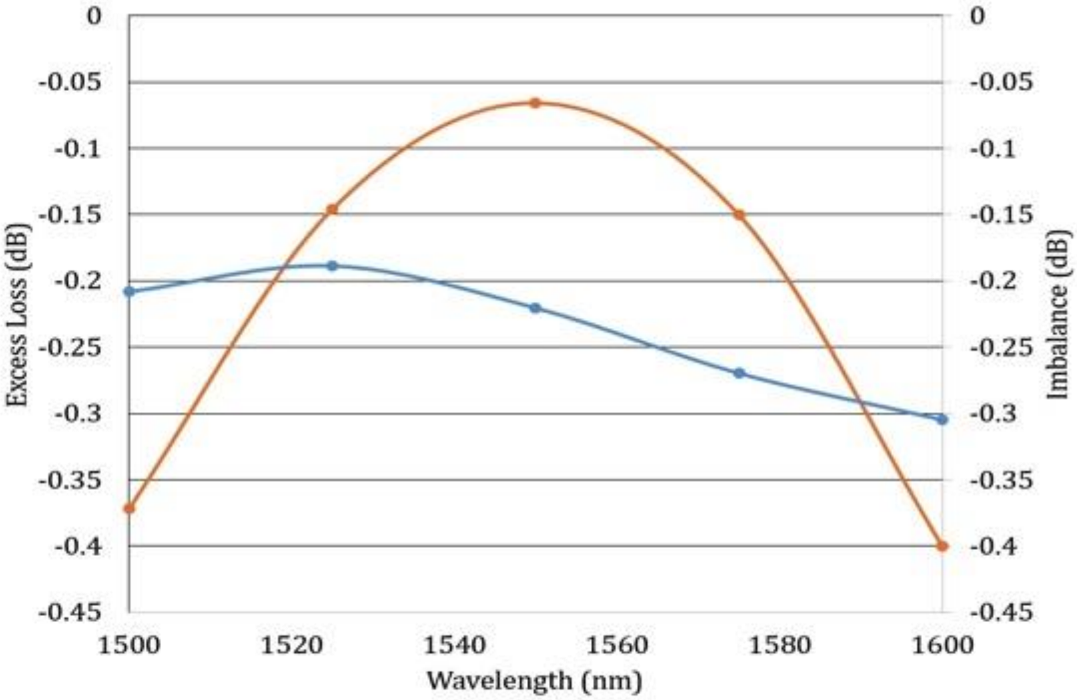

Figure 3.5. Simulated total excess loss of a TE_0 mode propagated from input port 1 to output ports 1 and 2 as well as imbalance between output ports 1 and 2 plotted versus wavelength. Simulation performed with FIMMWAVE mode solver software using the film mode matching (FMM) method.

For this hybrid design, a waveguide crossing is required to connect the in-phase LO signal to the upper second stage MMI. To minimize back reflections and crosstalk of the two waveguides, incidence angle was simulated in [42] using beam propagation method and found that incidence angles above 25° result in negligible reflections and crosstalk.

3.2.2 Local Oscillator

The local oscillator consists of an SG-DBR laser based on the design from [43]. A schematic diagram is presented in Figure 3.6. The laser consists of two grating mirrors with offset sampling periods resulting in two complementary comb filters that may be index shifted through current injection allowing for the comb peaks to be tuned across several nanometers. When properly designed, the two filters use the Vernier effect to select a wide range of outputs and greatly increase the available tuning range of the device.

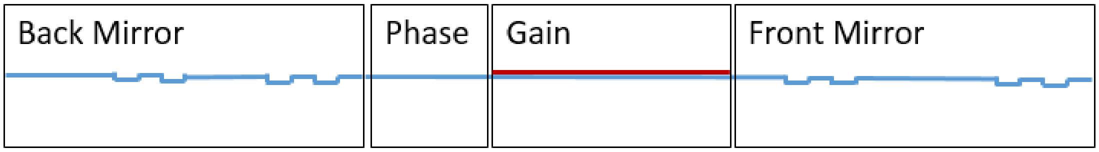

Figure 3.6. Schematic diagram of the SG-DBR laser consisting of back mirror, front mirror, phase section, and gain section [43].

To define the operating wavelength of the laser, several parameters must be set; these are illustrated in Figure 3.7; for the SG-DBR laser design of this dissertation, parameters were based off of previous work from [44]. First, the grating period is defined to center both comb filters at 1540 nm to match the gain peak of the material. For a grating period Λ, the resulting Bragg wavelength λ_B is

$$\lambda_B = 2n\Lambda$$

For a waveguide index of n = 3.26, the grating period required for a peak reflection at 1540 nm is 236 nm. Next the sampling period Z_0 of the gratings must be chosen to set the peak spacing of the combs. For continuous tuning, the peak spacing for each mirror must be less than the total tuning range of the mirror based on the index tuning efficiency of the material. For a 1.4 μm bandgap waveguide, the maximum measured tuning range is 7 nm [44]. Using a conservative 3.6 μm maximum spacing, the front mirror was designed to have a 3.55 nm peak spacing requiring Z_0 = 90.8 μm and the back mirror was designed for a 3.24 nm peak spacing requiring Z_0 = 99.6 μm. The sampling width Z_1 of the gratings and number of grating bursts N adjusts the reflection strength of the mirrors; the values Z_1 = 3.6 μm N = 6 for the front mirror and Z_1 = 6 μm N = 10 for the back mirror were chosen resulting in reflectivity spectrums plotted in Figure 3.8. Total theoretical tuning range of the two comb filters may be determined by

$$\lambda_{RMS} = \frac{\Delta\lambda_{\mathrm{front}} \times \Delta\lambda_{\mathrm{back}}}{\Delta\lambda_{\mathrm{front}} - \Delta\lambda_{\mathrm{back}}}$$

[45] where λ_{RMS} is the repeat mode spacing. Thus the theoretical lasing range is 37.1 nm.

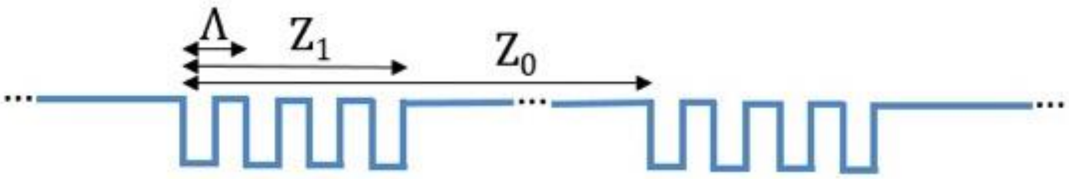

Figure 3.7. Illustration of the design parameters of the sampled mirror gratings in the tunable laser [43].

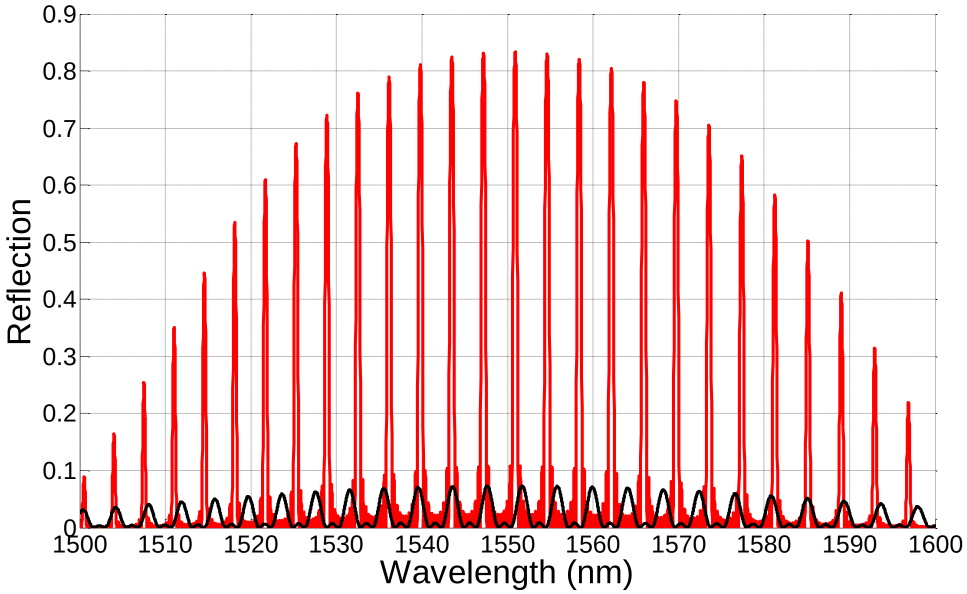

Figure 3.8. Simulated reflectivity of the front and back mirror of the SG-DBR laser versus wavelength. The red and black traces indicates the back and front mirror reflectivities. Respectively. Simulation code written by Michael Belt and may be found in Appendix A.

3.2.3 Photodiodes

For the photodiodes in the coherent receiver work, the design used consists of a p-i-n junction with an absorptive intrinsic layer consisting of seven quantum wells with a 1540 nm bandgap. For an in-plane waveguide photodiode such as the one used in this work the quantum efficiency may be described as

$$\eta = \kappa(1-R)\frac{\Gamma\alpha_{IB}}{\alpha}(1-e^{-\alpha L})$$

where R is the reflection at the photodetector interface, κ is the coupling efficiency due to modal mismatch, Γ is the confinement factor of the mode within the absorption layer, α_{IB} is the inter-band absorption, and α is the loss coefficient [46]. The loss coefficient may be described as

$$\alpha = \Gamma\alpha_{IB} + \Gamma\alpha_{FC} + (1-\Gamma)\alpha_{FCx} + \alpha_s$$

with α_{FC} defining the free carrier absorption loss inside the absorption layer, α_{FCx} defining the free carrier absorption outside the absorption layer, and α_s defining the waveguide's scattering loss. If $\Gamma\alpha_{IB}$ is much greater than α_{FC}, α_{FCx}, and α_s, the quantum efficiency reduces to

$$\eta = \kappa(1-R)(1-e^{-\Gamma\alpha_{IB}L})$$

[46]. For an offset quantum well waveguide structure, the confinement factor of the mode within the quantum wells is 5.4% [44], and for an approximate 8500 cm^{-1} inter-band absorption, a 30 μm long photodiode will absorb 75% of the incoming light, and a 60 μm long photodiode will absorb 94%.

To minimize capacitance, photodiode electrical pads were designed to have a 60 μm diameter, the minimum for practical wire bonding. Using a thick low-K dielectric such as BCB the theoretical pad capacitance may be greatly reduced, and a dielectric thickness greater than 7 μm should result in roughly 10 fF of theoretical capacitance which closely matches the 20 fF theoretical capacitance of a 30x3.65 μm InGaAsP photodiode with a 1.2 μm depletion region. By keeping the wire bond lengths shorter 500 μm, the resulting photodiode circuit should be capable of greater than 30 GHz bandwidth, meeting the design specifications of the coherent receiver.

3.2.4 Polarization Diversity and Demultiplexing

An integrated polarization manipulation scheme has several useful applications in coherent reception. In a polarization diversity configuration, a receiver may operate independently of an incoming wave's polarization state by re-aligning incoming signals to the desired polarization, eliminating the need for active tracking and adjustment. In a polarization demultiplexing configuration, a receiver may decode information on two orthogonal polarizations at once resulting in double the data capacity.

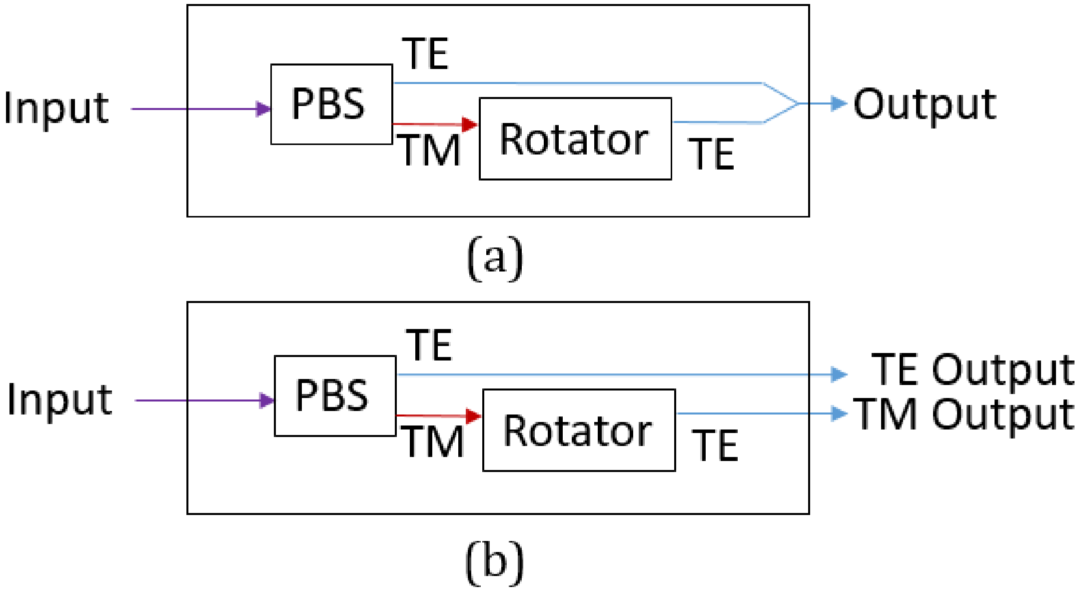

Figure 3.9. Block diagrams of (a) polarization diversity and (b) polarization demultiplexing circuits.

Block diagrams of polarization diversity and polarization demultiplexing circuits are presented in Figure 3.9 (a) and (b), respectively. In the polarization diversity circuit, an incoming signal is separated into its orthogonal transverse electrical (TE) and transverse magnetic (TM) components through a polarization beam splitter. The TM component is rotated 90° to a TE orientation and then recombined with the unconverted TE component, resulting in a fully TE polarized signal [47]. Similar to the polarization diversity circuit, a polarization demultiplexing scheme separates the incoming signal into TE and TM components through a polarization beam splitter and the TM component is then rotated 90° to a TE orientation. Unlike in the polarization diversity configuration, each component is then independently down-mixed and detected resulting in data reception on both polarizations.

Several structures have been proposed and demonstrated for integrated polarization demultiplexing on silicon; these have been summarized in [48] including MMIs, directional couplers, MZIs, photonic crystals, AWGs, and micro-ring resonators. On indium phosphide, polarization splitter implementations have been limited to metal-clad and modal birefringence directional couplers [49-51], metal-clad waveguide MZIs [52], asymmetrical waveguide directional couplers [53, 54], and quasi-state imaging effect in MMIs [55]. Of all these designs, the asymmetrical directional coupler design from [54] was chosen for its ease of integration, requiring no additional processing steps and only topographical waveguide redesign for compatibility with other components.

An asymmetrical directional coupler based on that from [54] is presented in Figure 3.10 with relevant design parameters. The splitter operates by using the birefringence of an indium phosphide waveguide to allow one polarization to couple to a higher order mode in a wider adjacent waveguide while preventing the other polarization from coupling due to beta mismatch. Another waveguide on the other side of the center waveguide transitions the coupled wave back to a low order mode.

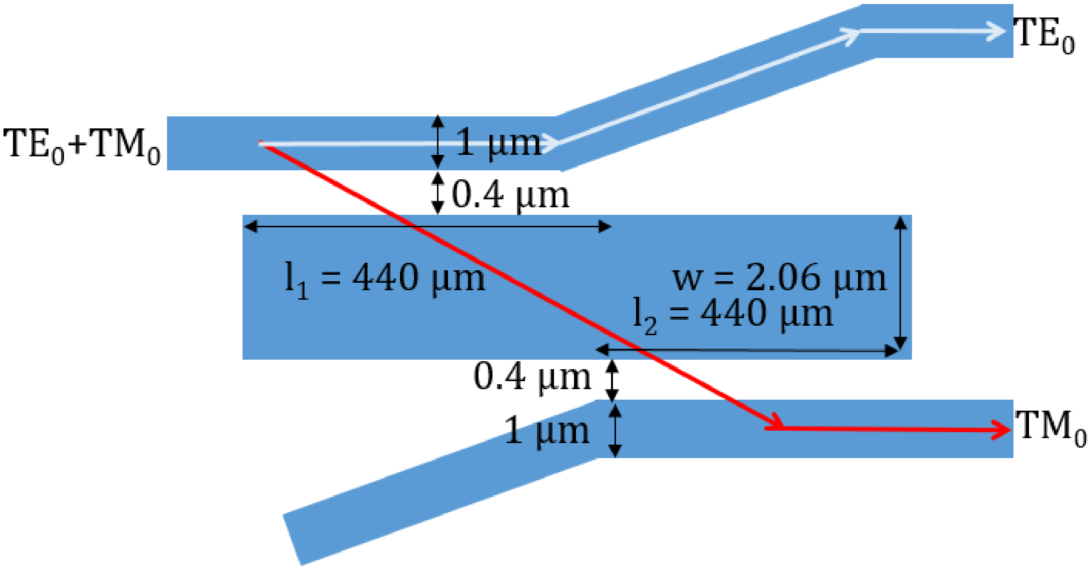

Figure 3.10. Schematic diagram of an asymmetrical directional coupler used for polarization splitting with relevant design parameters [54].

The directional coupler's performance was simulated using commercial FIMMWAVE mode solving software and covered the coupling of the TE_0 and TM_0 modes over a wavelength range from 1500 to 1600 nm. Simulated mode evolution propagating through the multi-mode section at 1525, 1550, and 1565 nm are presented in Figure 3.11. Simulated insertion loss of the TM_0 mode was plotted in Figure 3.12 from 1500 to 1600 nm showing useful operating range of roughly 65 nm from 1500 to 1560 nm; insertion loss for the TE_0 mode remained above 0.3 dB over the simulated wavelength range and was not plotted.

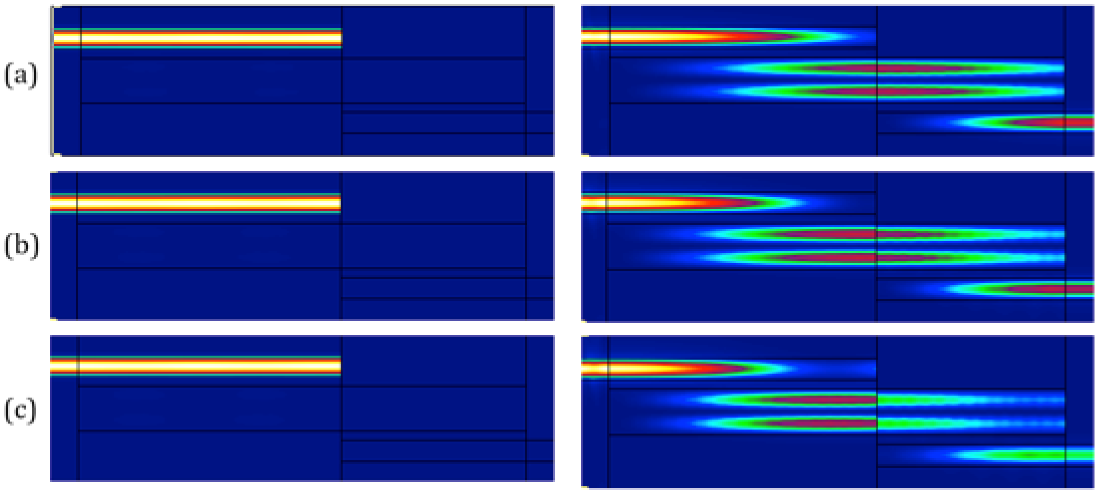

Figure 3.11. Simulated propagation of TE0 (left) and TM0 (right) modes through the polarization splitter of Figure 3.10 at (a) 1525 nm, (b) 1550 nm, and (c) 1565 nm. Simulation performed with FIMMWAVE mode solver software using the film mode matching (FMM) method.

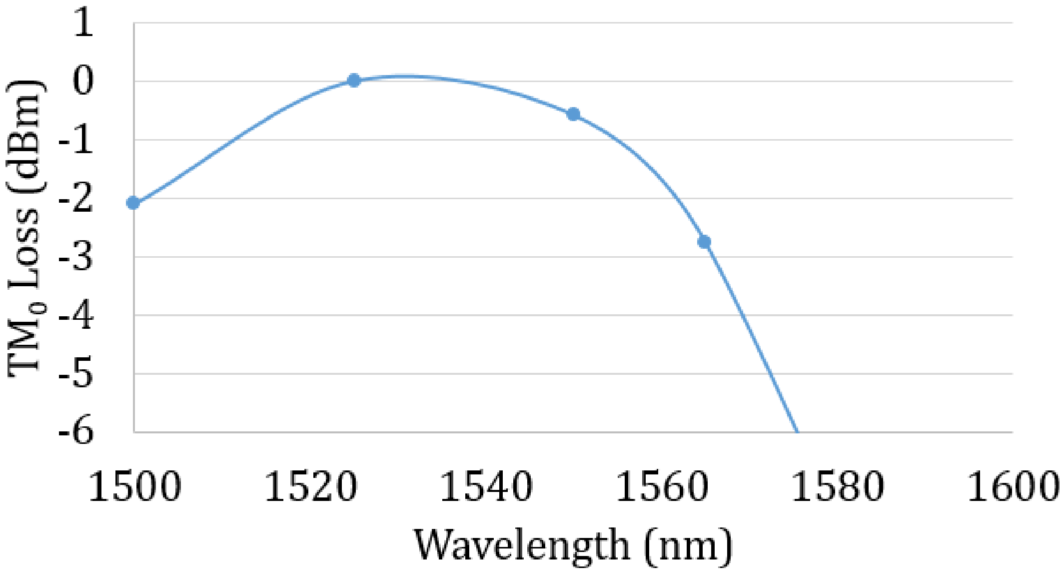

Figure 3.12. Simulated insertion loss of a TM0 mode passed through the polarization splitter of Figure 3.10. Simulation performed with FIMMWAVE mode solver software using the film mode matching (FMM) method.

After splitting, the TM mode must be converted to TE for improved receiver sensitivity in a polarization diversity scheme and for compatibility with TE-polarized LO output in a polarization demultiplexing scheme. The input and resulting output of a half wave plate capable of inducing a 90° polarization rotation is presented in Figure 3.13. The wave plate functions by using a birefringent crystal with an index difference Δn between two orthogonal components of a propagating mode. After length L_π, the two components of the wave will be shifted 180° out of phase with each other, resulting in a 90° polarization shift. The propagation length required to produce a 180° phase shift may be described as

$$L_\pi = \frac{\pi}{\beta_0 - \beta_1}$$

[56, 57] where β_0 and β_1 are the propagation constants of the orthogonal axes in the birefringent crystal.

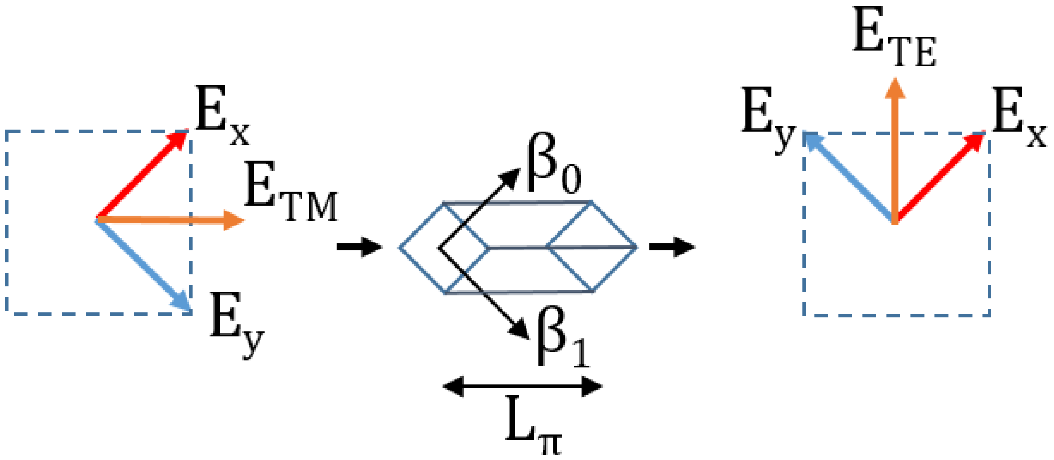

Figure 3.13. Diagram illustrating operation of a half-wave plate using a birefringent rotator such as that in [56]. An offset in the propagation constants of the x- and y- crystal planes induces a phase shift in the propagating wave converting its optical mode from a TM to TE orientation.

Several examples of on-chip polarization rotators have been demonstrated on indium phosphide [56, 58, 59] using asymmetrical waveguide structures to perform polarization mode conversion. For the work in this thesis, waveguide-based polarization rotators were explored due to their compatibility with the in-plane integration scheme utilized for the rest of the receiver components.

Two waveguide polarization rotator suitable for polarization rotation are presented in Figure 3.14 based on that in [56]. The rotators use an asymmetry in the waveguide's structure to introduce birefringence to the linearly polarized electromagnetic field. The birefringence produces a phase shift in the electromagnetic field due to the difference in effective index between the x- and y- components of the field with respect to the asymmetry's plane. After a certain propagation length, the electromagnetic field will be oriented 90° out of phase from its original orientation.

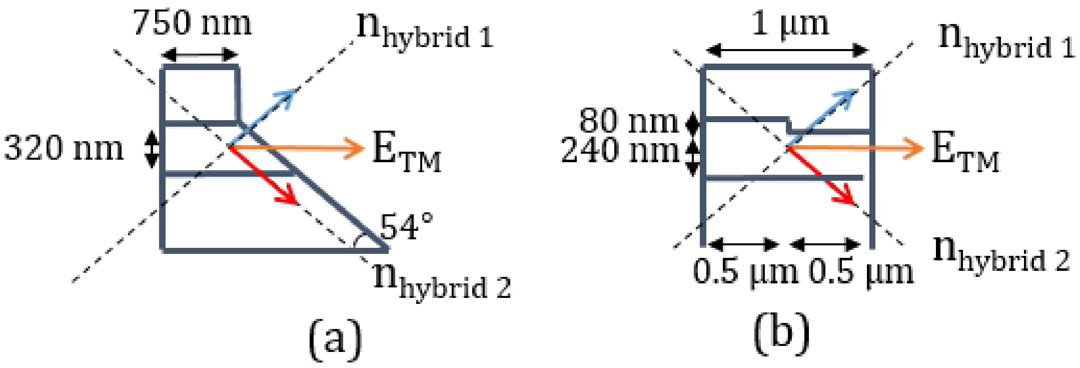

Figure 3.14. Diagram of two asymmetrical waveguide structures suitable for polarization rotation including relevant parameters [56].

A simulated mode evolution in the waveguide polarization rotator of Figure 3.14 (a) is presented in Figure 3.15 showing the top-down view of a waveguide utilizing a slanted sidewall to rotate the propagating mode with left and right images representing the TM and TE components of the electrical field, respectively. As the TM-polarized incident wave propagates through the rotator, the mode is converted to TE. Simulated excess loss of the TM-TE rotation is presented in Figure 3.16. To create a strong index difference, a strip waveguide geometry is required for stronger index contrast between the InP and air cladding. The width of the waveguide must also be minimized to maximize increase mode interaction with the air cladding. A width of 750 nm was the optimal trade-off between excess loss and large rotation coefficient; for this design the propagation length for a 90° polarization shift was 105 μm.

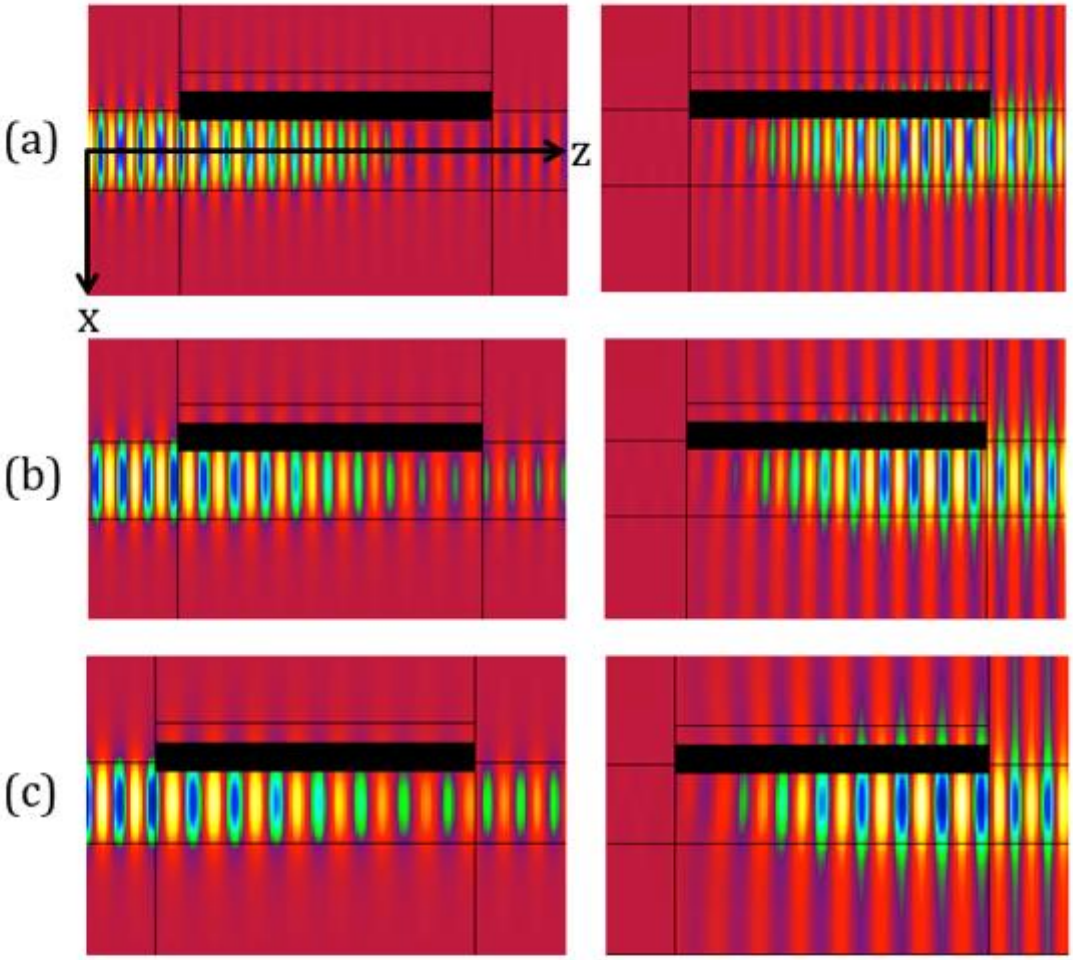

Figure 3.15. Simulated mode evolution of a TM_0 mode propagating through the polarization rotator design from Figure 3.14 (a) at (a) 1525 nm, (b) 1550 nm, and (c) 1565 nm. The images show top-down views of the TM and TE components on the left and right, respectively. Simulation performed with FIMMWAVE mode

solver software using the film mode matching (FMM) method.

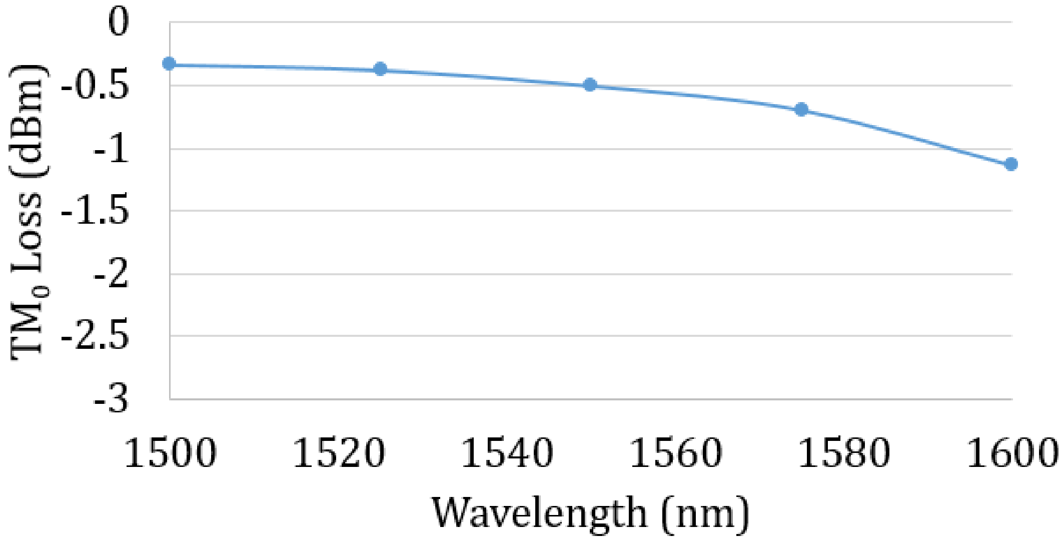

Figure 3.16. Simulated excess loss of a TM$_0$ mode converted to the TE$_0$ orientation through the polarization rotator design from Figure 3.14 (a). Simulation performed with FIMMWAVE mode solver software using the film mode matching (FMM) method.

Simulated mode evolution of a TM$_0$ mode propagated through the polarization rotator design from Figure 3.14 (b) is presented in Figure 3.17, and excess loss is plotted in Figure 3.18 over various wavelengths from 1500 to 1600 nm. For this design, a width of 1 μm introduced the optimal trade-off between interaction between the x- and y- components of the field and excess loss in the rotator, and the propagation length for a 90° polarization shift was 600 μm.

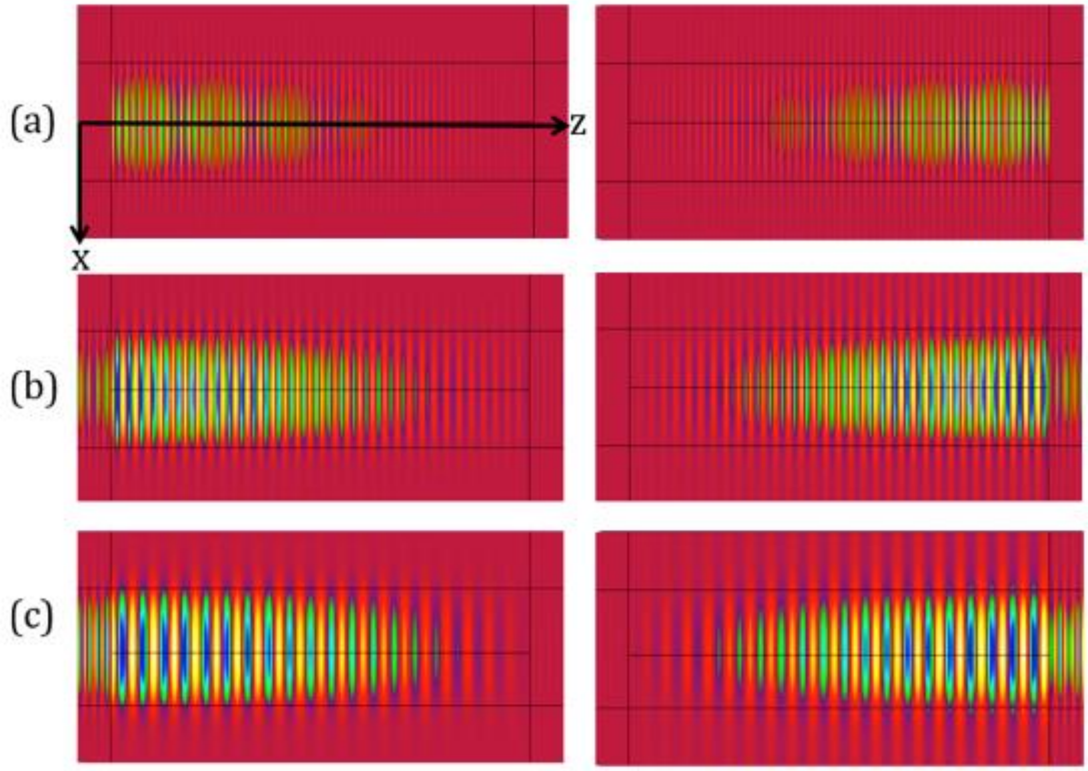

Figure 3.17. Simulated mode evolution of a TM$_0$ mode propagating through the polarization rotator design from Figure 3.14 (b) at (a) 1525 nm, (b) 1550 nm, and (c) 1565 nm. The images show top-down the TM and TE components on the left and right, respectively. Simulation performed with FIMMWAVE mode solver

software using the film mode matching (FMM) method.

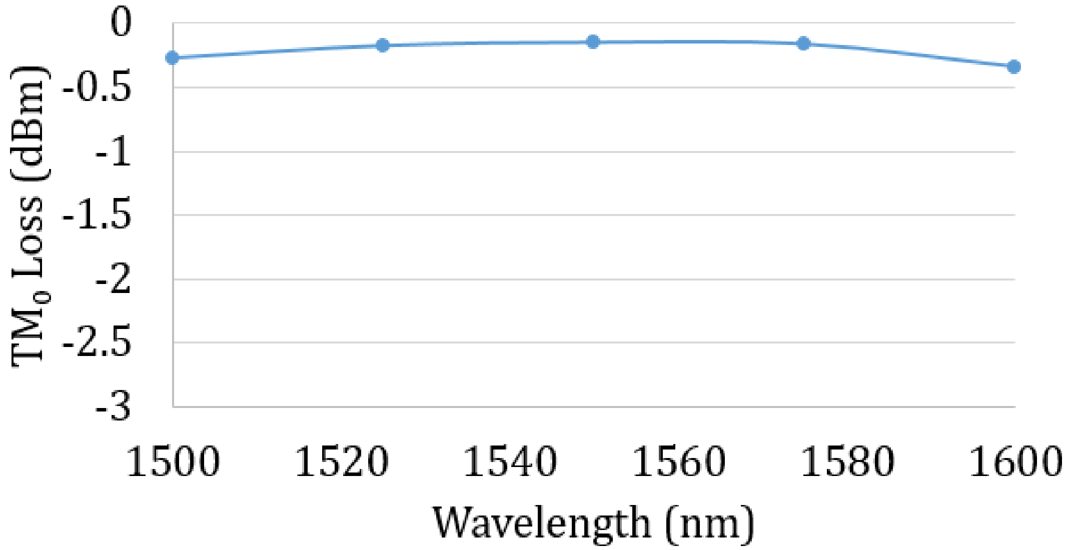

Figure 3.18. Simulated excess loss of a TM_0 mode converted to the TE_0 orientation through the polarization rotator design from Figure 3.14 (b). Simulation performed with FIMMWAVE mode solver software using the film mode matching (FMM) method.

3.3 Chapter Summary

In this chapter, overall design for several building blocks required for a coherent receiver were discussed. Theory for building blocks including the 90° optical hybrid, local oscillator, photodiodes, polarization splitter, and polarization rotator was described and critical design parameters for the components were derived. With the theoretical design of the coherent receiver components complete, theoretical design of the all-optical switch may now be discussed.

Chapter 4

Design of a Monolithically Integrated Tunable Optical Router (MOTOR)

4.1 Monolithically Integrated Tunable Optical Router Requirements

There are several attributes needed for the design of the monolithically integrated tunable optical router; broadly speaking, these break down into two categories: optical gain and propagation loss. The tunable switch consists of 6 overall functional blocks: an SG-DBR laser switchable wavelength source, linear and nonlinear semiconductor optical amplifiers, arrayed waveguide grating router, delay line, and interconnecting waveguides and splitters. Figure 4.1 summarizes their necessary characteristics sorted by broad category. For the SG-DBR laser, optical gain is necessary to allow for stimulated emission of photons as well as efficient electrical pumping to facilitate current injection into the gain material. Large optical confinement is also desired for more efficient use of the available gain in the laser, and high index tuning efficiency is needed for efficient mirror tuning. Two different types of on-chip amplifiers are desired, both requiring optical gain. The linear amplifiers require small optical confinement to prevent distortion from gain saturation, and the nonlinear amplifiers require large optical confinement to facilitate gain saturation which serves as the mechanism for wavelength conversion.

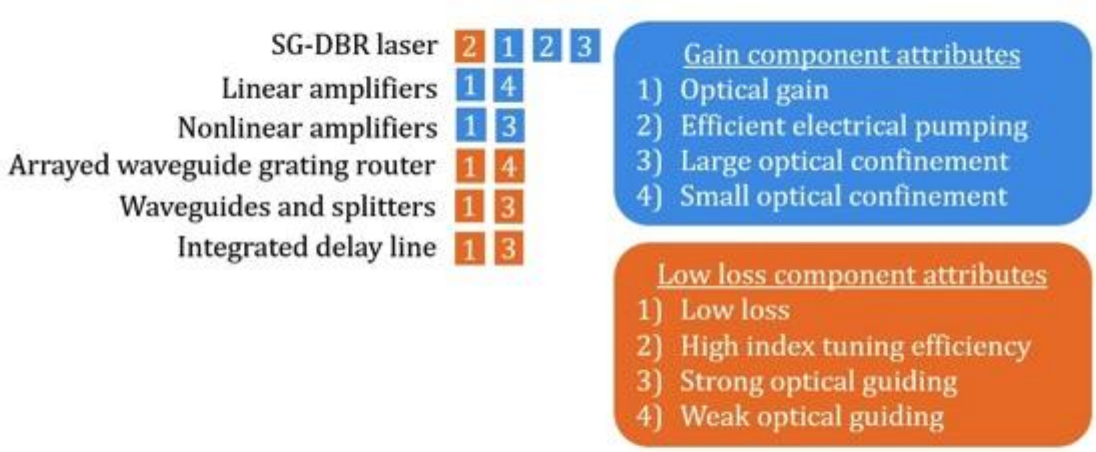

Figure 4.1. Summary of the components for a monolithic tunable optical router and each of their required attributes organized by 2 broad categories: gain and low loss.

In the arrayed waveguide grating router, sufficiently low loss is required to enable routing of the incoming signal without significant attenuation and weak optical confinement to minimize propagation loss. The splitters, waveguides, and integrated optical delay lines require low loss and strong optical guiding to connect all of the interacting components and propagate the optical signals through the chip without excess attenuation. Indium phosphide was chosen to integrate all of the necessary components, as it provides the best trade-off between integrating high gain functionality with low enough loss for larger passive functions.

4.2 Monolithically Integrated Tunable Optical Router Components

Now that the overall requirements for the design of the tunable optical router have been defined, the individual components required for operation may be described. These are the SOA-based optical-optical Mach-Zehnder modulator, pump source laser, and AWGR.

4.2.1 Mach-Zehnder Modulator

The primary component in the tunable optical router is the Mach-Zehnder modulator (MZM). A diagram of the modulator's operation is presented in Figure 4.2 consisting of a Mach-Zehnder interferometer with SOAs on each arm. In static operation, a CW pump source is split into two equal signals in a 1x2 MMI. Each signal is then passed through an SOA amplifying the signal. A π phase shift is introduced to the upper arm, and the signals are recombined in a 2x1 MMI causing deconstructive interference to cancel out the signal, dissipating its power into the substrate. In this state, the output of the MZM is in the 'off' condition.

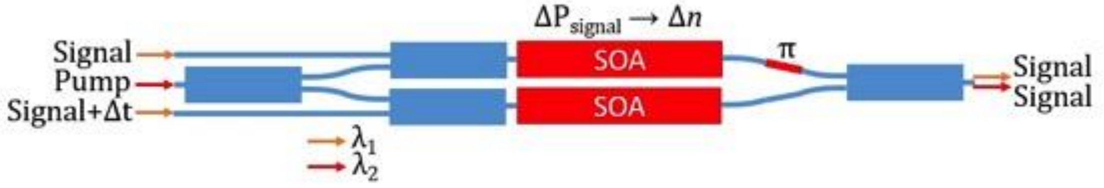

Figure 4.2. Block diagram of the optical-optical Mach-Zehnder modulator (MZM).

By introducing another signal into the upper arm of the modulator, some of the carriers in the upper SOA are stimulated into recombination by the new signal. This induces a change in the carrier density within the waveguide of the SOA and induces a phase change through the electro-optic effect. If a large enough signal is input into the SOA, a full π phase shift may be induced in the upper arm allowing the pump signal to constructively recombine in the output MMI, putting the MZM into the 'on' condition resulting in optical-optical modulation.

The speed of the modulator is limited by the gain recovery time. a measure of the length of time for the pump output power to respond after the input signal has been switched from on to off. The recovery time is primarily determined by the ratio of optical gain to the current density into the SOA, as the carrier recovery time is largely fixed by the fundamental carrier generation process. Simply put, if more gain is produced from a given current density, a larger swing in the pump signal may be produced resulting in a faster transition time. It is therefore beneficial to have large optical confinement in the SOAs used for the wavelength conversion process to maximize mode overlap with the gain material and produce more gain.

To overcome the fundamental limitations of gain recovery time, a push-pull configuration may also be implemented where part of the input signal is split off, delayed, and then fed to the lower arm of the MZM. This causes the pump signal in the lower arm to match the optical power of the upper arm after a delay causing destructive interference in the output and ‘pulling down’ the output state from on to off much faster than possible with a single-ended configuration. By choosing a delay length to match the pulse length desired, switching speeds much faster than the gain recover time can be achieved.

4.2.2 Tunable Pump Laser

A tunable laser is required to choose the pump wavelength determining the output of the MZM switch. Similar to the laser used in the coherent receiver, the source in the tunable optical router requires a wide wavelength range to facilitate an equally large array of selectable outputs. Since the laser must also be monolithically integrated onto the switch, an SG-DBR design was chosen as it allows for a wide tuning range while integrating all components on-chip. The same design described in Section 3.2.2 was used in the router.

There are a few requirements that differ from that of the coherent receiver implementation. Since the router’s signals are not coherent, the phase noise is not a critical aspect of the laser, but instead the switching speed of the laser is critical to the performance of the switch. For this application, electro-optically tuned SG-DBR mirrors are superior to thermo-optic solutions as the switching time is much faster. For an electrically pumped SG-DBR laser, the time to switch between supermodes is typically 10-15 ns [60], while that for a thermally tuned mirror is slightly less than 300 μs [61]. Laser stability is also important as it must remain within a narrow passband in the AWGR for proper routing and minimal channel cross-talk.

4.2.3 Arrayed Waveguide Grating Router (AWGR)

The final piece of the all-optical switch is the wavelength-selective router based upon an arrayed waveguide grating router (AWGR) or phased-array (PHASAR) structure such as that from [62]. Figure 4.3 presents a diagram describing the AWGR's operation.

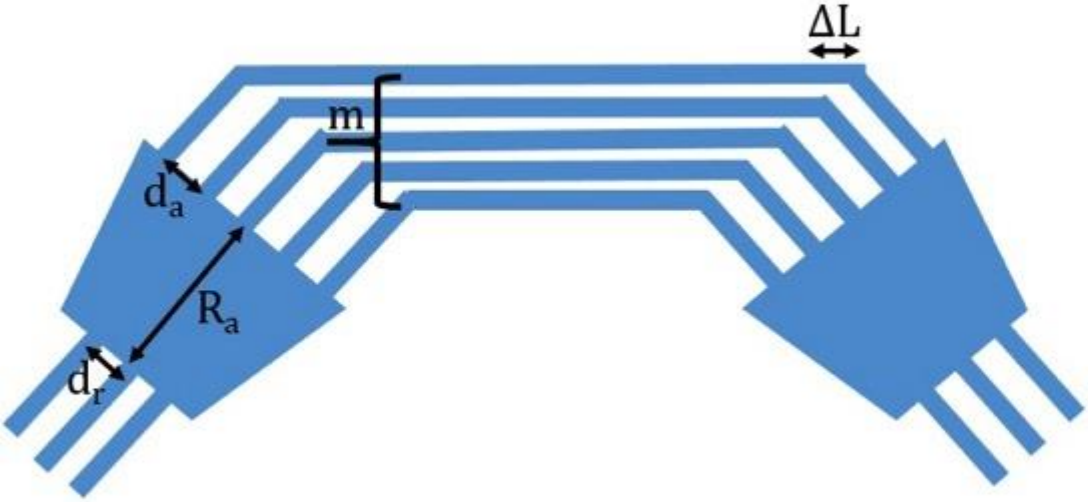

Figure 4.3. Illustration of an arrayed waveguide grating router [62].

The AWGR's design and derivation of parameters follows that described in [62]. The AWGR consists of two star couplers and an array of waveguides between them with varying lengths ΔL. As light enters the star coupler from one of the inputs, the mode is no longer guided and spreads out, producing an image on each of the star coupler's output waveguides. Each image is then propagated through the arrayed waveguides with path lengths varying from ΔL to $m \cdot \Delta L$ where m is the number of waveguides in the array and ΔL is specified for a center wavelength λ_c by

$$\Delta L = \frac{m\lambda_c}{N_g}$$

where N_g is the group index of the waveguide mode. An input signal with wavelength λ_c will cause constructive interference in the output star coupler at the mirror-image output port while other wavelengths will cause the constructive interference pattern to shift to adjacent output ports, thus producing the wavelength routing functionality. To avoid dropping signals beyond the outer output ports, the AWGR has a repeating free spectral range described by

$$FSR = \frac{c}{N_g m \Delta L} = m \Delta f_{ch}$$

where c is the speed of light.

To allow for the image to reach all of the desired outputs in the star coupler, its length must be set long enough to allow the mode to fully diverge. The required length can be expressed as

$$R_a = \frac{N_{star} d_r d_a N}{\lambda_c}$$

where N_{star} is the effective index in the star coupler and d_r and d_a are the pitch of the output and input ports of the star coupler, respectively. Finally, the number of waveguides in the array can be optimized as given by

$$N_a = \frac{2\theta_a R_a}{d_a} + 1$$

where θ_a is the aperture width. As the aperture width is typically 2-3x the width of a Gaussian far-field θ_0 according to [63], this can be approximated by

$$\theta_0 \approx \frac{\lambda_c}{N_{star}} \frac{1}{w_{wg}\sqrt{2\pi}(0.5 + \frac{1}{V - 0.6})}$$

as described in [62] where w_{wg} is the width of the input waveguide and V is the V-parameter, an empirically determined fitting term to estimate the effective width of the waveguide [62].

4.3 Chapter Summary

In this chapter, overall design of several building blocks required for an all-optical switch were discussed. Theory for building blocks including the Mach-Zehnder modulator, tunable pump laser, and AWGR was described and critical design parameters for the components were derived. With the theoretical design of both the coherent receiver and all-optical switch components complete, fabrication considerations for both devices may now be discussed.

Chapter 5

Integration Platform and Fabrication

5.1 Integration Platform

To meet the monolithic design goal of the coherent receiver and all-optical switch, selection of a suitable integration platform was required to fulfill all integration requirements. Several integration platform technologies and their advantages and disadvantages are presented in Figure 5.1, including indium phosphide PICs [26], silicon photonics [28], glass silica planar lightwave circuits (PLCs) [64, 65], and hybrid III-V/silicon PICs [27,29]. In general, there are three primary attributes vital to the performance of optical devices: high gain, high speed, and low loss. As the only direct bandgap material, indium phosphide provides the best available gain performance by far but also has higher loss due to high doping for efficient current injection [66]. Glass silica PLCs demonstrate the lowest propagation loss [64], enabling high performance passive components such as AWGRs and optical hybrids, but cannot be electrically pumped for gain due to the insulating nature of the silica waveguide. Recent work, however, has demonstrated gain through the use of erbium-doped waveguides [65], showing promise for active component integration on the platform. Silicon photonics leverages the maturity of silicon processing technology to enable high speed and low loss components, but as an indirect bandgap material, native gain on silicon has been difficult to realize. To address this, recent work has been done to bond III-V material onto high performance silicon photonic circuits allowing for evanescent coupling to the active material and leveraging the best of both III-V and silicon systems [67, 68]. Although promising, this platform is relatively new. Of all the platforms, silicon and silica are the most mature, as they are able to leverage existing technology from the silicon electronics industry to enable both commercial products and robust foundry services, while indium phosphide has a maturity in between the two, having commercial devices available and a nascent foundry model.

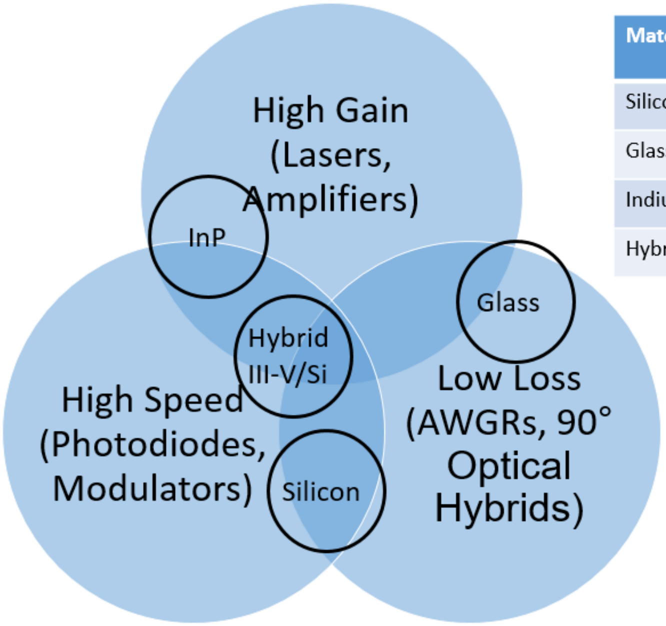

Material Platform	Commercial Process Maturity
Silicon	High
Glass	High
Indium Phosphide	Medium
Hybrid III-V/Si	Medium

Figure 5.1. Diagram presenting the strengths and weaknesses of several material platforms available today for photonic integration, along with their relative commercial process maturity [26-29, 64, 65] .

Based on the state of each platform and the requirements of coherent receiver and all-optical switch, indium phosphide was chosen for the availability of high gain to enable on-chip lasers and amplifiers critical to the performance of both devices while still allowing for high speed photodiodes and modulators. Several integration strategies have been explored on indium phosphide which broadly include simultaneous active/passive component integration through selective placement/activation/passivation of a quantum well gain material, but the two that have been focused upon at UCSB are offset quantum well (OQW) and quantum well intermixing (QWI) described in [66]. The offset quantum well approach benefits from a relatively simple fabrication scheme as the quantum wells are simply wet etched away in the passive areas of a chip prior to a blanket InP cladding regrowth [69]. The OQW approach also has a larger gain saturation power in on-chip SOAs due to lower confinement of the off-center location of the quantum wells relative to the waveguide. The QWI approach, on the other hand, has higher confinement due to the centered location of the quantum wells in the waveguide layer resulting in higher gain than a comparable OQW structure, but this comes at the cost of a lower gain saturation power and increased process risk as it requires a phosphorus implant to de-activate the quantum wells in the passive areas of a chip [66]. The QWI approach has also been demonstrated without a regrowth step [70], thus reducing production cost; merits of these platforms have been rigorously studied in [44, 71, 72].

For the work in this thesis, the regrowth-free QWI process of [70] was not yet available, so the offset quantum well platform was ultimately deemed the safer approach for getting high yield on the largely integrated coherent receiver and all-optical switch due to its relatively lower risk process. This allowed for the majority of design and testing to be focused on device architecture and fabrication instead of growth characterization. While the higher gain of the QWI platform would have been useful for more efficient laser and amplifier operation and would have ultimately resulted in much better performance in the all-optical switch in particular, at the time it was deemed unnecessary and the phosphorus implant step riskier than the etch used in the OQW process to remove the active layer.

5.2 Epitaxial Design

The epitaxial structure serves as the basis of the PIC and must be designed to support all of the desired PIC functions in conjunction with each other; broadly, these requirements include: optical guiding with minimal radiative loss to enable multiple interconnected functions on a single die; simultaneous integration of both active and passive sections to enable amplifying and absorbing functions as well as low attenuation; and efficient current pumping to facilitate amplification and absorption, again without any significant degradation of the mode propagation.

The epitaxial structure used for integration of the coherent receiver and all-optical switch is described in [70], details of which are presented in Table 5.1. The core of the waveguide for transverse confinement consists of a 320 nm thick layer of InGaAsP designed with a bandgap at 1.4 μm which serves as a compromise between low absorption loss and efficient index tuning [44]. The waveguide is clad by indium phosphide on top and bottom. A layer of 7 quantum wells is grown above the waveguide layer with a 1545 nm peak luminescence at room temperature for operation over the C-band. Temperature control of the device is critical, as heating will result in red shifting of the PL and adversely affect the performance of the device. To define the active and passive regions, the quantum well layer is etched away in all areas except where needed to avoid excess propagation loss. There are several advantages to a quantum well gain region as opposed to using bulk gain material. When current is injected into the diode, the heterojunctions confine the carriers, thus increasing carrier density and improving radiative recombination and thus the efficiency of the device. In addition, a compressive strain on the quantum wells results in even further gain improvement [73].

Table 5.1. Epitaxial structure of an offset quantum well device [70].

Layer	**Material $In_xGa_{1-x}As_yP_{1-y}$**		**Strain (ppm)**	**Thickness (nm)**	**Doping (cm^{-3})**	**PL λ (nm)**
	X	**Y**				
Contact	0.53	1	0	100	>2e19(p)	-
p-Cladding	1	0	0	2200	>1e17(p)	-
Setback	1	0	0	50	UID	-
SCH	0.7676	0.5039	0	25	UID	1226
Barrier(7x)	0.735	0.513	-2050	8	UID	1220
Well (7x)	0.735	0.835	8800	6.5	UID	1545
Barrier	0.735	0.513	-2050	8	UID	1220
Stop Etch	1	0	0	15	UID	-
Waveguide	0.6514	0.7377	-400	320	3e17(n)	1384
Substrate	1	0	0	150000	5e18(n)	-

To facilitate current injection, the substrate and waveguide layer are n-doped with sulfur and the upper cladding layer is p-doped using zinc to form a diode. This forms a p-n junction in areas without the quantum wells, and a p-i-n junction with the quantum wells, as the quantum well layer is unintentionally doped. The p-doping in the upper cladding is graded from a lower doping concentration nearest to the waveguide layer ($7x10^{17}$ cm^{-3}) up to $1x10^{18}$ cm^{-3} at the top; this is done to reduce the inter-valence band absorption caused by the zinc dopant. The top of the upper cladding is capped off with a 100 nm thick layer of highly p-doped ($>2x10^{19}$ cm^{-3}) p-InGaAs to facilitate formation of an ohmic contact when metal is deposited during processing. InGaAs is chosen as it has the smallest band-gap of all materials that can be lattice-matched to indium phosphide to help minimize the formation of a Schottky barrier at the junction. As the InGaAs layer is highly absorptive, the InP upper cladding is 2 μm thick to minimize loss from evanescent coupling.

With the epitaxial structure defined, all of the requirements for an integrated coherent receiver and all-optical switch may be realized. An optimized waveguide layer allows for several different optical elements to be integrated onto a single die in series using interconnects. Selective placement of the quantum well layer across the chip makes possible simultaneous integration of active and passive optical elements, and a doping profile tailored for low-resistance diodes allows facilitates efficient current injection of the device. With the material platform fully developed, the layout and fabrication process may now be explored.

5.3 Fabrication Overview

A visualization of the complete fabrication flow is presented in Figure 5.2. Several steps are required to fabricate all of the necessary components; broadly these are: active/passive definition, grating etch, upper cladding regrowth, waveguide etches, dielectric depositions, via definitions, metallization, electrical isolation, substrate thinning, and cleaving. Descriptions of each fabrication step are listed in Table 5.2 including methods used to perform each step, critical dimensions, and equipment required. The order of these steps is critical to allow interoperability and avoid steps interfering with each other.

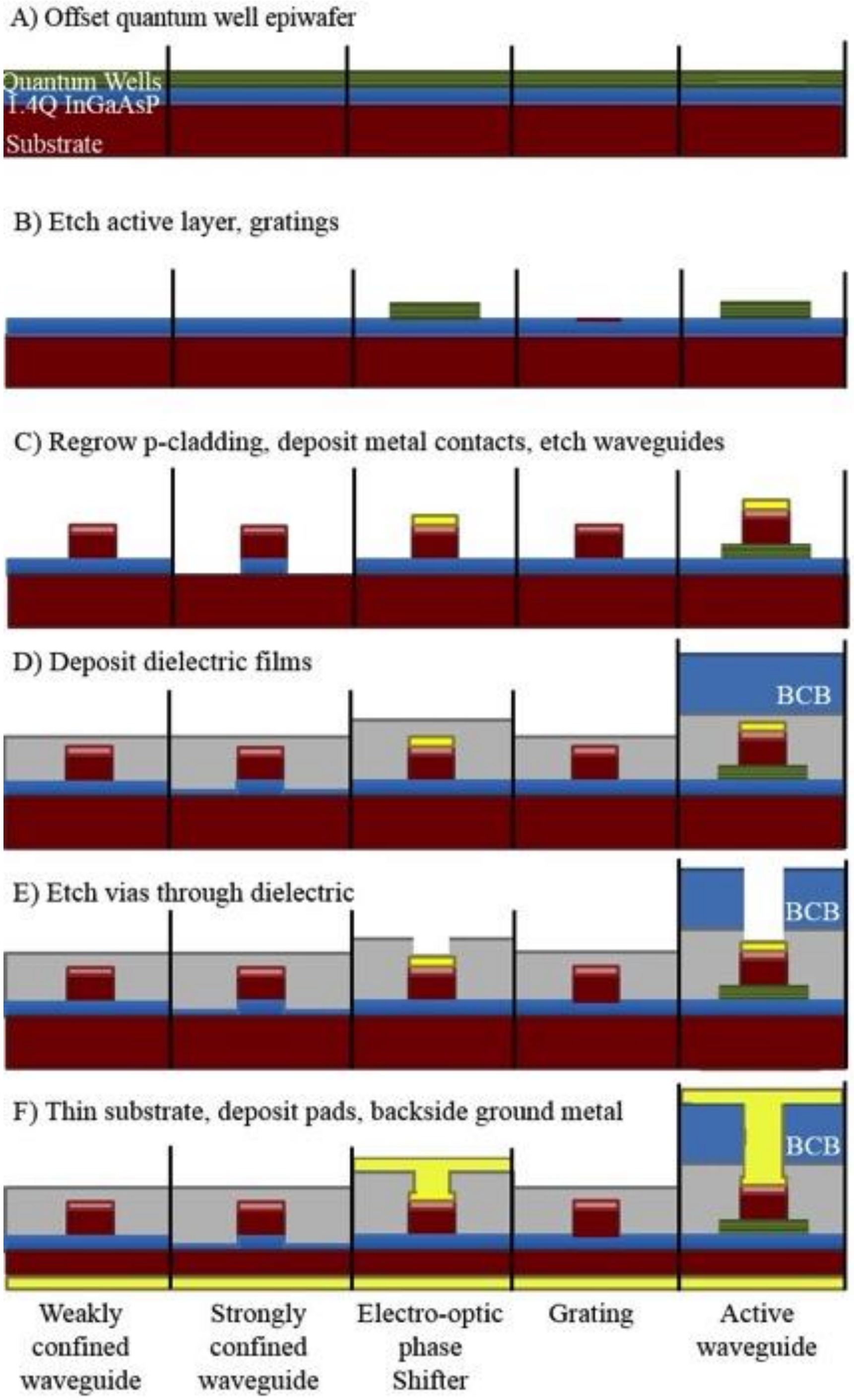

Figure 5.2. Illustration of device fabrication flow.

Starting with an epiwafer, the quantum well layers are first removed with a H_2SO_4:H_2O_2:H_2O 1:1:10 wet etch in all areas except where gain and absorption is desired. The wet etch is selective and will only etch the quaternary quantum well material, stopping on a thin layer of InP placed just above the waveguide layer. A protective InP capping layer must also be removed prior to the quantum wells using an H_3PO_4:HCl 3:1 wet etch. It is essential at this point to verify that the quantum wells are fully removed as they cannot be corrected after the regrowth has been done. Next, gratings are etched into the waveguide layer using reactive ion etching with a methane/hydrogen/argon gas mixture of 4/20/10 sccm at 75 mT to form the feedback for the SG-DBR lasers. The gratings are only etched 80-100 nm into the waveguide layer to ensure that the regrowth will properly fill them. For both etches, silicon nitride is used as a hard mask, which is subsequently removed in hydrofluoric acid (HF). The surface is then etched with a short H_2SO_4 dip to ensure surface cleanliness and regrown with an upper cladding.

Table 5.2. Process steps involved in the fabrication of the coherent receiver and all-optical switch.

Process Step	Method/Equipment Used	Critical Features
Quantum Well Etch	i-line stepper H_2SO_4:H_2O_2:H_2O 1:1:10 wet etch	Etch depth
Grating Etch	Electron beam lithography with $CH_4/H_2/Ar$ RIE etch using SiN_x hard mask	Duty cycle, grating pitch, depth
p-Cladding Regrowth	MOCVD reactor, external vendor	Surface preparation
p-Contact Deposition	i-line stepper, electron beam deposition	Surface preparation
Ridge Etches	PECVD SiO_2 deposition, i-line stepper, CHF_3 ICP etch, 200°C $Cl_2/N_2/Ar$ ICP etch, H_3PO_4:HCl 3:1 wet etch	Sidewall roughness, angle, etch temperature
BCB Dielectric Deposition/Via Etch	Photo-BCB, i-line stepper, O_2/CF_4 ICP etch, PECVD SiN_x deposition, CF_4/O_2 ICP etch	Dielectric thickness, via width
p-Pad Deposition	i-line stepper, electron beam deposition	Metal adhesion, sidewall coverage
Isolation Etch	i-line stepper, 3:1:50 H_3PO_4:H_2O_2:H_2O wet etch	Complete InGaAs removal

Once regrowth is complete, metal contacts are immediately deposited onto the unprocessed surface to avoid any contamination; throughout the fabrication flow, dielectric hard masks consisting of either silicon dioxide or silicon nitride are necessary to mitigate photoresist degradation during high temperature etches. An unwanted side effect of the hard mask deposition is hydrogen implantation due to the presence of SiH_x as a precursor for the formation of the dielectric, which releases hydrogen as a byproduct. At high temperatures utilized in plasma enhanced chemical vapor deposition (PECVD), the hydrogen gas can permeate into the upper layer of the semiconductor and bind with the zinc ions. The contacts are deposited prior to any dielectric deposition to avoid this issue altogether.

Once the metal contacts have been formed, the waveguide features are defined using a PECVD-deposited 700 nm thick SiO_2 hard mask and etched into the semiconductor using a $Cl_2/N_2/Ar$ inductively coupled plasma (ICP) etch at 200°C; as the etch only has a 5:1 selectivity with SiO_2, a thick dielectric layer is required. Two different waveguide geometries are implemented serving different functions on the chip. The first consists of a strip waveguide where etching penetrates past the waveguide layer to form a strongly guiding waveguide useful for tight bend radii. The second geometry stops the etch at the surface of the waveguide layer resulting in a weakly guiding waveguide which reduces the mode overlap with the edge of the waveguide to reduce loss.

Once the waveguides have been defined, a 300 nm thick layer of Si_3N_4 is deposited over the entire chip, isolating the devices from the probe metal which will be deposited on top. In areas where high speed is desired, an additional layer of BCB 7.5 μm thick is deposited to further reduce pad capacitance. Via openings are then etched into the dielectric material using a CF_4/O_2 ICP etch to allow for electrical contact in desired areas, and a metal stack of titanium, platinum, and gold is then deposited to connect to the small metal contacts. This layer is laid out with a large surface area to facilitate probing and wire bonding.

After the metallization, the top InGaAs layer is etched away on either side of each pad using H_3PO_4:H_2O_2:H_2O 3:1:50 to electrically isolate adjacent devices from each other. The chip is then implanted with hydrogen ions to provide further isolation between devices using the thick metal as a hard mask.

Once implanted, the wafer's substrate is thinned to 100-150 μm to facilitate cleaving and a titanium/platinum/gold coating is deposited on the backside to form a common ground. The devices are then cleaved, forming smooth edge facets for interfacing the on-chip waveguides to a lensed fiber. Significant characterization of several steps in the process flow was performed to optimize their order, execution, and minimize detrimental interactions as described in the following sections.

5.3.1 Lithography

I-line lithography was used for all of the process steps except for the gratings, which required electron beam lithography in order to resolve the 118 nm half-pitch resolution. The i-line stepper used was capable of producing features down to a 400 nm critical dimension size, which was more than sufficient for both the coherent receiver and all-optical switch designs. As the stepper was also capable of <150 nm alignment tolerance, direct via alignment to the tops of the waveguides was performed. This alignment tolerance is enabled by a dark field alignment system (DFAS), which measures the alignment die-by-die and then makes corrections to the user alignment. The DFAS system was particularly useful in minimizing the offset at transitions between the two waveguides, as larger misalignment between them results in unwanted reflections and increased loss. The stepper was also capable of wafer leveling, which improved the resolution precision, allowing for large device footprints without variation of the critical dimensions across the die. The leveling also improved feature uniformity across the wafer resulting in higher yield across each die.

5.3.2 Gratings

The gratings are a critical component of the SG-DBR laser and require a carefully calibrated period, duty cycle, and depth in order operate as desired. Because the half-period of the gratings is ~118 nm, which is beyond the capabilities of i-line steppers, electron beam lithography must be used for their definition. To determine the optimal exposure settings, a dose calibration was performed by varying the electron beam dosage on a dummy sample that was then etched in the same manner as the real device. The resulting duty cycles were then measured in a scanning electron microscope (SEM) and the dose yielding a duty cycle closest to 50% was found. Two grating calibrations are shown in Figure

5.3 including a 40% and 50% duty cycle example on the left and right, respectively; the dose conditions for the 50% duty cycle were ultimately chosen. The gratings were then etched using a methane/hydrogen/argon gas mixture in an RIE tool; this etch tool was useful for its slow etch rate, relatively small etch surface roughness, and minimal trenching.

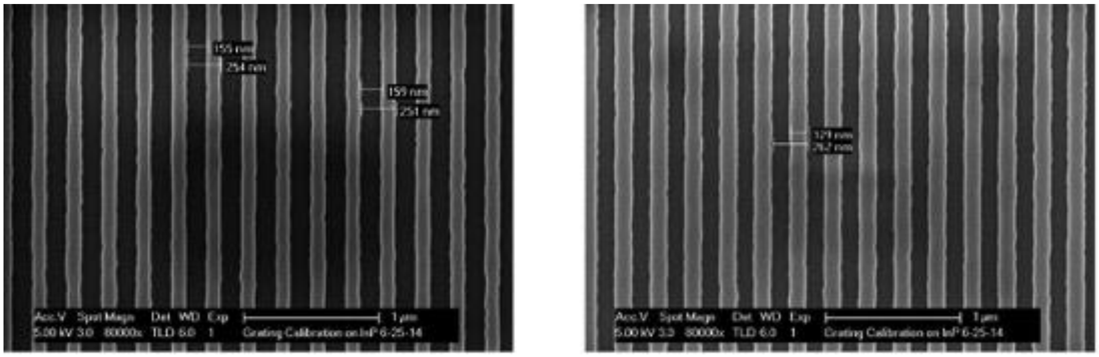

Figure 5.3. Comparison of two different duty cycles resulting from the grating calibration. The grating on the left has a 40% duty cycle resulting from overexposure, which the grating on the right has a 50% duty cycle.

The depth of the gratings must be monitored between etches using atomic force microscopy (AFM) as shown in Figure 5.4. The AFM measures the deflections of a probe with a ~10 nm tip as it is tapped along the surface of the device. As the depth of the grating must not exceed 100 nm, it was critical to monitor the etch progress.

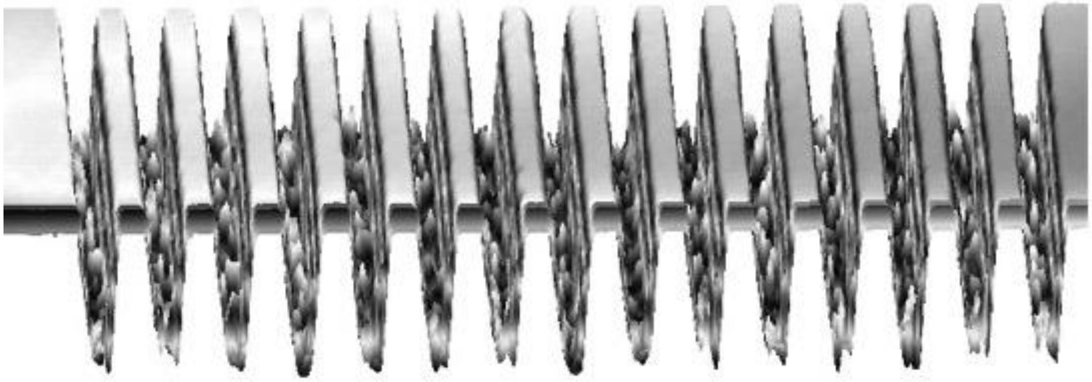

Figure 5.4. 3D image of a grating prior to regrowth measured by AFM.

5.3.3 Regrowth

Surface preparation prior to regrowth was crucial for good device performance; cases of silicon contamination at the regrowth interface have been documented in [63] due to improper surface preparation that resulted in the formation of a p-n junction at the regrowth interface and subsequently poor diode performance. Several steps were used to ensure the surface has been properly treated. First, the wafer was etched in HF for 5 minutes to remove any residual dielectric material. After this step, the wafer was etched for a brief amount of time in a sulfuric acid to lightly etch back the quaternary waveguide and quantum well layers, rinsed in distilled water, and again air dried. Between wet etches, the wafer was exposed to a high temperature O_2 plasma at 250° C to dehydrates the surface and remove residual polymers such as photoresist. The high temperature plasma also causes the surface to become hydrophilic, enabling a more repeatable etch.

An SEM image of a properly cleaned surface is presented in Figure 5.5 (a) showing no residual dielectric or polymer on the surface.

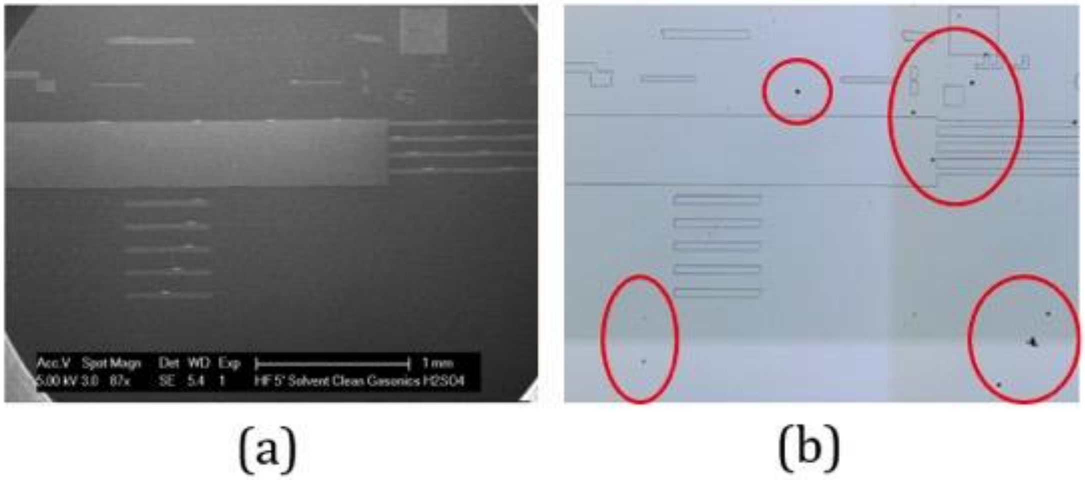

Figure 5.5. Images of the wafer surface (a) prior to regrowth showing no visible defects or particles on the surface and (b) after regrowth revealing significant surface contamination similar to that found in [60].

The wafer was then vacuum sealed for transfer to an MOCVD reactor. Regrowths for all of the devices were performed by MOCVD at III-V Labs. Immediately prior to regrowth, the external vendor performed a short HF etch and sulfuric acid etch to remove any native oxide that may have built up on the device during shipping.

After regrowth, the surface was microscope inspected for defects. For the switch and test structure device run, the regrowth had little to no surface defects, but the receiver run encountered significant surface defects after the regrowth as shown in Figure 5.5 (b). These devices were fabricated to completion as the effect of the defects was an unknown, but diode testing of the wafer revealed significant shunt resistances in areas close to the defects allowing current to bypass the diodes and shorting the devices. A linear correlation between the proximity to a defect and the value of the shunt resistance implicated the defects as the source of the shunt resistances, and similar defect densities and their effects have been studied in [60] resulting from inadequate preparation of an MOCVD reactor prior to regrowth. As the reactor heats up to growth temperature, the metal sidewalls expand, causing any material on them to break off and redeposit on the wafer surface causing surface masking preventing regrowth and creating a shorted path to the waveguide layer. Cleaving adjacent devices apart from the surface defect removed shunting and greatly improved device performance. As such, the defects had little effect on isolated on-wafer test structures but devastating results on the larger coherent receiver PICs. Out of 16 individual receiver devices that were fabricated on the wafer, only 2 exhibited low enough shunt resistance for full operation, resulting in a 12.5% yield. The shunt resistance was particularly prevalent in most of the gratings for the SG-DBR lasers, indicating that the gratings also may not have been correctly filled during regrowth.

As the regrowth can be one of the most difficult steps in chip fabrication, it is best to perform in-house as often as possible in order to minimize risk. However, it is costly to maintain a MOCVD reactor without running large amounts of devices, and it requires a dedicated operator to maintain and run the tool. For this reason, an external vendor was used for the growth, as the risk was deemed necessary due to prohibitive cost of in-house fabrication. For a commercial enterprise focused on PIC development, it is optimal to perform regrowth in-house to ensure high yields.

5.3.4 Waveguide Etching

In the all-optical switch, the same methane/hydrogen/argon RIE etch used for the gratings was implemented to create the device's waveguides. However, upon diode testing, it was revealed that there were large resistances in series with the diodes across the entire wafer. After a 450°C anneal, the resistance was greatly reduced. As this is the temperature at which hydrogen outgasses from InP, it was believed that the hydrogen from the etch were diffusing through the hard mask into the semiconductor due to the DC bias used to generate the etch plasma. To investigate this issue, an alternative waveguide etch was developed devoid of hydrogen to determine whether the series resistance could be improved in future device runs.

The new waveguide etch chemistry was largely based on an existing etch developed in [74] for the Unaxis ICP tool in the UCSB cleanroom. This etch consisted of a combination of chlorine, hydrogen, and argon gas plasma ignited in an ICP etching tool under a pressure of 1.4 mTorr; in the work here, the hydrogen gas was replaced with nitrogen. The chlorine gas does the majority of chemical etching, creating the precipitates listed in Table 5.3. As seen from the table, the etch precipitates have a high boiling point, requiring a high temperature to facilitate removal. The wafer was heated to 200°C using a backside thermal loop in the etcher to allow proper removal of the etch products. Similar to hydrogen, the nitrogen in the chemistry passivates the sidewall of the waveguide as the etch progresses, which reduces ion interaction with the sidewall, increasing verticality. The argon serves as a physical component of the etch. The combination of nitrogen sidewall passivation and argon physical etching results in a polishing effect which smooths the sidewall out, reducing roughness.

Table 5.3. Boiling point of chlorine etch precipitates at atmospheric pressure [75].

Etch Product	Boiling Point at 1 atm
$AsCl_3$	130°C
PCl_3	76°C
PCl_5	162°C
$InCl_3$	600°C
$GaCl_3$	201°C

Several iterations of the waveguide process were required before the waveguides had sufficiently low roughness for low propagation loss; Figure 5.6 presents SEM images of several iterations. The image on the left shows the first attempt at the waveguide etch. From the image, it is clear that significant surface roughness is present, indicating insufficient substrate temperature for etch precipitate removal. This problem arose due to the nature of the wafer size required by the ICP etch tool. The ICP etch tool is designed to etch 4 inch wafers; as the process runs in this work were completed using one quarter of 2 inch wafers, a carrier wafer was required for compatibility. In this case, the sample was simply placed on the carrier wafer and run in the tool; under vacuum, the wafer heating used to control the substrate temperature was unable to transfer the heat to the quarter piece, resulting in insufficient heating and significant surface precipitation causing micro-masking and grassing of the etch surface. To resolve this issue, the quarter piece was thermally connected to the carrier wafer using conductive grease, after which the surface roughness was greatly improved.

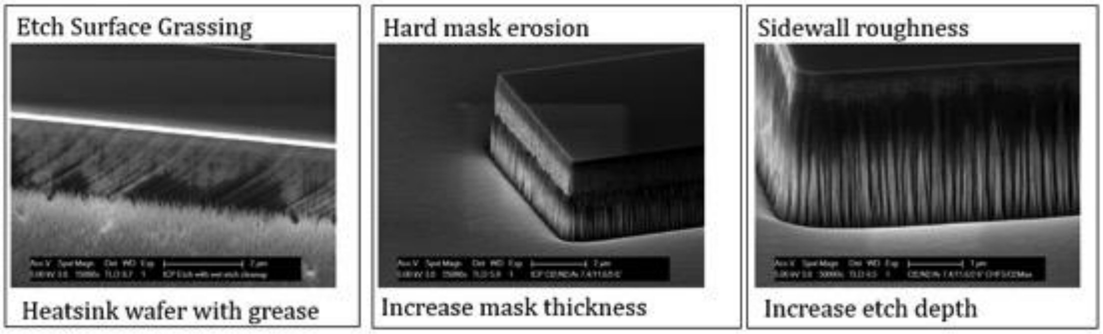

Figure 5.6. SEM images of several iterations of waveguide etch development. The image on the left depicts significant surface roughness from inadequate substrate heating, the center image depicts increase sidewall roughness due to mask erosion, and the right image shows sidewall roughness from shorter etch times.

Once the surface roughness had been improved, the next issue uncovered was an etch shelf that was formed from hard mask deterioration, as the new etch chemistry had a much lower selectivity than that previously used (5:1 versus 30:1). By increasing the SiO_2 mask thickness to 700 nm, this issue was eliminated. Finally, it was found that the sidewall roughness of the waveguide was much greater than that of the old etch after etching a similar depth. For the rib waveguide, which uses a wet etch to clean up any unfinished etching, this was not an issue, as the wet etch smooths out the roughness, as shown in the final waveguide etch shown on the right in Figure 5.7. With the strip waveguide geometry, a wet etch step is not possible, and the roughness remains, as shown in the rightmost image of Figure 5.6. The root-mean squared (RMS) line edge roughness of the sidewall measured with an AFM tool was 45-55 nm, resulting in propagation losses of 8-10 dB/mm through a 1.8 μm wide deeply etched waveguide. It was observed, however, that the roughness was much less at the top of the waveguide than the bottom, indicating that increased etch time may lead to reduced roughness. Based on this observation, the etch depth was increased 3 μm past the waveguide layer to polish the sidewall resulting in an RMS line edge roughness of 15 nm at the waveguide layer and propagation losses below 5 dB/mm for a 1.8 μm wide deeply etched waveguide.

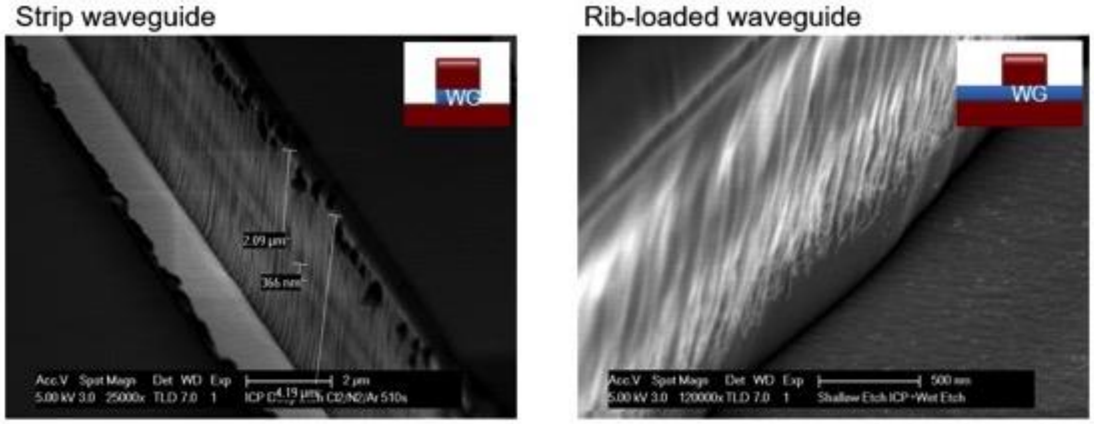

Figure 5.7. SEM image of the final waveguides after processing. The image on the left is a deeply etched strip waveguide, and the image on the right is a shallow etched rib-loaded waveguide. Inserts at the top-right of each image show the structure of each waveguide.

Another observation made during etch characterization was that the roughness initiated from roughness in the hard mask, as shown in the left image in Figure 5.8. Modern stepper tools specify a line edge roughness of 5% of the smallest feature size, meaning that an i-line stepper with a 400 nm minimum feature will have a line edge roughness of 20 nm, similar to the best roughness achieved for the deeply etched waveguides. By switching to a lithography tool with lower wavelength source such as a krypton fluoride laser with a 248 nm wavelength or an argon fluoride laser with a 193 nm wavelength, this roughness could be potentially reduced even further.

One additional cause of the roughness could be from resist deformation during the hard mask etch; this was investigated by taking an SEM image of the developed photoresist before etching, as shown in the right image in Figure 5.8. From this image, the photoresist appears quite smooth, indicating that significant roughness must be added during the hard mask etch, potentially due photoresist degradation under plasma. This effect could be mitigated by decreasing the RF power applied to the plasma or using short bursts of etching to avoid burning the resist.

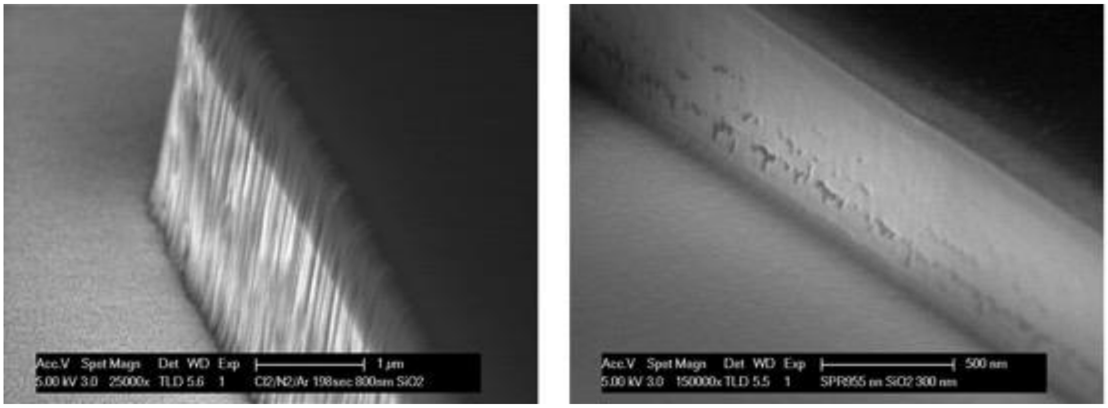

Figure 5.8. SEM images of the masking profiles at two different points in the waveguide process. The image on the left shows the waveguide with its 700 nm SiO_2 mask just after the chlorine dry etch showing a clear correlation between the roughness of the hard mask and the indium phosphide. The image on the right shows the resist prior to the hard mask etch.

5.3.5 Dielectrics

After the waveguides were etched, the surface of the wafer was encapsulated in a dielectric material used to electrically isolate the surface of the device from large metal pads that will be deposited on the surface of the device for electrical probing; deposition of the metal layers without the dielectric would result in electrical contact across the wafer, shorting out the device. A 300-350 nm layer of silicon nitride was deposited by PECVD; this material was chosen for its relatively film high quality and absence of pin-hole defects which can be found other PECVD-deposited materials such as SiO_2. The pin holes could result in short circuit paths to the waveguide layer of the device, which could potentially lead to poor device performance.

One issue with the PECVD deposition process for silicon nitride is the possibility for hydrogen contamination. The gas chemistry used to form the Si_3N_4 contains SiH_x as a precursor that forms hydrogen as a byproduct. At the 250° C deposition temperature, these hydrogen ions could potentially be driven into the surface of the semiconductor, increasing the resistance of the device. Rather than PECVD deposit the dielectric, a sputtering process could be used instead, which is physical deposition process using particle bombardment to knock atoms from a dielectric target and redeposit them onto the desired surface. As this process is purely physical, it involves no hydrogen byproducts which could potentially passivate the device; however, the resulting deposition rate is much slower than PECVD. For example, a 100 nm Si_3N_4 layer would require 1 hour to deposit using sputtering compared to 8 minutes using PECVD deposition. As such, commercial production of integrated devices would most likely use the PECVD option, and the hydrogen contamination can be mitigated by depositing the metal contact layer prior to the dielectric to serve as a hard mask for the active areas of the device.

The thin film of Si_3N_4 was sufficient for current isolation of DC electrical pads, but in areas where high speed is desired, the pads form a large capacitor with the wafer surface that increase the switching time of high speed modulators and photodiodes. To reduce this pad capacitance, a thicker dielectric layer with a lower dielectric constant was deposited under the pads for the RF devices. For the all-optical switch, the modulators used a 2.4 μm thick layer of SiO_2 as the dielectric, but it was found during testing that the pad capacitance was still dominating the frequency response of the device. Thus for the photodiodes of the coherent receiver, the dielectric was switched to BCB and its thickness was increased to 7.5 μm, resulting in greatly improved performance of the photodiodes that were now transit-time limited through the intrinsic region of the photodiode.

The BCB used was a photosensitive resin that has much less tolerance to inadequate surface preparation and can result in poor adhesion, making it impossible to wire bond the metal pads without ripping them off the device. To avoid this issue, the surface was prepared by depositing half of the Si_3N_4 layer prior to spinning on the resist. The sample was then exposed to a high-temperature O_2 plasma to thoroughly clean and dehydrate it and treated with AP 3000, an adhesion promoter designed to specifically improve the adhesion of BCB. The adhesion promoter was left on the surface for 1 minute to allow it to react with the surface and then spun off, and the wafer was then dried off on a hot plate for 1 minute. The BCB was spun on at 1500 RPM using a standard resist spinner; this was the lowest speed possible without forming a large bead of photoresist at the edges of the wafer that might cause an out-of-focus exposure on those surfaces and loss of the outer devices. The devices were then exposed, soft baked at 95°C for 1 minute, spin-developed once, and then cured in an oven at 250°C for 4 hours. Finally, the top 500 nm of BCB was etched away using an 80/20 O_2/CF_4 ICP etch in order to remove a scum layer present from the curing process which can affect the adhesion of the metal layers to the BCB, and the second half of the Si_3N_4 was deposited on top to encapsulate the BCB.

5.3.6 Vias, Metallization, and Electrical Isolation

Once the dielectric layers had been deposited, vias were etched through to expose the metal contacts in areas for current injection using a CF_4/O_2 ICP etch. A direct via process was used in which the vias are exactly defined in the photoresist and etched all the way through. As the stepper's alignment is limited to within 150 nm, the vias were designed to be 200 nm narrower on each side than the full width of the waveguides in order to mitigate short circuiting from alignment errors. Since Si_3N_4 dielectric layer was sufficiently thin, sloping in of the vias due to etching was not an issue. However, because the BCB dielectric layer was so thick, the angle of the sidewall after etching was a concern, as too narrow of a via opening lithographically defined at the top of the BCB could end up fully closed by the time the etch reaches the bottom. The etch chemistry used to remove the BCB layer was an 80/20 ratio of O_2/CF_4 in an ICP etch tool, as the BCB is comprised primarily of polymer. To avoid the closing of the via at the bottom, the mask was designed to be 2 μm wider. An SEM image of the via opening with metal deposited all the way to the bottom is shown in Figure 5.9 showing that the via width was sufficiently wide enough to open up at the bottom.

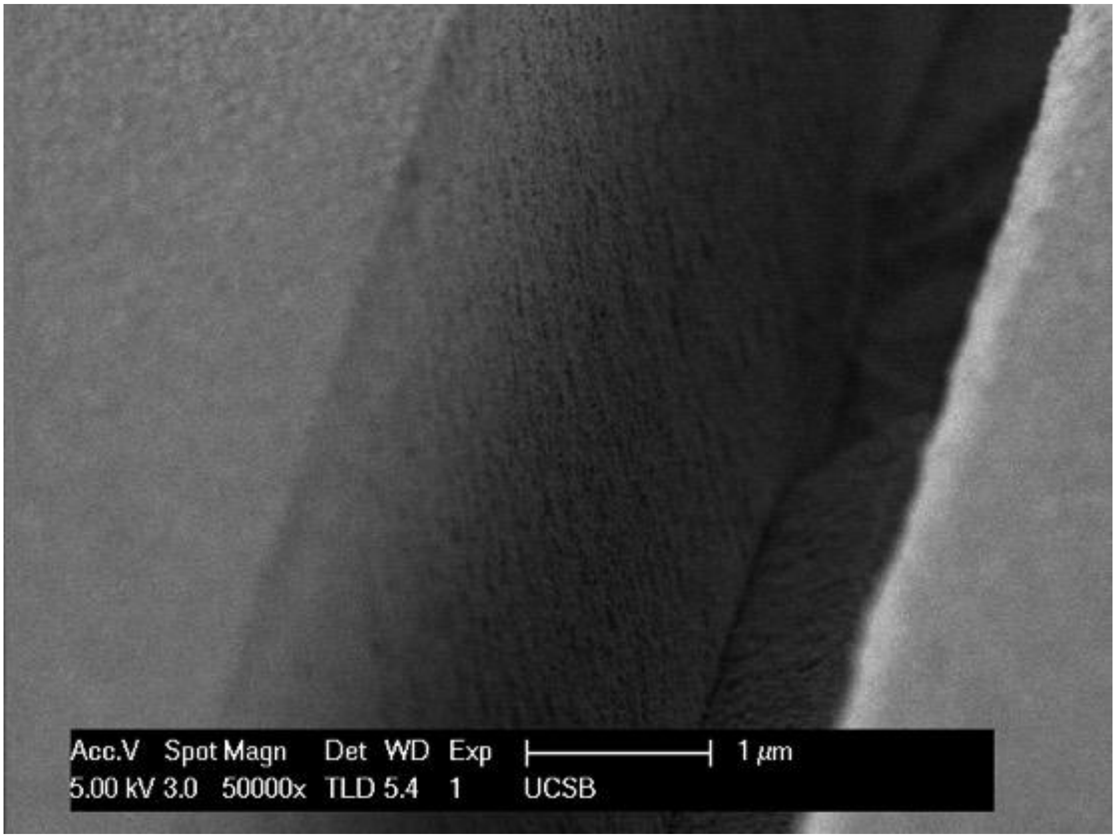

Figure 5.9. SEM image of via etched into BCB showing full gold coverage and no shadow effects down to semiconductor surface.

Once the vias were opened, a metal stack consisting of 20 nm titanium, 40 nm of platinum, and 1 μm of gold was deposited using electron beam deposition to connect to the diodes and form large pads which can be wire bonded and probed. To fill in the vias and ensure sidewall coverage of the waveguide structures, a planetary rotation system was used to rotate the device around while depositing. The metal layer started with titanium to facilitate adhesion of the contacts to the dielectric surface. After this, a platinum layer was deposited to overcome the Schottky barrier height formed from the difference between the band gap of the InGaAs contact layer and the metal work function and to serve as a diffusion barrier during annealing. The platinum has a higher work function than gold, reducing the Schottky barrier height and forming a better ohmic contact at the metal-semiconductor junction.

To minimize hydrogen contamination of the semiconductor, a metal contact layer was deposited prior to any other post-regrowth processing and layer connected through the vias to the main electrical pads. Prior to deposition, the sample was etched with a 1:3 mixture of $HCl:H_2O$ to remove any native oxide on the semiconductor and replace it with temporary Cl^- terminations to prevent immediate oxide reformation [76]. The sample was then blow dried with nitrogen and immediately placed into vacuum for deposition. The order of deposition and layer thicknesses for the contact layer are shown in Table 5.4. For the all-optical switch, the deposition started with a titanium layer, but in the coherent receiver, a 10 nm platinum layer was deposited prior to the titanium layer to further reduce the Schottky barrier height [77]. The contacts were then annealed at 300°C to form the metal-semiconductor interface.

Table 5.4. Metal contact layers from top to bottom based results from [77].

Layer	Thickness
Gold	10 nm
Platinum	30 nm
Gold	100 nm
Platinum	40 nm
Titanium	20 nm
Platinum	10 nm
p-InGaAs	100 nm

As the top InGaAs layer is highly conductive due to a high doping concentration, the vias were extended 5 µm beyond the end of the metal on the top of the diodes and etched in 3:1:50 H_3PO_4:H_2O_2:H_2O to selectively remove the InGaAs, stopping on the indium phosphide. A 100 keV hydrogen implant at 200°C was then performed to further isolate devices from each other; the implanted hydrogen ions bind with the zinc dopant, deactivating it and increasing the resistance of the p-doped semiconductor. The implant also has the added benefit of decreasing the loss of the passive waveguide sections, as the zinc dopant is the primary cause of the inter valence band absorption. Once implanted, the passive waveguide loss in a rib-loaded waveguide was reduced from 1.3 dB/mm to 0.8 dB/mm.

5.3.7 Packaging

Once the metallization was complete, the wafer substrate was thinned to 100-150 μm to facilitate cleaving, and a metal stack consisting of 20 nm of titanium, 40 nm of platinum, and 1 μm of gold was deposited on the backside to form a common ground. The devices were then cleaved with a precision cleaver and soldered to a gold-plated aluminum nitride carrier for improved heat dissipation. On the coherent receiver, the photodiodes were wire bonded to coplanar waveguide transmission lines on the carrier to facilitate high speed probe contact; these wire bonds were made as short as possible to get as close to the optimal inductance as possible. No wire bonding was performed on the all-optical switch; instead it was electrically probed using tungsten probe tips. Lensed fibers with 2 μm spot sizes were used to couple in and out of the on-chip waveguides and were aligned to the waveguides using grooved fiber boats controlled by a precision 3-axis stage with piezoelectric tuning.

Chapter 6

Coherent Receiver Component Characterization

As the receiver relies on many different optical elements to achieve full functionality, it was imperative to verify the performance of the individual components before testing the full device. On a single coherent receiver, there are over 12 discrete optical functions integrated including local oscillator, splitter, 90° optical hybrid, and photodiodes that must all work properly for full device operation. On the all-optical switch, each of the 16 wavelength converter channels integrates 5 discrete optical functions per channel including laser pump source, delay line, booster SOAs, and optical-optical MZI for a total of 81 optical functions on-chip including the AWGR router. Each optical function must be tested to determine its performance and the potential capability of the entire device prior to system testing to specify the full performance and identify any fabrication issues.

6.1 Receiver Components

To meet the performance specifications of the coherent receiver, two components in particular were developed prior to their implementation in the full receiver PIC. These components were the photodiodes critical for the high speed operation of the receiver and the polarization rotator required for on-chip polarization demultiplexing. In addition, the photodiodes had to interface with a commercial digital oscilloscope, so the on-carrier transmission lines as well as wire bonds used to interface between them had to be verified prior to their application with the receiver. Finally, since significant development work was performed on a new waveguide etch, it was also necessary to thoroughly characterize the performance of the passive components of the chip to understand their effect on the loss budget of the device. Thus the characterization of these components will be detailed before going into the results of the receiver characterization.

6.1.1 Photodiodes

The photodiodes were characterized using an on-chip test structure consisting of a tapered waveguide and photodiode. The waveguides of the test structure photodiodes were 3 μm wide as opposed to the 3.65 μm width on the on the receiver. First the responsivity of a 30 μm long photodiode was measured from 1500 to 1600 nm. The photodiode was reverse biased at -3 volts, producing a dark current of less than 100 nA. An external cavity laser was TE-polarized in a polarization controller to maximize absorption in the quantum wells and coupled to the chip using a 2 µm spot size lensed fiber, and the resulting photocurrent generated was measured with a Keithley voltage source. Maximum responsivity of 0.3 A/W at 1515 nm and a 3 dB bandwidth of 74 nm occurred from 1474 to 1548 nm. This absorption range results from a combination of absorption due to both the quantum wells designed with a 1545 nm bandgap and the absorption of the red-shifted 1.4 µm waveguide layer to the Franz-Keldysh effect from the large electric field across the photodiode.

To find the optimal photodiode length, the responsivity of several different photodiode lengths from ranging from 7.5 µm to 60 µm were measured and plotted in Figure 6.1. All photodiodes were biased at -3 V, and the input wavelength was set to 1550 nm. A maximum responsivity of 0.4 A/W was measured at a photodiode length of 50 µm; beyond this length, no further increase in responsivity was observed. To determine the coupling loss of the device, a Fabry-Perot cavity consisting of an identical waveguide structure and input/output facets was swept from 1500-1600 nm, and the output power was coupled out of the other facet and measured in a power sensor. The length of the cavity was varied by cleaving back the sample to de-couple the waveguide loss from the mirror loss; the waveguide loss was measured as approximately 1.3

dB/mm, and the resulting coupling loss was 5 dB per facet. This matched closely with the measured responsivity of the photodetectors that have an ideal responsivity of 1.24 A/W without coupling loss.

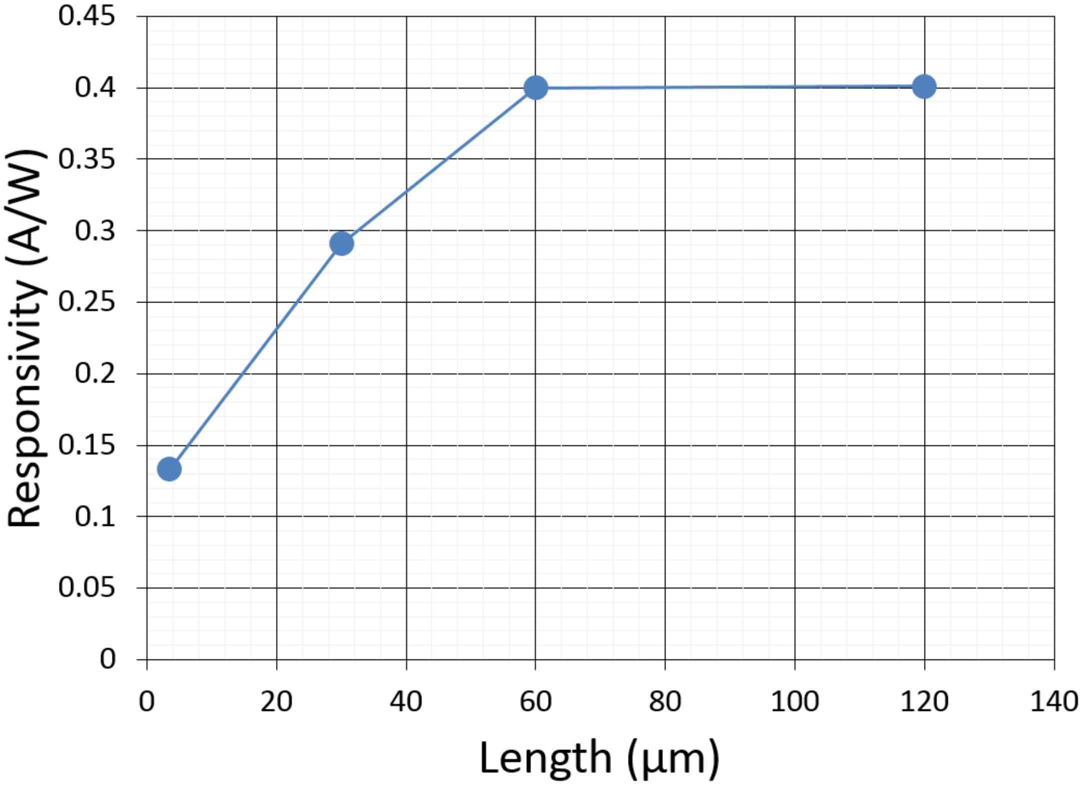

Figure 6.1. Responsivity of photodiodes with length varying from 7.5 to 60 µm. Measurement performed with a TE-polarized 0 dBm output at 1550 nm coupled from an external cavity laser to the photodiode with a 2 µm lensed SMF fiber. 20-100 nA leakage currents were measured at the photodiodes with a -3 V bias. Photodiode was temperature controlled to 15°C.

Next three 30 µm photodiodes were bonded to similar transmission lines with wire bond lengths of 200, 500, and 600 µm to find the optimal inductance. The photodiodes were then measured with a Keysight N6343B Lightwave Component

Analyzer (LCA) to determine their RF response. To interface with the LCA, transmission lines were probed with a ground-signal-ground probe. The electrical connections from the LCA down to the GSG probe were calibrated out of the measurement by measuring their open, short, and load circuit response using a calibration substrate. After calibration, a modulated optical signal was swept from 100 MHz up to 40 GHz and coupled to each photodiode while reverse biased at -1.5 V, and the small-signal current was measured by the LCA; the resulting S21 frequency response of the photodiodes are shown in Figure 6.2, exhibiting a 3 dB optical roll-off of greater than 30 GHz for the shortest wire bond length. Several dips in the response at low frequencies occur due to resonances in the transmission line, but more significant ringing occurs at frequencies above 28 GHz. These resonances occur due to the non-terminated nature of the photodiode, which has a large impedance under reverse bias. At high frequencies, this impedance appears as an open circuit at the end of the transmission line resulting in increased reflections. As expected, the longer wire bond lengths had more limited bandwidth due to additional parasitic inductance limiting their bandwidth to below 22 GHz.

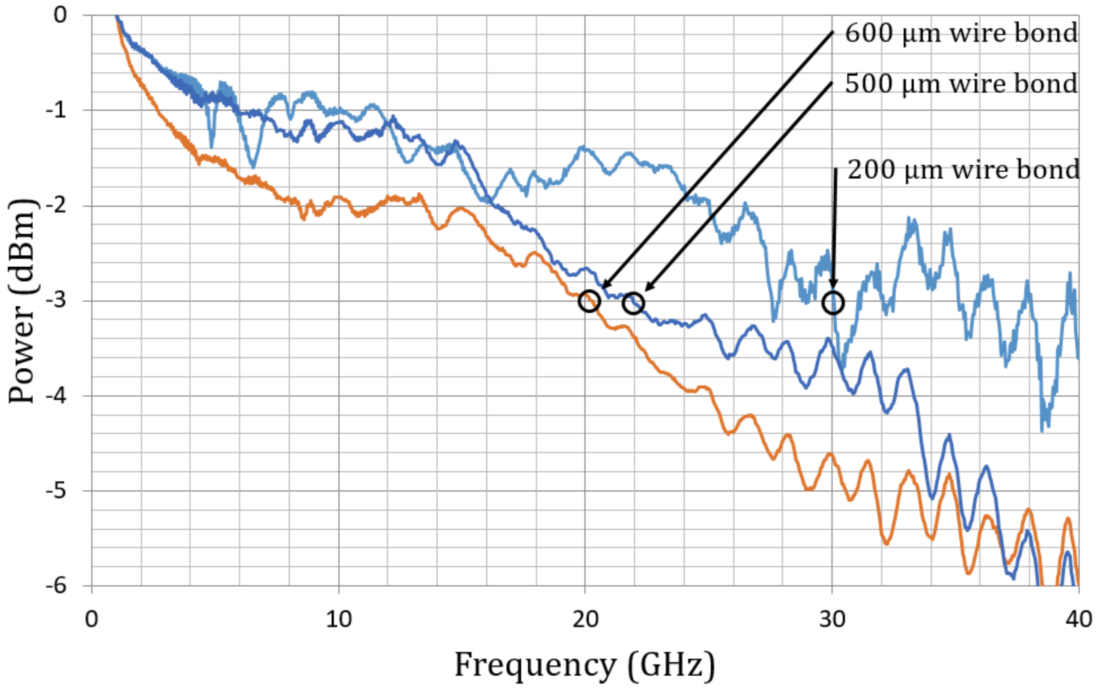

Figure 6.2. Frequency response of three 30x3.65 μm photodiodes including wire bond and transmission line normalized to 1 GHz. Only wire bond lengths were varied from 200 to 600 μm, significantly affecting the bandwidth of the photodetector circuit. Measurement performed with a TE-polarized 6 dBm output at 1550 nm coupled from a Keysight N6343B LCA to the photodiodes with a 2 μm lensed SMF fiber. 20 nA leakage and 1.1 mA photocurrent were measured with a -1.5 V bias. Photodiodes were temperature controlled to 15°C.

To determine whether parasitic capacitance from carrier trapping was limiting the performance of the quantum well photodiodes, another photodiode was fabricated without the quantum well layer and again measured in the LCA; the resulting S21 frequency response is plotted in Figure 6.3, showing similar performance. As the intrinsic region of the diode was removed, this diode required a much larger reverse bias of -5 V to reach the optimal depletion width of the diode to achieve a similar diode resistance and capacitance. This diode exhibited similar ringing to the quantum well design due to its non-terminated nature.

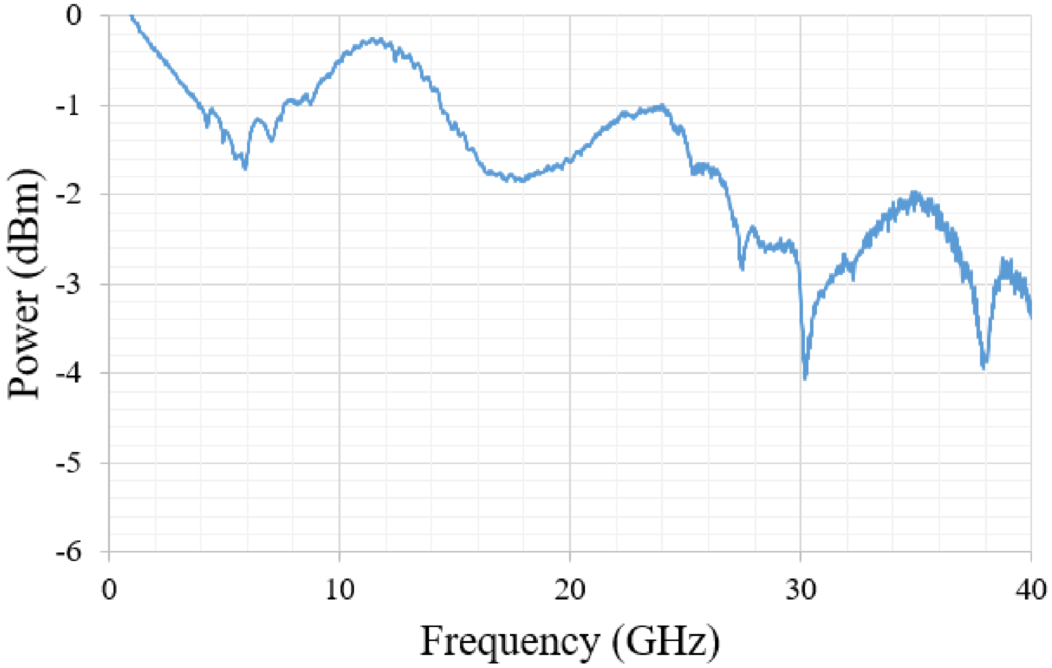

Figure 6.3. Frequency response of a 30x3.65 µm photodiode with absorbing quantum well layer removed. Measurement performed with a TE-polarized 6 dBm output at 1550 nm coupled from a Keysight N6343B LCA to the photodiode with a 2 µm lensed SMF fiber. 20 nA leakage and 1.1 mA photocurrent were measured at the photodiode with a -1.5 V bias. Photodiode was temperature controlled to 15°C.

Next an amplitude-shift keyed non-return-to-zero pseudo-random bit sequence (NRZ-PRBS) with a 2^7-1 bit length was generated with an commercial optical intensity modulator and input into the photodiode, and the resulting signal was captured on a digital storage oscilloscope, as shown in Figure 6.4. Test setup for this measurement is shown in Figure 6.5. The detected signal had an open eye and showed no distortion, indicating suitable performance for the receiver.

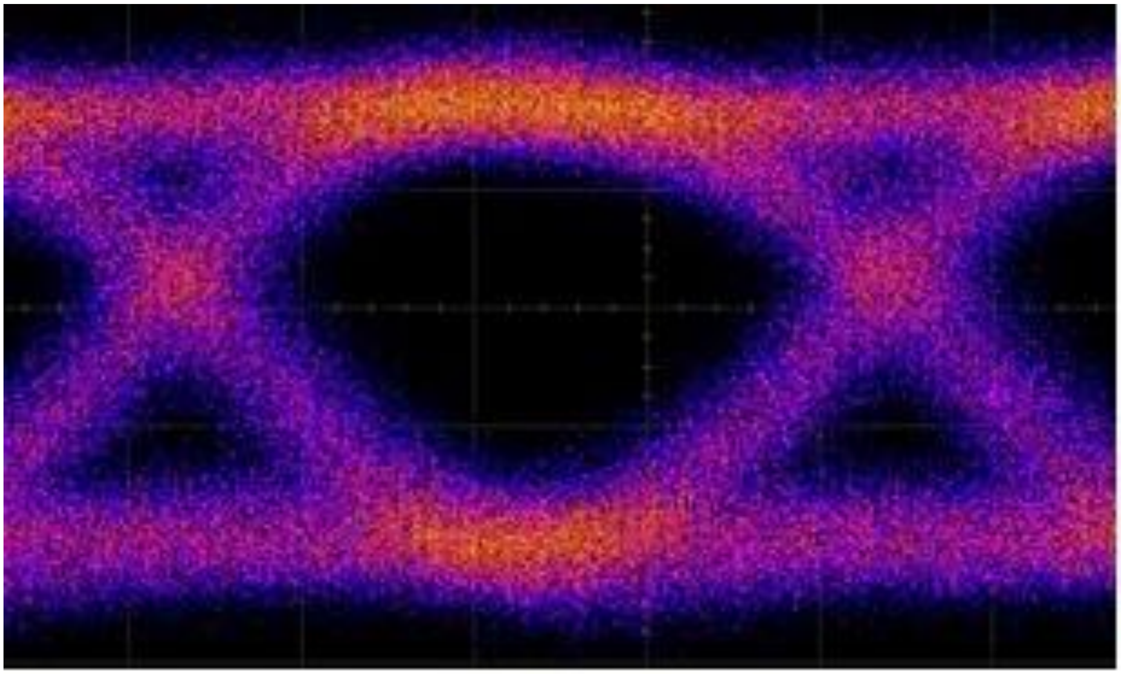

Figure 6.4. Output of a 25 GHz ASK NRZ-PRBS 2^7-1 optical signal detected by an on-receiver photodiode. Signal was generated from an external cavity laser output modulated by a lithium-niobate MZ modulator and amplified by an EDFA at 1550 nm coupled to the photodiode with a 2 μm lensed fiber. 1 μA leakage and 300 μA photocurrent were measured at the photodiode biased at -1.5 V. Photodiode was temperature controlled to 15°C. Measured with test setup presented in Figure 6.5. Reprinted with permission from [78].

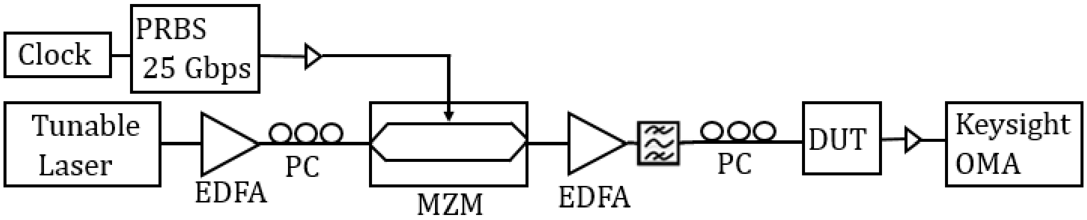

Figure 6.5. Test setup used to measure amplitude-shift keyed NRZ-PRBS 2^7-1 data stream at 25 GHz in one of the receiver photodiodes.

6.1.2 Polarization Rotators

To determine whether integrated polarization demultiplexing would be feasible on the coherent receiver, a set of polarization rotators were fabricated using a slanted sidewall geometry with an array of widths from 550 to 850 nm in 50 nm increments and lengths ranging from 70 to 170 μm in 5 μm steps. An image of the setup used for characterization is presented in Figure 6.6. An external cavity laser output was TM polarized in a polarization controller and couple to the test waveguide with a lensed fiber. After propagating through the waveguide, the output light was focused onto a polarization beam splitter through a microscope objective and split into TE and TM components. Each component was measured by a power sensor to determine any polarization rotation produced by the waveguide.

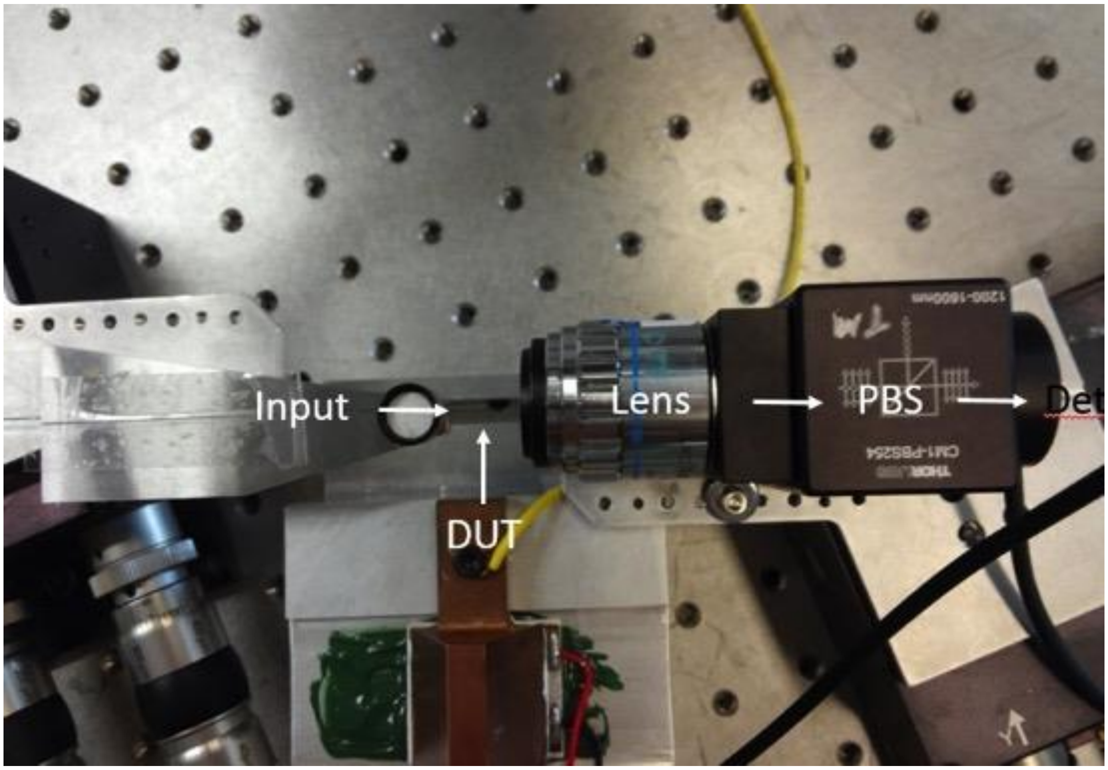

Figure 6.6. Test setup for measuring the polarization rotator. Rotator measured using a 14 dBm TM-polarized output at 1550 nm from an external cavity laser amplified by an EDFA coupled into the device using 2 μm lensed fiber and collected using a microscope objective attached to a polarization beam splitter. Power was measured from each PBS output with a photodetector. Rotator was temperature controlled to 15°C.

Testing revealed that the 800 nm waveguide produced polarization rotation, confirming simulations showing a tight width tolerance for the rotator design. The resulting TE and TM output power fractions are plotted for varying lengths in Figure 6.7, revealing a rotation of 12.6° per 100 μm. The insertion loss of the rotator was also determined by summing together the two output components and plotting the total output power over the varying lengths, as shown in Figure 6.8. The resulting propagation loss was 3 dB per 100 μm.

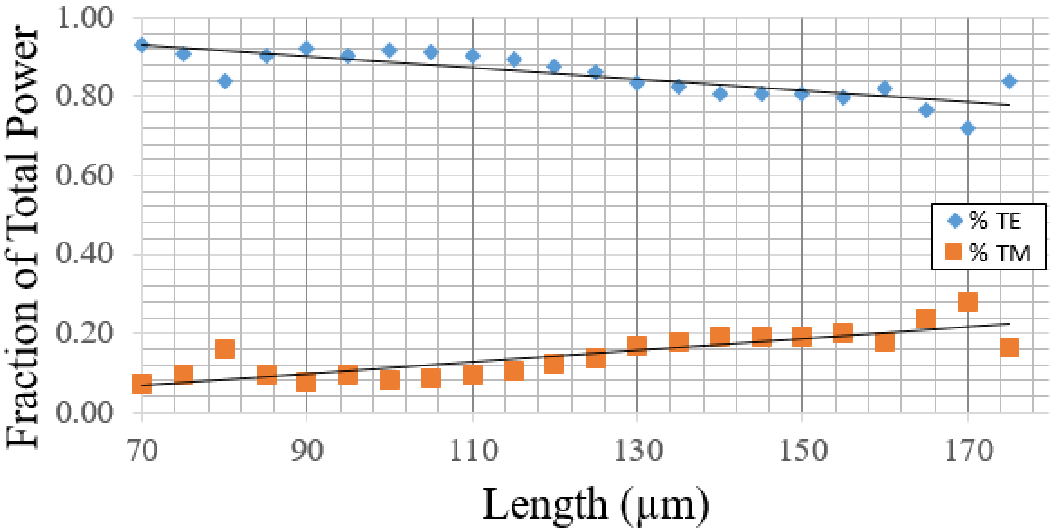

Figure 6.7. Fraction of TE and TM light produced from an array of polarization rotating waveguides with varying lengths. Rotator width was 800 nm. Test setup used to perform measurement is presented in Figure 6.6.

To produce a 90° polarization rotation with this waveguide design, the rotator would need to be 715 μm long, resulting in over 21 dB of insertion loss for this particular design. This amount of insertion loss was deemed too high for use in the receiver, so an off-chip polarization demultiplexing scheme was chosen as the most viable option. The high loss through the waveguide may be attributed to increased mode interaction with the sidewall roughness resulting in increased scattering loss. The narrow waveguide width of 800 nm required for the mode to strongly interact with the waveguide's asymmetrical design also caused the mode to interact much more strongly with the roughness of the sidewall. To date, all polarization rotation schemes on indium phosphide have been based on birefringence produced from strong interaction with a waveguide asymmetry; as this inherently relies on high mode confinement in the waveguide to produce the necessary interaction, feasible integration of a polarization rotator based on these design approaches requires greatly reduced waveguide roughness to minimize scattering loss for the tight mode confinement required.

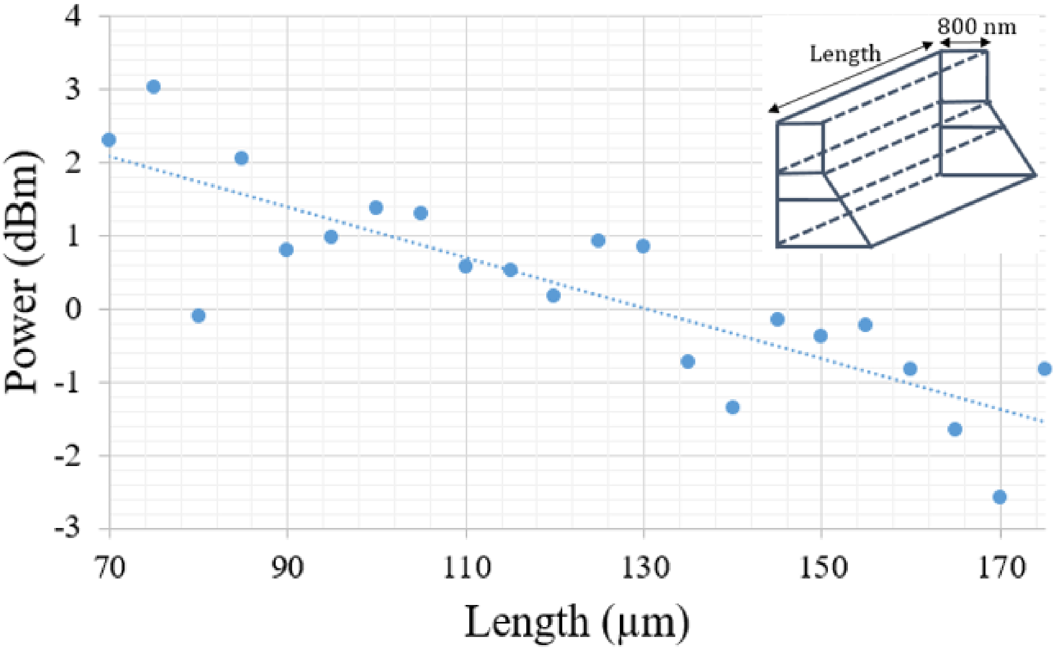

Figure 6.8. Total output power collected from various rotator lengths for an 800 nm device width with inset of rotator design. Input signal was a TM-polarized CW signal from an external cavity laser source at 1550 nm amplified to 14 dBm with an EDFA. Test setup used to perform measurement presented in Figure 6.6. Loss includes 5 dB coupling loss into and out of device for 10 dB total coupling loss beyond intrinsic rotator loss.

6.1.3 Waveguides

As the coherent receiver chip was the first device utilizing a newly developed chlorine/nitrogen/argon waveguide etch, extra effort was spent verifying the waveguides had propagation loss less than 1.5 dB/mm to meet the 3.5 dBm sensitivity design goal for the receiver.

To characterize the propagation loss, a set of test structures was fabricated with various passive components, as shown in Figure 6.9. An array of SG-DBR lasers were used to generate an on-chip optical signal propagated down individual waveguides containing arrays of passive elements separated by 100 µm passive sections electrically contacted with 100 µm long pads for a 200 µm pitch similar to that in [70]. The propagation loss through individual components was then measured and averaged to give an expected loss.

An additional set of passive structures were arrayed into Fabry-Perot cavities and measured using the cut-back method described in [79]; the measured loss of each passive component is presented in Table 6.1.

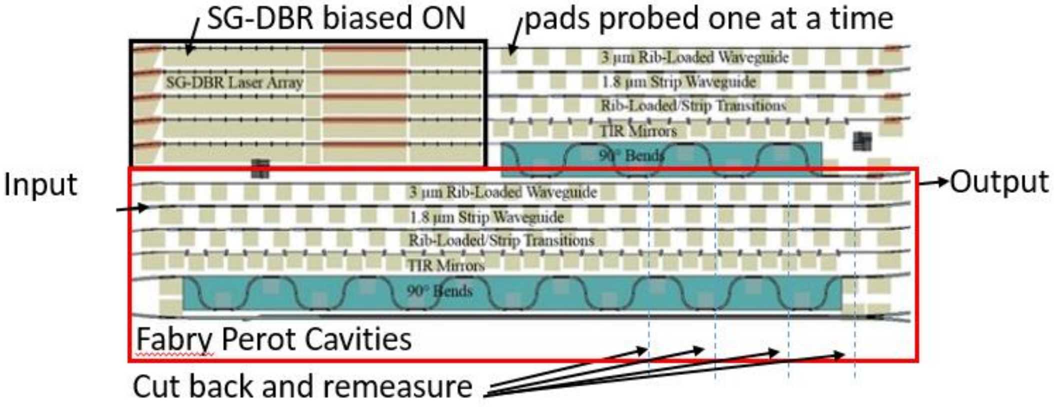

Figure 6.9. Layout of test structures for waveguide testing.

Of particular importance for optical integration is the ability route a signal 90° allowing for more compact circuit design enabling more effective use of chip area. Two different schemes for 90° bends were investigated: TIR mirrors, which consist of a deeply etched concave reflector connecting two perpendicular rib-loaded waveguides, and 90° bends with a 100 µm radius. The TIR mirrors were based on a design from [80] and allow for all routing to be completed using rib-loaded waveguides, eliminating the need for waveguide transitions. On the other hand, the 90° bends require deeply etched strip waveguides to keep the mode confined through the small turn radius desired. This also necessitates adiabatic tapering to and from the different waveguide structures for minimal loss. The passive structures measured included 3 µm wide rib-loaded waveguides, 1.8 µm strip waveguides, adiabatic tapers to and from the rib-loaded and strip waveguides, deeply etched TIR mirrors connected by 3 µm rib-loaded waveguides, and strip waveguide 90° bends; the results of the measurements are listed in Table 6.1. To reduce turnaround and speed up development time, no implant was performed on the waveguide test structures.

Table 6.1. Results from passive structure loss measurements using on-chip laser sources and waveguide power monitor arrays.

Element	Loss
3 μm rib-loaded waveguide	1.27 dB/mm
1.8 μm strip waveguide	5.14 dB/mm
3 μm strip waveguide	1.5 dB/mm
Rib/strip taper	2 dB/mm
Strip/rib taper	1 dB/mm
TIR Mirror	1.2 dB/mm
90° bends (per 90°)	2.4 dB/mm

The propagation loss in a straight 3 μm wide rib-loaded waveguide was 1.3 dB/mm, similar to that demonstrated in [72]. The propagation loss of the 1.8 μm strip waveguide was 5.1 dB/mm, and the 90° strip waveguide bends had an additional 2.4 dB of loss per 90° due to larger mode interaction with the sidewall roughness resulting in increased scattering. Adiabatic transitions to and from the different waveguide structures hadlosses of 2 dB and 1 dB for the rib-to-strip and strip-to-rib respectively. As the receiver utilized deeply etched 180° bends to route the LO signal to the hybrids, these losses contributed to 8 dB excess path loss from the LO's output. In comparison, the TIR mirrors had a loss of only 1.3 dB per mirror and would have resulted in 2.6 dB for the same 180° bend. Despite this result, the 90° bends were ultimately used on the receiver as there was not enough time to update the receiver mask before fabrication of the full device occurred. However, the increased loss had the unintended benefit of providing on-chip isolation to minimize reflections going back into the SG-DBR laser.

6.1.4 Transmission Lines

As the photodiodes were wire bonded to high speed transmission lines on an aluminum nitride carrier to allow for high speed proving, the transmission line needed to be verified. RF response was measured using a Keysight PNA network analyzer swept from 100 MHz to 50 GHz. The S21 response of the transmission line is presented in Figure 6.10 showing a 3 dB cutoff frequency beyond 50 GHz. Various minor resonance dips were observed due to parasitic inductance paths through the AlN carrier that were largely insignificant to the overall operation of the transmission line and did not affect its 3 dB bandwidth. While minor, these resonances could be reduced by further optimizing the design of the transmission lines.

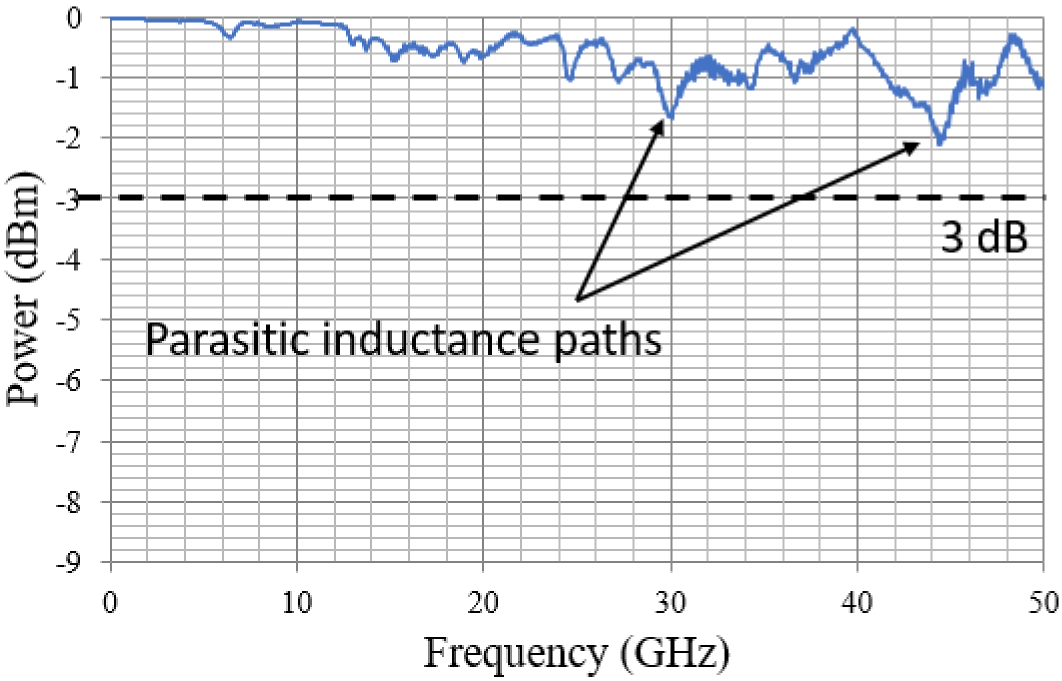

Figure 6.10. S21 measurement of a carrier transmission line used to interface to on-chip photodiodes measured with a 50 GHz Keysight PNA. Various resonance dips were observed due to parasitic inductance paths through the AlN carrier. Measured bandwidth is beyond 50 GHz.

6.1.5 Local Oscillator

The LO for the coherent receiver was characterized to determine its threshold current, differential efficiency, maximum output power, wavelength range, and linewidth. A schematic diagram of the laser is presented in Figure 6.11. First the gain section of the laser was swept from 0 to 100 mA and the output power from the back mirror was measured by reverse biasing the absorber section and measuring the photocurrent. The absorber section was sufficiently long enough for 100% quantum efficiency resulting in a 1.24 A/W responsivity; the measured

L-I curve is shown in Figure 6.12. The threshold current of the laser was 35 mA, and its differential efficiency was 6.3%. The maximum output power was 22 mW at 210 mA out of the front mirror measured using an on-chip test structure.

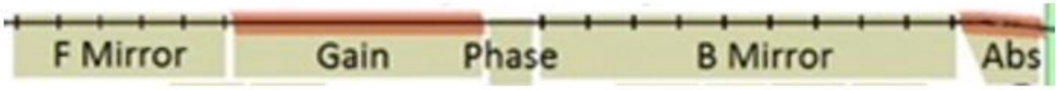

Figure 6.11. Schematic diagram of the SG-DBR laser.

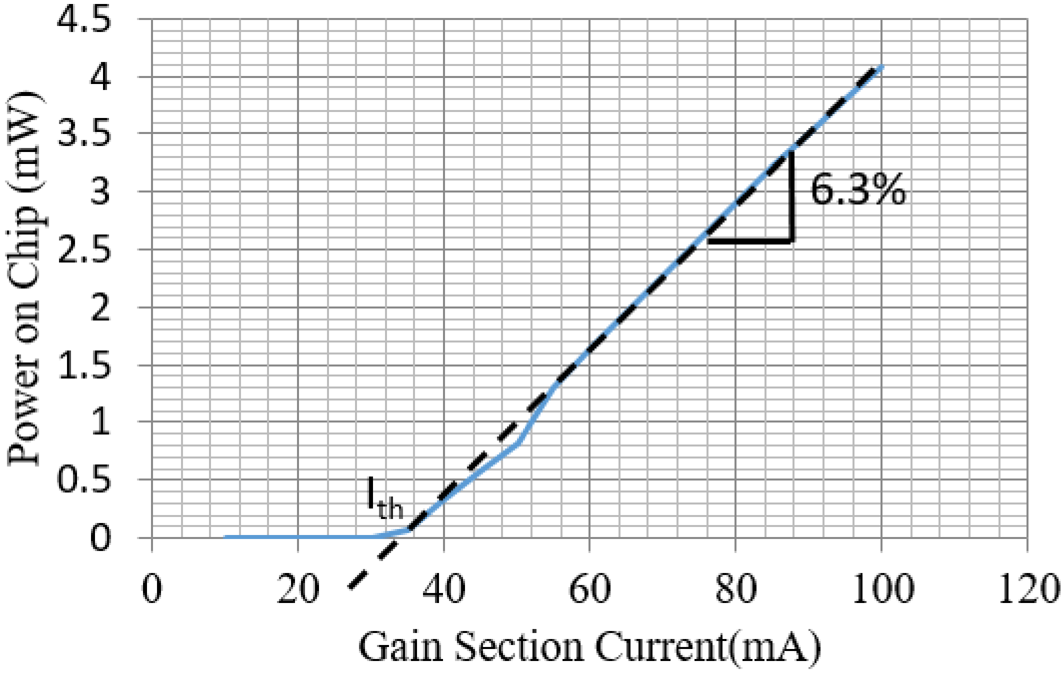

Figure 6.12. LI during CW operation of the SG-DBR laser measured in the reverse-biased absorber. Mirror and phase sections were left unbiased. Laser was temperature controlled to 15°C.

The side mode suppression ratio (SMSR) was measured using an optical spectrum analyzer (OSA) and was greater than 40 dB for all wavelengths, as shown in Figure 6.13. The front and back mirrors were swept in an array from 0-40 mA in 0.5 mA steps to determine the wavelength range of the laser; the resulting wavelength range was 1520 to 1564 nm, sufficient for almost the entire C-band, as seen in Figure 6.14.

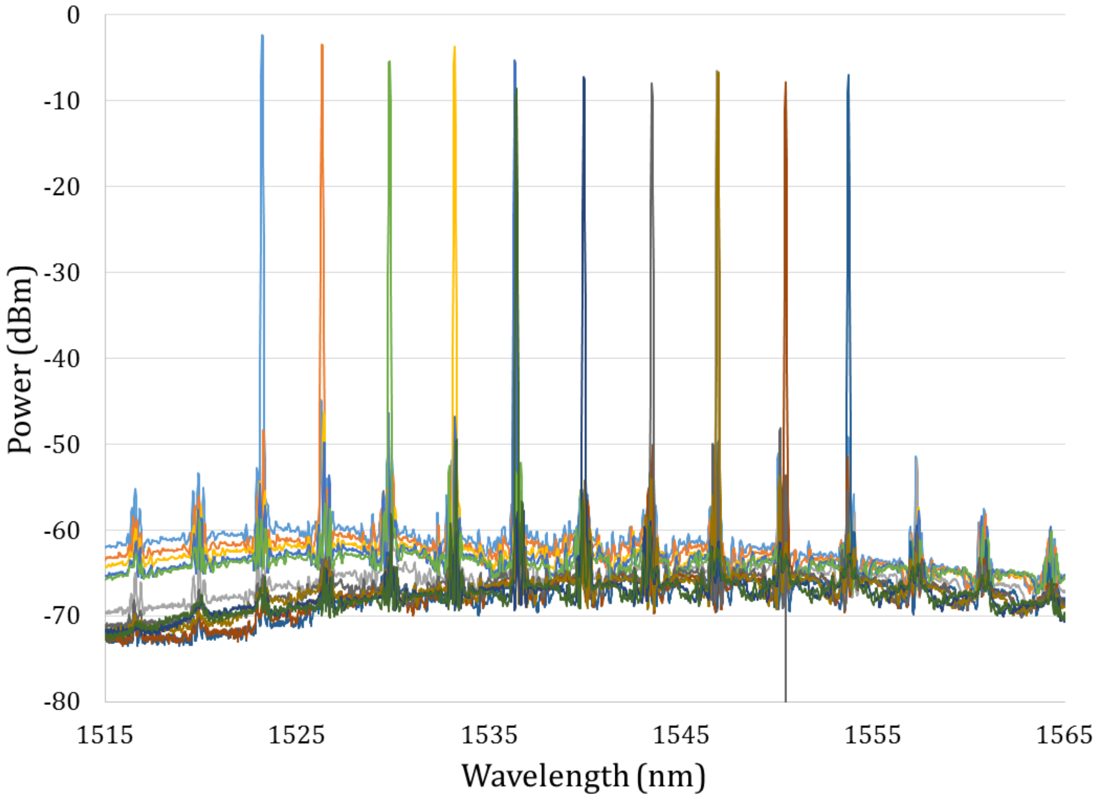

Figure 6.13. Output spectrum of CW operation of the SG-DBR laser at various back mirror biases measured by an optical spectrum analyzer coupled to the laser using a 2 μm lensed fiber. Gain section was biased at 100 mA for all measurements, and laser was temperature controlled to 15°C.

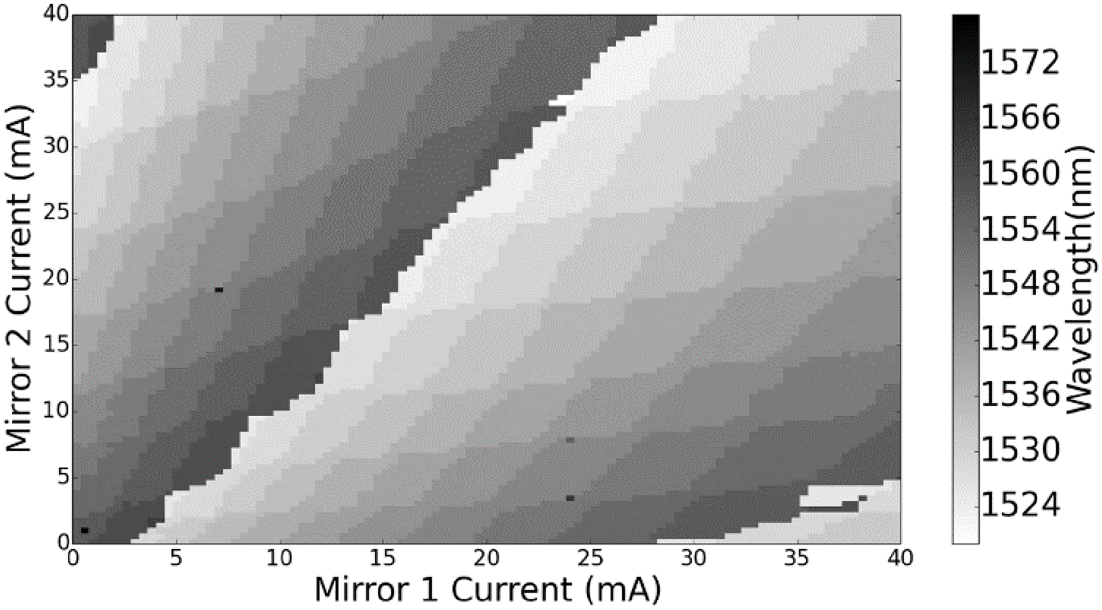

Figure 6.14. Peak wavelength of the SG-DBR laser for various front and back mirror biases measured by an optical spectrum analyzer coupled to the laser using a 2 μm lensed fiber. Gain section was biased at 100 mA for all measurements, and laser was temperature controlled to 15°C. Reprinted with permission from [78].

The linewidth of the LO was measured using the self-heterodyne method at three different wavelengths achieved by tuning the front mirror of the device. A diagram of the test setup used is presented in Figure 6.15. The output of the LO was coupled off chip and then split in a 50/50 fiber coupler. One arm was then delayed with 20 km of LEAF fiber while the other arm was shifted 100 MHz with an acousto-optic modulator. The two beams were then recombined in another 50/50 coupler and converted to an electrical signal by a high speed photodiode. The output of the photodiode was measured in an electrical spectrum analyzer with a 200 kHz resolution bandwidth; the resulting spectrums for the three different wavelengths are shown in Figure 6.16 along with Lorentzian fits used to determine their linewidth. For these linewidth measurements, the front mirror and gain section of the SG-DBR laser were biased using Keithley current sources, and the resulting linewidths were 12, 15, and 18 MHz at 1545.26, 1548.38, and 1551.5 nm, respectively. The increase in linewidth with increasing wavelength was likely due to increased electro-optic absorption from current injection in the mirrors reducing the output power of the laser, as each wavelength required 2-3 mA additional current to shift the mirror index, as well as reduced available gain as the wavelength moves further from the gain peak of the material.

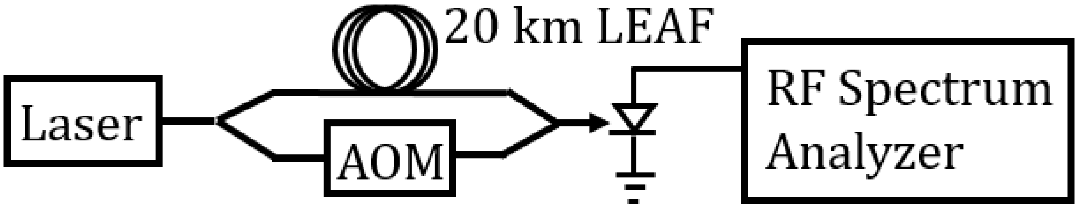

Figure 6.15. Diagram of the self-heterodyne measurement setup used to characterize the LO linewidth.

As the theoretical white noise linewidth of an SG-DBR laser is less than one MHz [81], it was notable that the laser's linewidth was significantly higher than that reported in [82]. In an effort to improve linewidth, the laser was measured again with gain and mirror sections biased with AA batteries similar to that in [60] where noisy current sources had been shown to cause linewidth broadening. The current to the mirror was tuned by connecting a potentiometer in series with its battery source; the output wavelengths were slightly blue shifted as the battery on the gain section was unable to supply as much current as the Keithley source, but the resulting linewidths were now 10, 5, and 8 MHZ at 1544.7, 1547.8, and 1551 nm as shown in Figure 6.17.

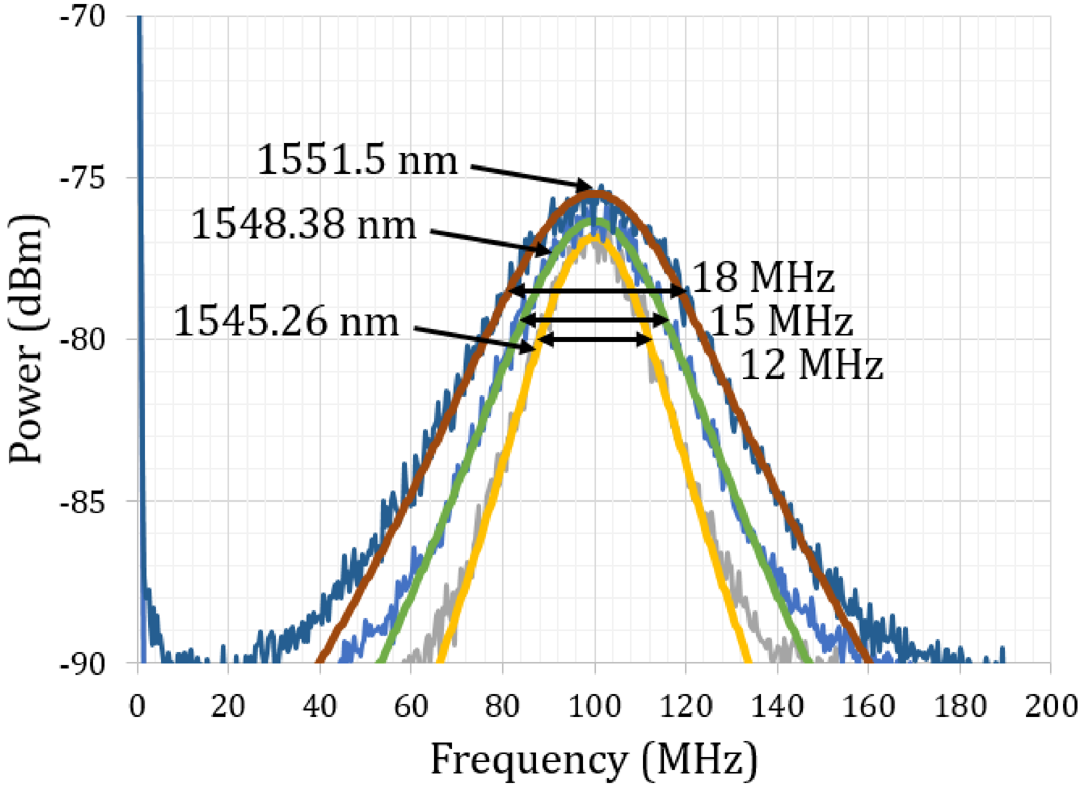

Figure 6.16. Linewidth measurements with Lorentzian fits of the SG-DBR local oscillator under CW operation with a constant 100 mA gain bias at 1545.26, 1548.38, and 1551.5 nm using a delayed self-heterodyne with a 20 km delay line. Laser was biased using Keithley current sources. Measurement setup is presented in Figure 6.15. Laser was temperature controlled to 15°C.

One possible mechanism for the linewidth broadening is carrier fluctuations in the current source directly modulating the mirror and gain section causing a carrier-induced index shift that modulates cavity length. By switching to a thermally tuned mirror, the SG-DBR laser's linewidth could be greatly reduced, as demonstrated in [61].

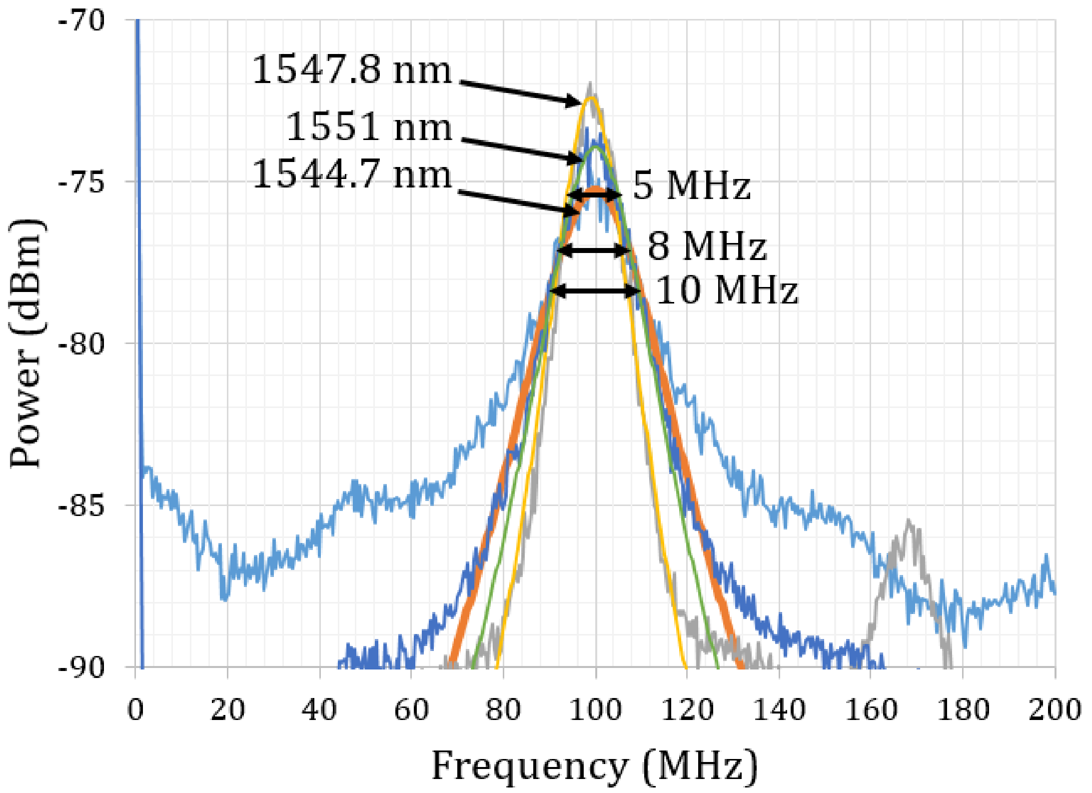

Figure 6.17. Linewidth measurements with Lorentzian fits of the SG-DBR local oscillator under CW operation biased by two 1.5V AA batteries on both the gain and front mirror sections at 1544.7, 1547.8, and 1551 nm using a delayed self-heterodyne with a 20 km delay line. Measurement setup is presented in Figure 6.15. Laser was temperature controlled to 15°C.

6.1.6 90° Optical Hybrid

The next step in characterizing the coherent receiver was to measure the output balance and phase tuning of the 90° optical hybrid. Any difference in optical power among the photodiodes will result in an imbalance in the recovered signal that can result in detection errors. The output power detected in each photodetector with the local oscillator biased on was 200-300 μA. Using the LO as a source, the imbalance between the photodiodes was less than 1 dB, sufficiently low enough for the DSP to account for. This imbalance was likely caused by defects in the waveguides of the 90° optical hybrid rather than due to an improperly designed MMI, as any power imbalance in two adjacent photodiodes was typically due to one output having a much lower power while the other remained similar to all of the other photodiodes on the chip rather than the adjacent photodiode having more power than the others.

As the DSP used to detect the signal was designed to recover the QPSK signal at 90° out of phase, the phase of the LO on the Q arm of each hybrid needed to be tuned 90° out of phase with the I arm, as any deviation would result in increased phase errors during decoding. To measure the phase tuning efficiency of the electro-optic phase shifter and map the quadrature point of the hybrid, an external cavity laser was coupled to the signal input of the hybrid and tuned close to the output of the on-chip local oscillator until a beat frequency at 4 GHz between the two optical sources was generated, which was low enough to be detected by the photodiodes. The phase difference between the I+ and Q+ photodiodes was then measured on a digital storage oscilloscope, as presented in

Figure 6.18. The electro-optic phase shifter was then swept from 0-20 mA to map the phase points of the hybrid. Using 1.55 mA bias, the hybrid was set at a 90° phase offset between the I and Q outputs.

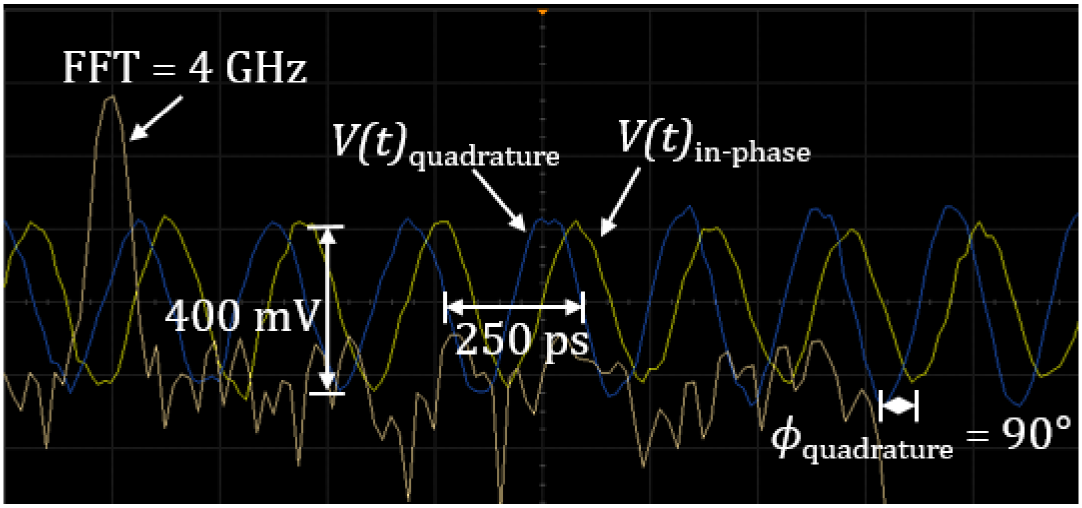

Figure 6.18. Trace of $V(t)_{\text{in-phase}}$ and $V(t)_{\text{quadrature}}$ outputs from I+ and Q+ photodiodes captured in a digital storage oscilloscope showing an optimal 90° offset between the received signals. Beat signal was generated using a CW external cavity laser signal amplified with an EDFA to 20 dBm coupled to the chip through a 2μm spot size lensed fiber. On-chip LO was biased 100 mA on the gain section for a 1548 nm output and the external cavity laser was tuned to generate a 4 GHz tone. Quadrature phase shifter was biased to 1.55 mA to reach 90° phase offset between the I and Q outputs. Receiver was temperature controlled to 15°C.

Chapter 7

Coherent Receiver System Testing and Discussion

7.1 Dual Channel Coherent Receiver PIC with Tunable Local Oscillator

With the photodiode, local oscillator, waveguide, and 90° hybrid operation verified, a coherent receiver PIC was designed and fabricated as presented Figures 7.1 and 7.2, respectively. The receiver consists of two parallel 90° optical hybrids for reception of two independent polarizations along with eight 30 GHz photodiodes and an on-chip SG-DBR local oscillator.

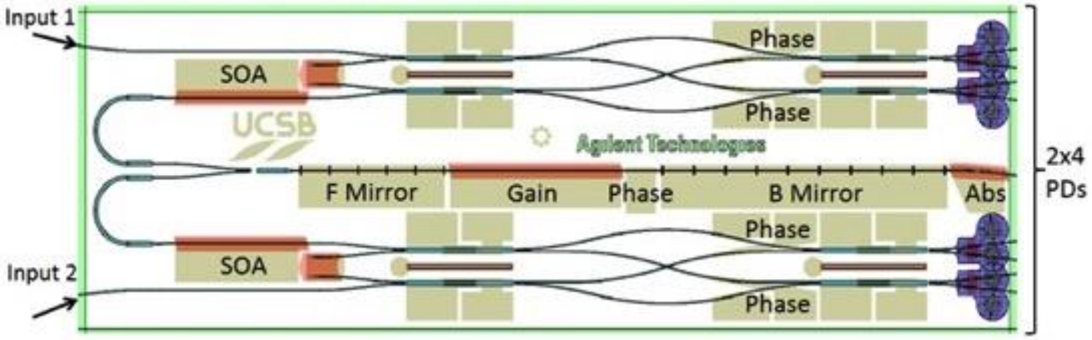

Figure 7.1. Schematic diagram of the dual channel coherent receiver with integrated widely tunable local oscillator. Reprinted with permission from [78].

Figure 7.2. Image of the fabricated dual channel coherent receiver. Reprinted with permission from [78].

7.2 Net Responsivity

To verify performance of the receiver, the net responsivity defined in Section 2.5 was first measured. The responsivity was measured from 1460 to 1580 nm. The I+ and Q+ photodiodes for each polarization were reverse biased at -1.5 volts, producing a dark current of 10-15 μA. An external cavity laser was TE-polarized using a polarization controller to maximize absorption in the quantum wells and coupled to one channel at a time using a 2 μm spot size lensed fiber, and the resulting photocurrent generated was measured with a Keithley 6221. Figure 7.3 shows the resulting responsivity exhibiting a maximum responsivity of 0.28 A/W at 1515 nm and a 3 dB bandwidth of 74 nm occurring from 1474 to 1548 nm.

The net responsivity includes 6 dB of splitting loss in the hybrid as well as the reduced 0.75 A/W responsivity of the shorter photodiodes. From these values, the excess loss of the receiver is 9.1 dB including 5 dB of coupling loss due to mode mismatch and reflection at the input facet and 4.1 dB of propagation loss.

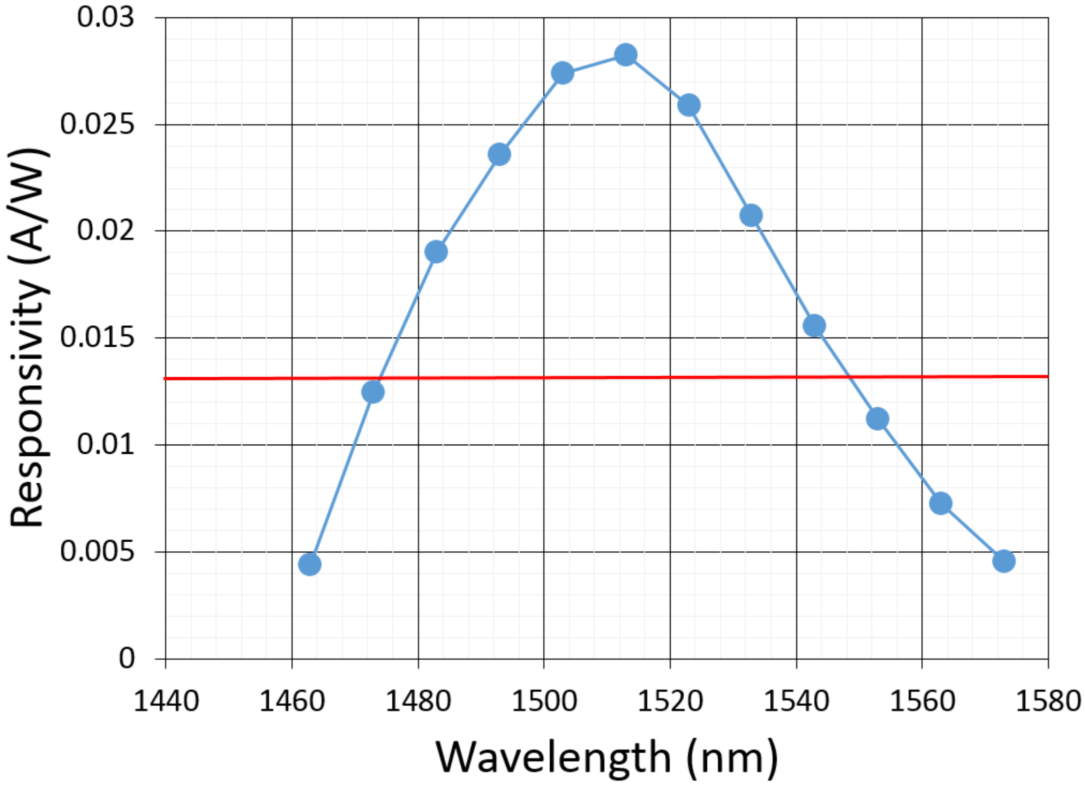

Figure 7.3. Net responsivity of the coherent receiver PIC measured at the photodiodes as a function of wavelength from 1460-1580 n. A TE-polarized 0 dBm input was coupled from an external cavity laser to the receiver with a 2 μm lensed SMF fiber. The on-chip laser was left off while the hybrid phase tuner was biased to 1.55 mA. 10-15 μA leakage and 5-30 μA photocurrent were measured at the photodiodes for a -1.5 V reverse bias. Receiver was temperature controlled to 15°C. Reprinted with permission from [78].

7.3 50 Gbps NRZ-QPSK Operation

Prior to full link testing, pre-distortion feedback was programmed into the Keysight optical modulation analyzer used to demodulate the QPSK signal to linearize the channel and account for imperfections in the 90° optical hybrid, photodiodes, and RF cables as detailed in Section 2.4. The OMA features a built-in integrated coherent receiver test that determines the correct calibration values for the receiver, including I-Q power imbalance, cable skew, and the I-Q phase [32]. This was performed by sweeping an external cavity laser coupled into the receiver to generate a beat frequency with the on-chip local oscillator that is swept from 2 to 20 GHz while simultaneously measuring the resulting amplitude and phase in the I+ and Q+ photodiodes to generate the calibration values for the receiver.

To characterize the practical phase noise of the local oscillator, an external cavity laser with a 100 kHz linewidth was coupled to the receiver and tuned to generate a beat tone with the LO, and the RF spectrum of the resulting beat tone was measured from one of the photodiodes. The linewidth of the beat tone was 130 MHz, much greater than the linewidth of either individual laser due to the independent drift from thermal fluctuations and vibrations of each individual laser resulting in a much larger total 1/f noise.

To verify the full operation of the coherent receiver in a coherent transmission link, each of the two input channels were tested individually with a 50 Gbps NRZ-QPSK signal generated from the CW output of an external cavity laser modulated by a Fujitsu 100G DP-QPSK modulator; a schematic diagram of the test setup is presented in Figure 7.4. A polarizing beam splitter cube was used before the receiver inputs to separate incoming polarization-multiplexed signals; the TE path was fed directly to one channel, while the TM signal was rotated to the TE orientation using a polarization controller before being fed to the other channel to allow for compatibility with the LO signal. The optical signal was pre-amplified to 20 dBm using an EDFA and filtered with a 0.4 nm tunable filter before being coupled into the chip, and the received photocurrents were amplified with an RF amplifier before being decoded in the OMA. 3 different wavelengths were tested to verify the wavelength tunable receiver operation, and the recovered constellations at 20 dB OSNR are presented in Figure 7.5.

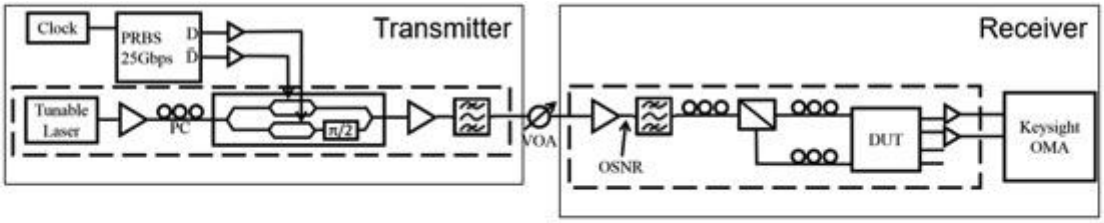

Figure 7.4. Diagram of the test setup for 50 Gbps NRZ-QPSK testing. The CW output of an external cavity laser was modulated by a Fujitsu 100G DP-QPSK modulator and amplified in an EDFA. OSNR was controlled using a variable attenuator in front of the receiver EDFA. Receiver signal was pre-amplified to 20 dBm by an EDFA, TE-polarized, and coupled to the chip using a 2 μm spot size lensed fiber. Electrical output signals from the receiver were amplified using 30 GHz broadband amplifiers and captured in a Keysight OMA. Receiver was temperature controlled to 15°C. Reprinted with permission from [78].

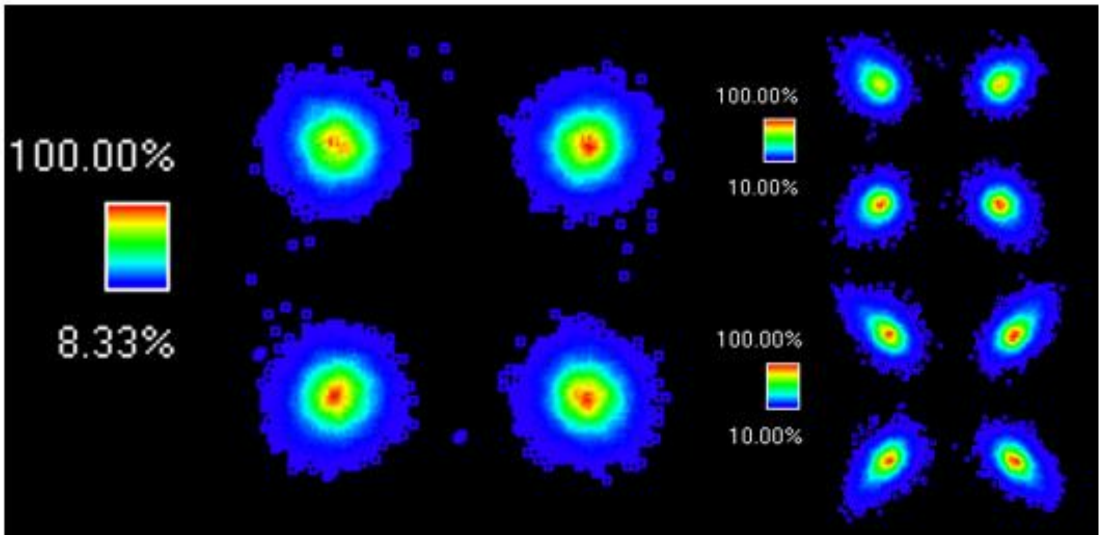

Figure 7.5. Recovered constellations at 3 different wavelengths for 50 Gbps NRZ-QPSK data into a single channel: 1545.26 nm left, 1548.38 nm top right, 1551.5 nm bottom right using the test setup from Figure 7.4. Receiver signal was pre-amplified to 20 dBm by an EDFA, TE-polarized, and coupled to the chip using a 2 μm spot size lensed fiber. Electrical output signals from the receiver were amplified using 30 GHz broadband amplifiers and captured in a Keysight OMA. Receiver was temperature controlled to 15°C. Reprinted with permission from [78].

The BER was then measured versus the incoming signal's OSNR; the curves for the 3 wavelengths are presented in Figure 7.6. An error floor was measured at 10^{-8}, and a BER of 10^{-3} was achieved at an OSNR of 7.5 dB for the 1548.38 and 1551.5 nm wavelengths. The error floor at 22 dB of OSNR shown in Figure 7.6 was caused by the large linewidth of the beat frequency between the carrier wave and local oscillator adding significant phase noise to the measurement. An OSNR of 11.5 dB was required to achieve the same BER at 1545.26 nm; this increase may be due to greater noise from the EDFA at this wavelength. The Kalman filter carrier phase recovery algorithm was used during demodulation to enable the DSP to track the absolute phase of the received signal. A constellation of the received signal at 1551.5 nm without the phase tracking algorithm is shown in Figure 7.7. Without the phase tracking, the phase information is lost, resulting in the constellation points rotating around their absolute phase points until the data cannot be recovered.

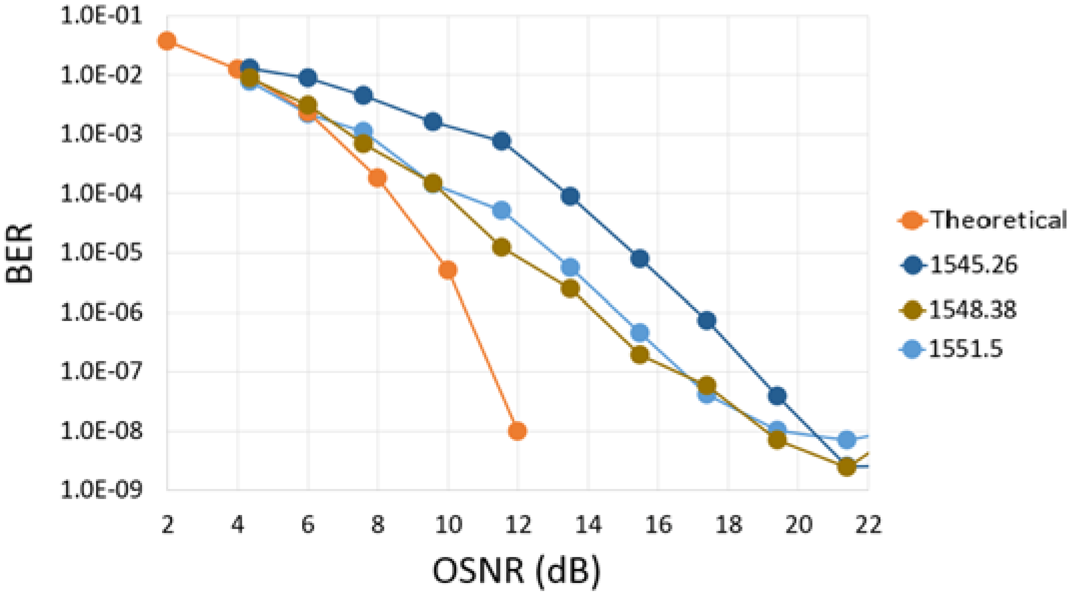

Figure 7.6. Measured BER vs. OSNR for 50 Gbps NRZ-QPSK data into a single channel. OSNR was controlled using a variable attenuator in front of the receiver EDFA. Receiver signal was pre-amplified to 20 dBm in an EDFA, TE-polarized, and coupled to the chip using a 2 µm spot size lensed fiber. Electrical output signals from the receiver were amplified using 30 GHz broadband amplifiers and captured in a Keysight OMA. Receiver was temperature controlled to 15°C. Reprinted with permission from [78].

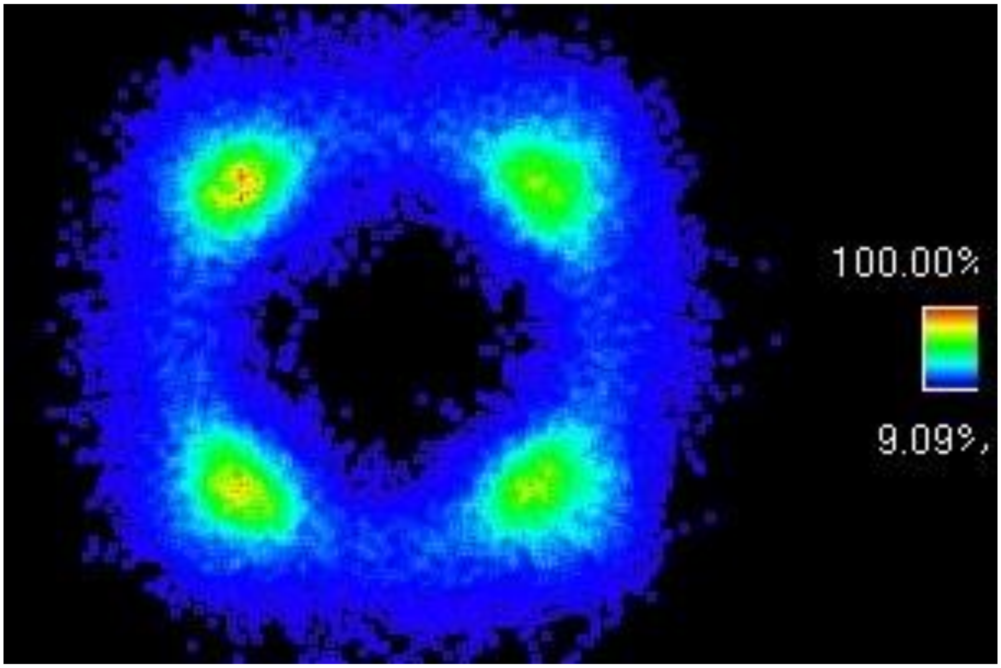

Figure 7.7. Recovered constellation at 1551.5 nm with reduced loop gain in the Kalman filter carrier phase tracking loop. Increased phase errors result from insufficient feedback signal.

7.4 Loss Budget and Receiver Noise Figure

The receiver's loss budget and noise figure were measured using the analysis presented in Section 2.5. For the 30 GHz bandwidth of the photodiodes, at 293 K the thermal noise current is 3.12 μA. The receiver's sensitivity was determined from the noise equivalent power. A beat frequency was generated at 2.5 GHz between the LO and an external cavity laser at 1548.38 nm and coupled to the receiver. The RF output of one of the photodiodes was then measured to determine the difference between the signal power and the noise power on an RF spectrum analyzer for a given input photocurrent to the receiver. For an optical signal power of -19.7 dBm at the photodiode, the SNR was 12 dB in the spectrum analyzer, resulting in a noise equivalent power of -31.7 dBm at the photodiode. As the receiver had roughly 15.22 dB of loss, the noise equivalent power at the front of the receiver was -16.48 dBm. For a desired optical signal to noise ratio (OSNR) of 20 dB, the resulting sensitivity at the front of the receiver was 3.5 dBm and the noise figure of the receiver was 9.5 dB.

The relative intensity noise (RIN) of the LO was also measured at 1548.1 nm and the resulting sweep is presented in Figure 7.8. Peak RIN of the laser is -138 dBc/Hz through 3 m of fiber at 4.5 GHz which is the relaxation frequency of the laser; this result is similar to that in [82]. Above this frequency the RIN is diminished, so the resulting noise contribution to the receiver may be approximated as the sum of the noise below 4.5 GHz. Using the peak RIN as a high approximation for the entire spectrum of noise within the 4.5 GHz band, the resulting optical noise level is -37.2 dBm, much lower than the thermal noise of the receiver. As such the RIN has no significant effect on the noise of the receiver.

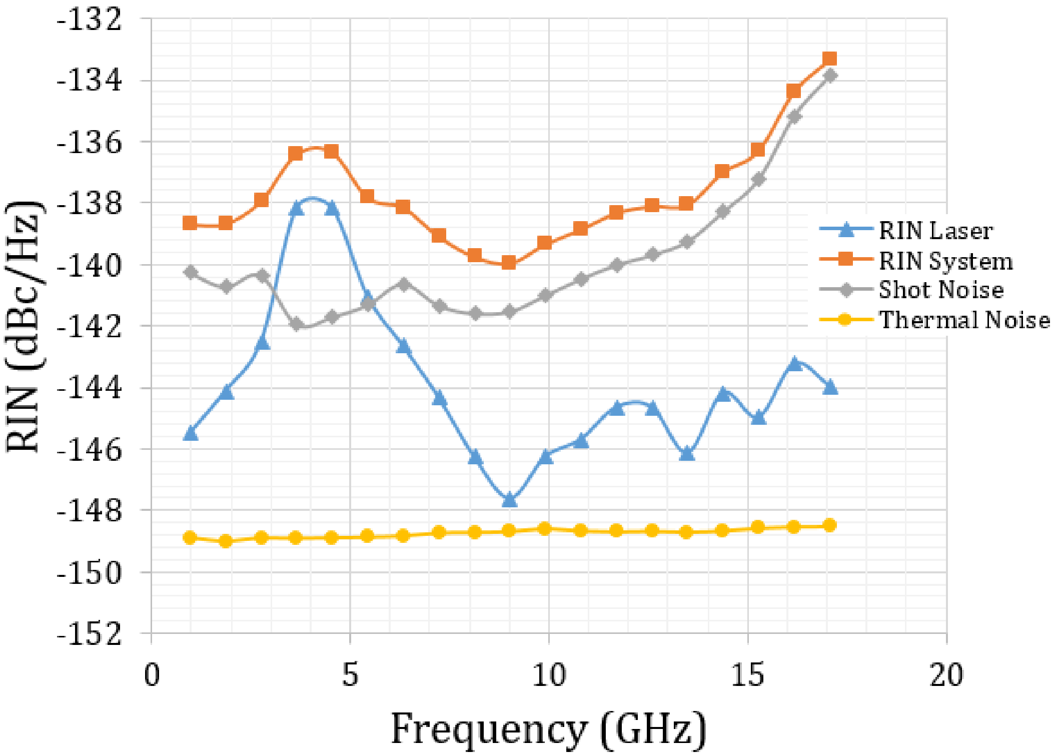

Figure 7.8. RIN measurement of the SG-DBR laser at 1548.1 nm. Gain section was biased to 210 mA. Input power was 0 dBm coupled to Keysight RIN measurement system through an SMF lensed fiber with a 2 µm spot size. Laser was temperature controlled to 15°C.

7.5 Summary and Discussion

Several achievements were met on the dual channel coherent receiver. First, 30 GHz photodiodes were demonstrated for the first time on the offset quantum well platform without the need of a second regrowth. This allowed for integration of a tunable SG-DBR laser on the same chip, greatly reducing the complexity of the receiver system. In addition, 50 Gbps NRZ-QPSK per channel data reception was demonstrated for 100 Gbps total capacity, one of the highest per-channel bitrates ever demonstrated for a monolithically integrated coherent receiver with an on-chip LO. These accomplishments prove the viability of integration of both gain and high speed components on a common epitaxial design.

Table 7.1. Comparison of goal performance and actual measured results for the coherent receiver.

Design Attribute	Goal Performance	Measured Performance	Comments
Linewidth	< 10 MHz	5-10 MHz	DC biasing required, could narrow with thermal tuning
Wavelength Stability	± 0.1 nm	<0.1 nm	Temperature control required
Wavelength Range	> 40 nm	40 nm	Could increase with DBR redesign
Sensitivity	< 4 dBm	3.5 dB	Could reduce with coupling loss, longer photodiode, reduced waveguide loss
Bandwidth	> 25 GHz	30 GHz	
Power Dissipation	< 1 W	0.5 W	Could reduce with narrower waveguides
Physical Size	< 5 mm^2	3 mm^2	Could reduce using TIR mirrors

Table 7.1 presents a comparison of the design goals for important features of the receiver and their measured performance. All stated metrics were successfully achieved for the coherent receiver, but there were several areas identified in the testing where the receiver’s performance could be improved. First, the linewidth

of the heterodyne receiver was quite large due to independent fluctuations between the carrier signal and LO; while a software-enabled phase-lock loop was implemented to overcome this limitation, an error floor was still present in the BER measurement at 10^{-8}. Due to the increased constraints on SNR, higher order modulation formats such as 16 QAM would likely be impossible on the receiver without some form of hardware feedback to compensate for the large linewidth generated by the two lasers. Additionally, due to the excess loss of the receiver, the photocurrent out of the detectors was low and needed to be amplified using broadband RF amplifiers before it could be processed in the electronics, adding more complexity to the system. Using on-carrier trans-impedance amplifiers directly connected to the photodiodes would greatly reduce the complexity of the system. Finally, the polarization demultiplexing was deemed impractical due to the high scattering loss in the narrow waveguide structures required to produce the necessary mode interaction with the asymmetry of the waveguide. However, by switching to a narrower wavelength source for the lithography, the waveguide loss in these narrow waveguides could be reduced, allowing for on-chip integration of more optical components of the receiver.

Chapter 8

16x16 MOTOR Switch Component Characterization

As the switch requires over 81 optical functions working at the same for full operation, several individual functions were verified before full switch testing was started. These components were the SOAs and MZM, which serve as the primary mechanisms for the wavelength conversion, the AWGR, which performs the wavelength routing function, and the pump laser which acts as the selectable switch in the system.

8.1 Semiconductor Optical Amplifiers

First the gain of the SOAs was measured for varying injection current to determine the optimal operation point of the amplifier. An external cavity laser was coupled to the SOA through a lensed fiber and the output power from the SOA was measured in a reverse-biased SOA downstream. The current was swept from 0 mA until the optical power began to roll over indicating the thermal roll-off point of the device. For the booster SOAs downstream of the on-chip laser, the on-chip laser was used to generate the signal source. To test the MZI SOAS, a lensed fiber was coupled to the AWGR output in order measure the output power of the device. The resulting bias points are 80 mA and 220 mA for the input and MZI SOAs.

Next, input saturation power of the SOAs was measured by sweeping the input power at the SOA and measuring the resulting output power. The resulting sweeps for the input and MZI SOAs are presented in Figures 8.1 and 8.2, respectively, showing a 1-dB gain saturation power of 5.3 and -1.5 dBm for the input and MZI SOAs, respectively.

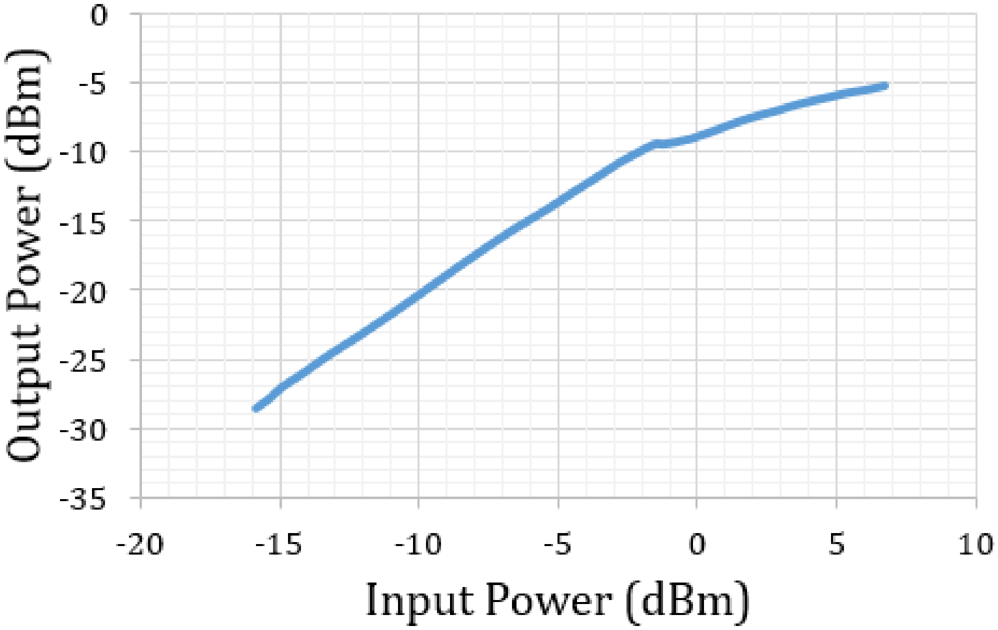

Figure 8.1. Plot of optical output power versus input power of a 200 x 3 μm input SOA biased at 80 mA. A CW input signal was generated from an external cavity laser at 1540 nm amplified through an EDFA passed through a 0.4 nm filter to remove ASE. Input power controlled by an optical attenuator. Signal was coupled to the SOA through a SMF lensed fiber with a 2 μm spot size and output power was measured in downstream MZI SOA after passing through a 3d dB splitter. SOA was

temperature controlled to 15°C. 1 dB gain saturation point was observed at 5.3 dBm input power.

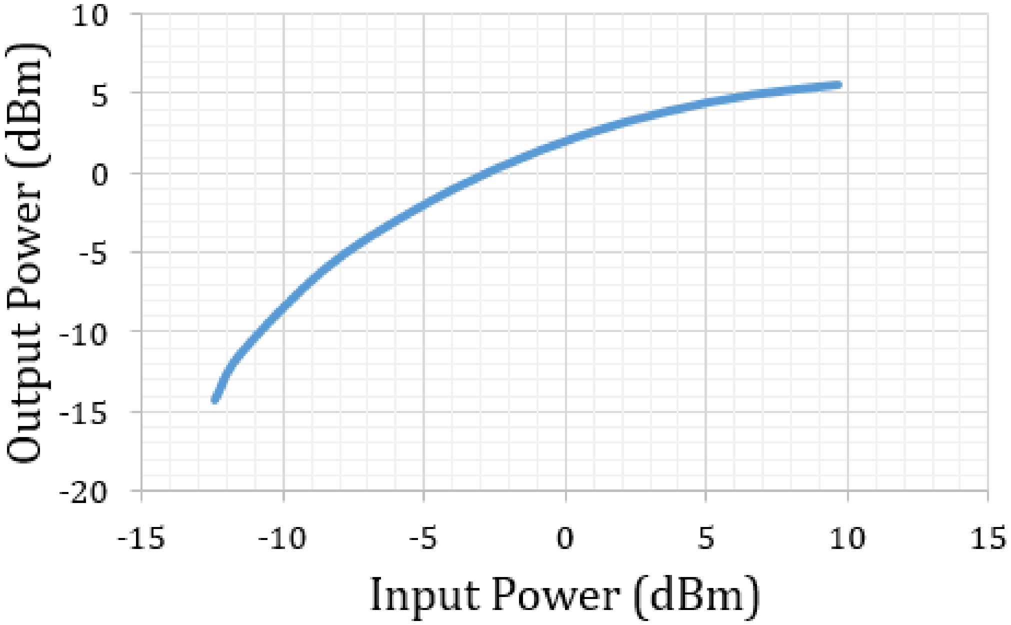

Figure 8.2. Plot of optical output power versus input power of a 1 mm x 3 μm MZI SOA biased at 220 mA. A CW input signal was generated from an external cavity laser at 1540 nm amplified through an EDFA passed through a 0.4 nm filter to remove ASE. Input power was controlled by adjusting the upstream input SOAs. Signal was coupled to the SOA through a SMF lensed fiber with a 2 μm spot size and output power was measured in an off-chip power meter coupled to the AWGR through a SMF lensed fiber with a 2 μm spot size. SOA was temperature controlled to 15°C. 1 dB gain saturation point was observed at -1.5 dBm input power and saturated output power was 5 dBm.

8.2 Arrayed Waveguide Grating Router

Next the 16x16 AWGR filter used to direct the converter arrays' outputs to one of 16 ports was characterized. To generate a broadband light source, the MZI SOA of wavelength converter 8 was biased at 210 mA creating approximately -3 dBm of ASE noise coupled to the AWGR. Each output port was then probed with a lensed fiber and the resulting spectrum was measured with an OSA; a plot of the output from each port is presented in Figure 8.3 with all of the passband maxima normalized.

AWGR channel spacing was 1.45 nm, and the average FWHM of each passband was 0.6 nm. Minimum channel crosstalk measured as the difference between the peak amplitude of the passband and residual side modes was 17 dB. The insertion loss defined as the loss from the output of a wavelength converter to the output of the AWGR was measured by coupling an external cavity laser to the output of the AWGR using a lensed fiber and measuring backwards to the SOAs of a wavelength converter. Total insertion loss of the AWGR was 10-15 dB depending on the path taken, or roughly 1-1.5 dB/mm through the 10 mm long waveguide.

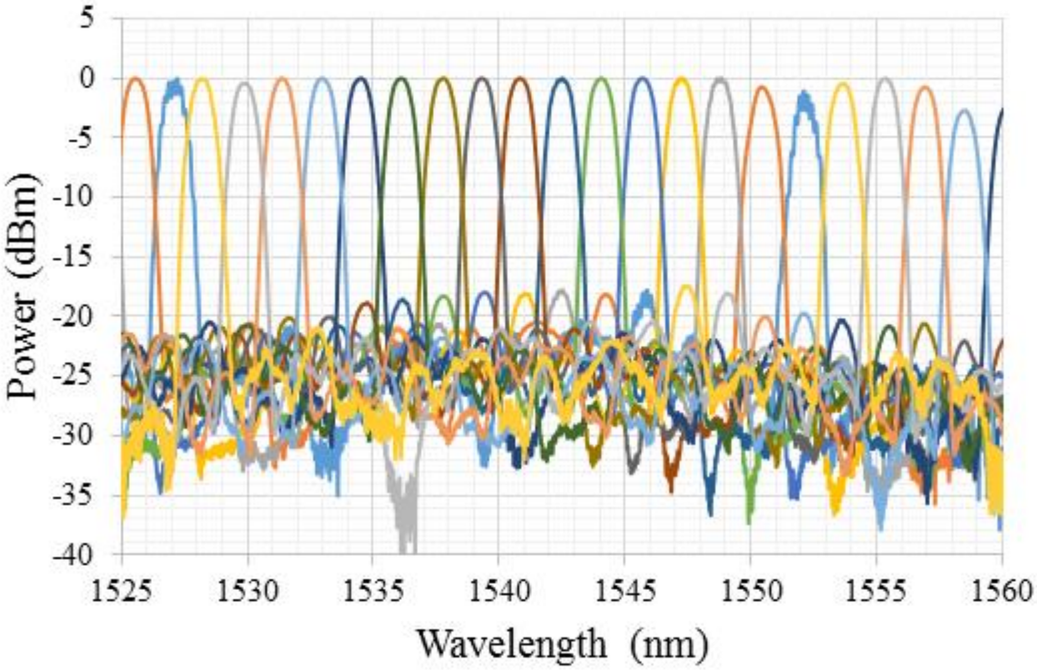

Figure 8.3. Output spectrum of each output port of the AWGR normalized to their passband maxima with the MZI SOAs of wavelength converter #8 biased at 210 mA to provide ASE output. The 2.5x1.7 mm 100-arm AWGR has a 25 nm free spectral range with 10-15 dB loss through the device. Output port 1 is located at 1525.6 nm and output port 16 is at 1548.8 nm. Secondary passbands begin above 1550 nm due to the 25 nm free spectral range of the AWGR. Switch was temperature controlled to 15°C.

To determine the effect of ASE noise due to several wavelength converters running at once, 8 of the wavelength converters' MZI SOAs were biased at 210 mA and one of the outputs of the AWGR was again measured. The resulting spectrum is plotted in Figure 8.4 showing a crosstalk reduced to 10 dB as well as significant channel imbalance. In Figure 8.5, the channels are rebalanced by adjusting the gain of the MZI SOAs to match the output power of the weakest passband. Minimum crosstalk remained 10 dB for the adjusted output.

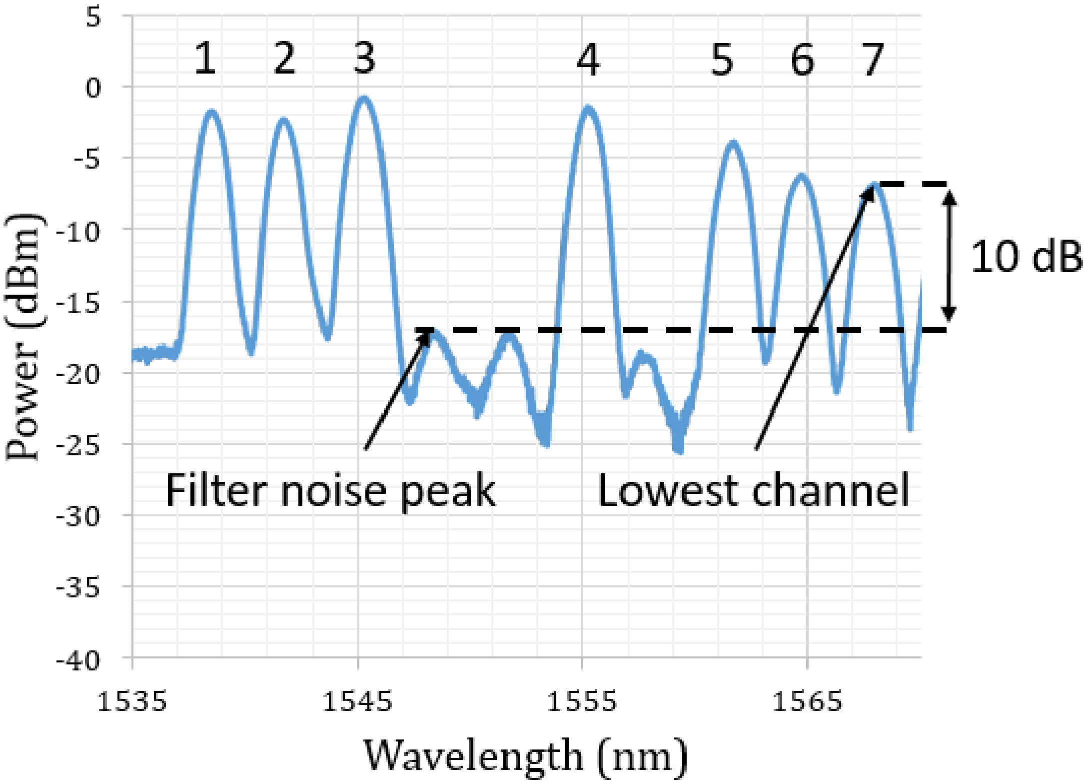

Figure 8.4. Output spectrum from one port of the AWGR with 8 wavelength converter MZI SOAs simultaneously biased at 210 mA. Channels imbalance are caused by additional loss due to path length differences through the waveguides to and from the AWGR but can be adjusted by changing the gain of the MZI SOAs. Switch was temperature controlled to 15°C.

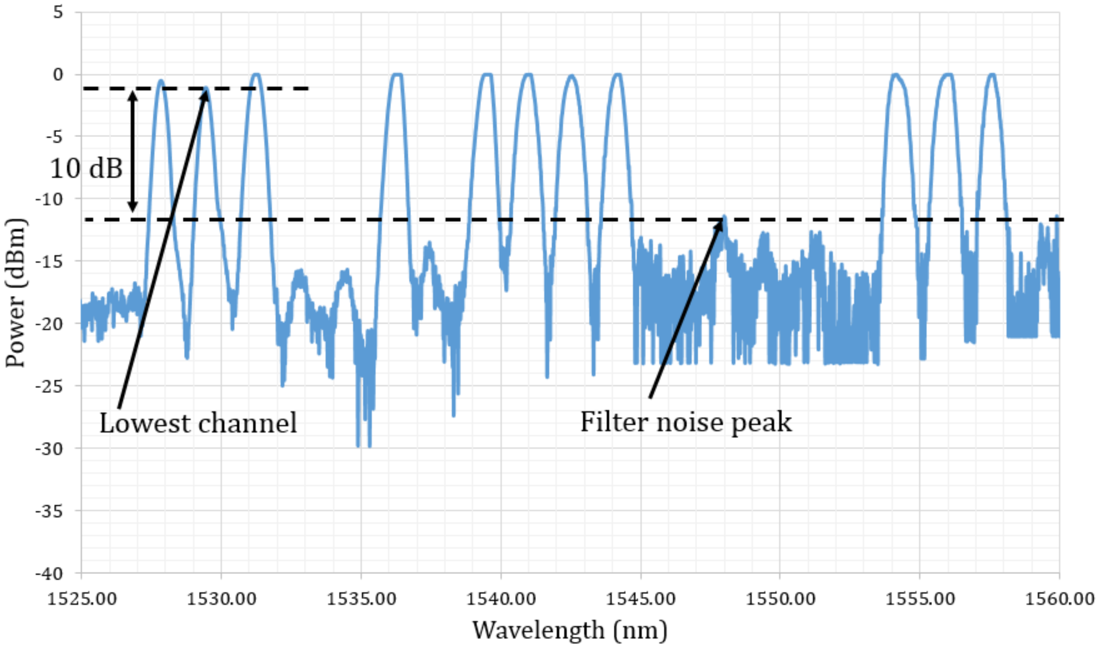

Figure 8.5. Output spectrum from one port of the AWGR with 8 wavelength converter MZI SOAs adjusted for balanced outputs. Switch was temperature controlled to 15°C.

8.3 Mach-Zehnder Modulator

The MZI features two modes of operation: electrical to optical modulation, in which the electro-optic phase shifters on the MZI can be used as EAMs to modulate the electric field of the CW light source from the on-chip SG-DBR laser, or optical to optical modulation, in which the CW light source is modulated by another incoming optical signal. The electro-optic response of the modulator was measured by turning on the pump laser and MZI SOA then sweeping the current of one of the phase shifters and measuring the resulting output. The pump laser's booster SOAs were biased such that the input power was -3 dBm to each SOA. A maximum extinction ratio of 15 dB was found over the first period. A minima in the output power occurred at a 2 mA bias in the phase shifter, while maximum output power was achieved at a 1 mA bias. As the tuning current was increased, the maxima and minima of the output power were reduced, likely caused by increased electro-optic absorption in the phase section imbalancing the output of the MZM resulting in reduced interference strength.

8.4 Tunable Pump Laser

The tunable laser in the all-optical switch used a similar design to that in the coherent receiver resulting in a similar L-I characteristic and wavelength tuning range. The L-I curve of the laser is shown in Figure 8.6, exhibiting a 55 mA threshold current and 4.84% differential efficiency. Maximum output power was 13 mW occurring at a 210 mA bias into the gain section of the laser. The side mode suppression ratio (SMSR) and wavelength range could not be individually measured for the laser due to the AWGR placement between the laser and output.

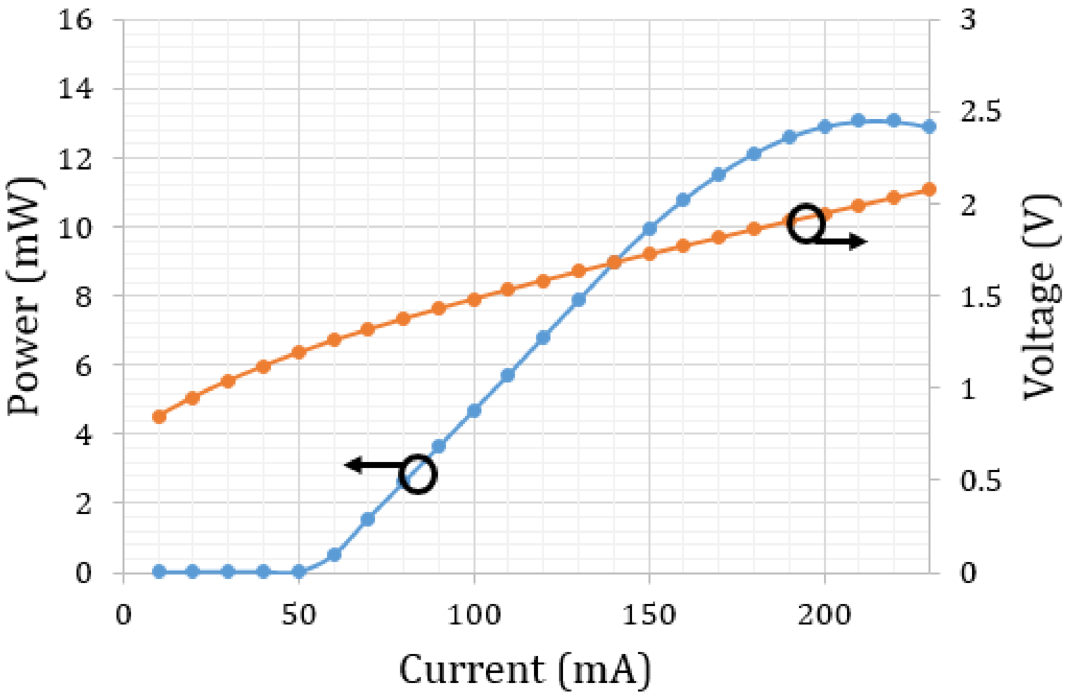

Figure 8.6. Plot of CW operation of the SG-DBR pump laser measured in the reverse-biased booster SOAs. Mirror and phase sections were left unbiased. Laser was temperature controlled to 15°C.

Chapter 9

16x16 MOTOR Switch System Testing and Discussion

9.1 10 Gbps Single-Ended and 40 Gbps Differential Operation

An image of the complete all-optical switch with the wavelength converter array and AWGR outlined is presented in Figure 9.1. The performance of the switch was first tested by switching the wavelength and output port of an incoming 10 Gbps signal. The signal was generated by modulating an external cavity laser with an amplitude-shift keyed NRZ signal with a PRBS 2^7-1 bit pattern at 10 GHz; the test setup is presented in Figure 9.2. The input signal was pre-amplified to 20 dBm using an EDFA and filtered with a 0.4 nm tunable filter before being coupled into the chip. The SOA on the delay line used for differential operation was reverse biased to avoid interference with the single-ended performance of the device. The pump laser was tuned to 1550.45 nm resulting in the signal coming out of port 15 of the AWGR. The signal was then collected in a lensed fiber with a 2 μm spot size, passed through a 5 nm filter to remove the source signal, amplified in an EDFA, and measured in an optical sampling oscilloscope.

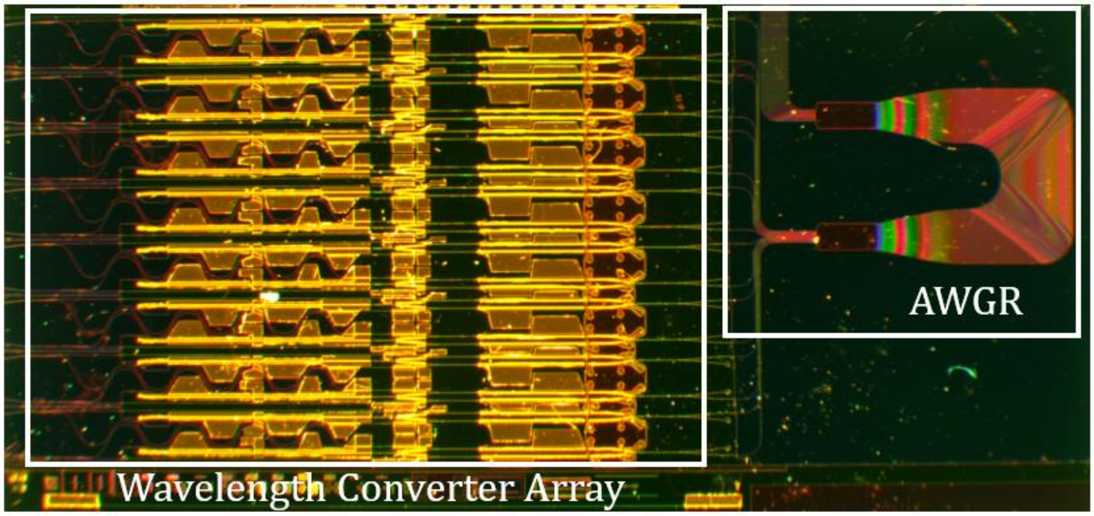

Figure 9.1. Image of the fabricated 16x16 monolithically integrated all-optical switch with wavelength converter array and AWGR outlined.

Figure 9.3 shows an open eye diagram of the switched signal on the right, with the original signal on the left, indicating error-free operation. The extinction of the signal was greatly reduced from 20 dB at the input to 8 dB at the output, and the jitter of the signal was increased from 3.5 to 6 ps. At 10 Gbps, the gain recovery time of the SOA had a noticeable effect on the bits, causing long tails on the one-to-zero transition. The gain recovery time was approximately 90 ps measured from the 90%-10% transition time of the tail. Further testing revealed that all 16 output ports were addressable and that all 16 input channels would be functional as they had sufficient photocurrent to drive the MZI SOAs, measured photocurrents for an 18 dBm input and single-ended operation are presented in Table 9.1 for all 16 channels.

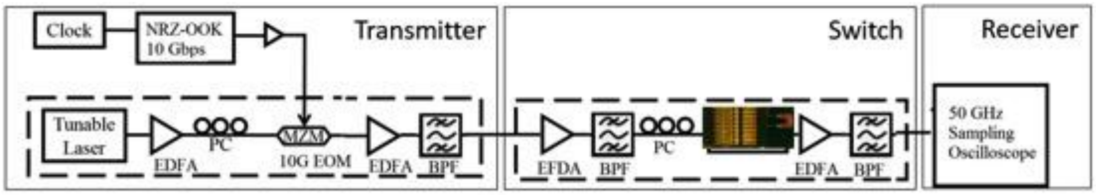

Figure 9.2. Schematic of the setup used for testing 10 Gbps switching.

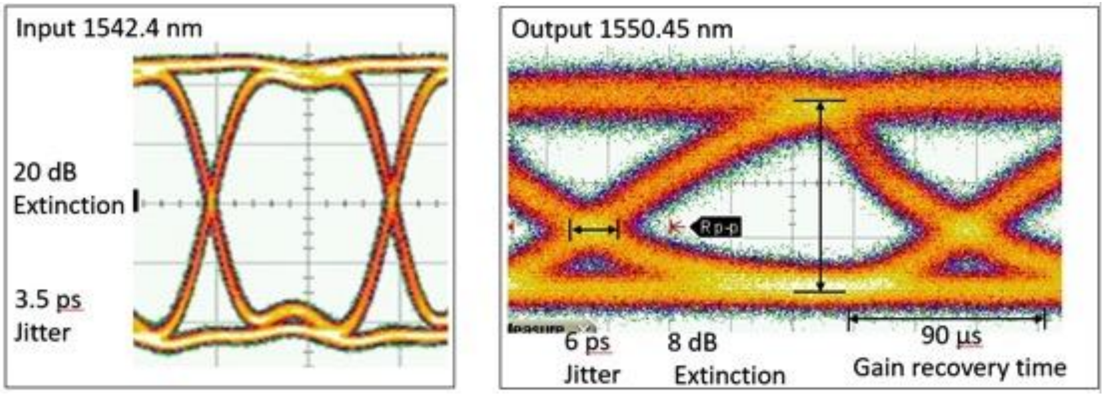

Figure 9.3. Input and output eyes at 10 Gbps through the all-optical switch measured in a Keysight sampling oscilloscope. Input signal was a TE-polarized 10 Gbps NRZ-OOK signal at 1542.4 nm modulated onto a CW external cavity laser output and amplified to 20 dBm in an EDFA. MZI SOAs were biased to 210 mA and input SOAs were biased to 80 mA. The pump laser gain section was biased at 210 mA and tuned to 1550.45 nm using the back mirror. Output of port 15 was coupled to the oscilloscope with a 2 µm lensed fiber. The MZI SOAs typically had 100 µA leakage and >10 mA photocurrent. All output ports and all input channels would be fully addressable for 10 Gbps operation. Switch was temperature controlled to 15°C during testing.

Next a 40 Gbps signal was generated by modulating an external cavity laser with an amplitude shift-keyed RZ signal with a PRBS 2^7-1 bit pattern at 40 GHz and input into the switch. A pulse carver was used to convert a 40 Gbps NRZ signal into an RZ signal as shown in the test setup in Figure 9.4; an RZ signal was utilized to decrease the duty cycle of the one bit thus increasing its peak power for a given average optical power, resulting in higher peak power to better saturate the MZI SOAs. For this test, the SOA on the delay line was biased so that the signal power was 3 dB less than that in the other arm to match the signal power as the bit turns off. The pump laser was again tuned to 1550.45 nm resulting in the signal coming out of port 15 of the AWGR. The signal was then collected in a lensed fiber, passed through a 5 nm filter to remove the source signal, amplified in an EDFA, and measured in an optical sampling oscilloscope. Figure 9.5 shows the eye diagram of the switched signal on the right with significant degradation due to pattern dependence; the original signal is on the left. Further testing revealed that all 16 output ports were fully addressable while only input ports 2, 3, 5, 7, 8, 9, 11, 12, 13, and 15 would be functional due to additional loss through the delay line causing the converted signal to fall below the noise floor of the MZI SOAs. A table of photocurrents detected in each input port during DC testing of the switch are presented in Table 9.1 for an 18 dBm input power. The input power was doubled to 21 dBm during switch testing resulting in twice the photocurrent during switch operation.

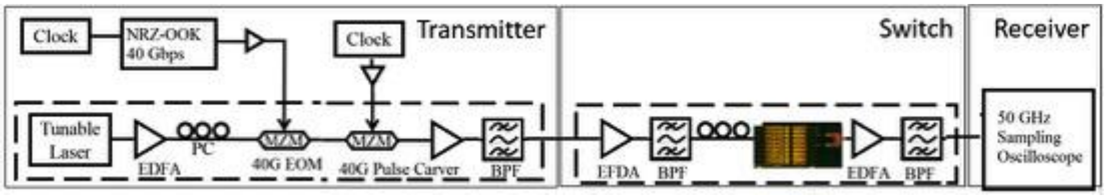

Figure 9.4. Schematic of the setup used for testing 40 Gbps switching.

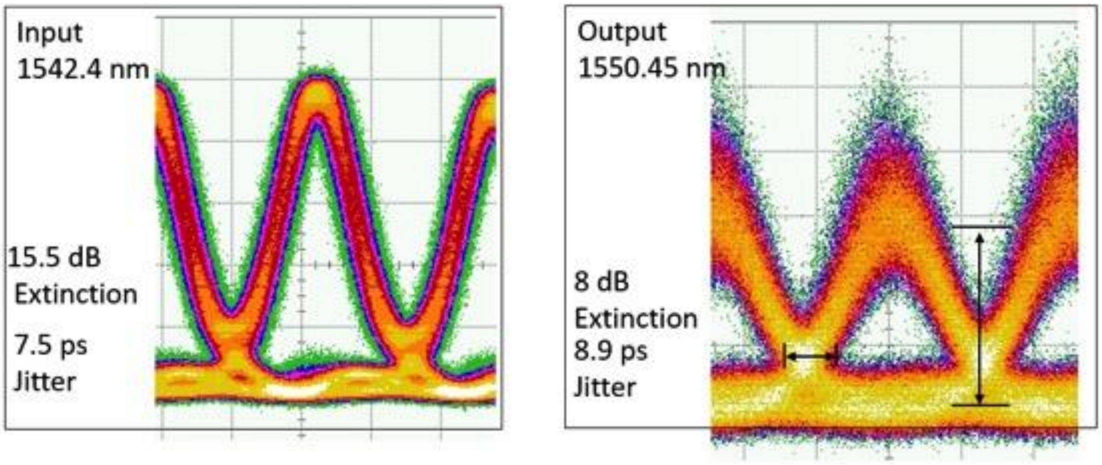

Figure 9.5. Input and output eyes at 40 Gbps from port 8 to port 15 of the all-optical switch measured in a Keysight sampling oscilloscope. Input signal was a TE-polarized 40 Gbps RZ-OOK signal at 1542.4 nm modulated onto a CW external cavity laser output and amplified to 20 dBm in an EDFA. MZI SOAs were biased to 210 mA and input SOAs were biased to 80 mA. The pump laser gain section was biased at 210 mA and tuned to 1550.45 nm using the back mirror. Output of port 15 was coupled to the oscilloscope with a 2 μm lensed fiber. The MZI SOAs had 100 μA leakage and 10 mA photocurrent. Output ports 1-16 were fully addressable while only input ports 2, 3, 5, 7, 8, 9, 11, 12, 13, and 15 would be functional due to excess loss through delay lines in the other converters. Switch was temperature controlled to 15°C during testing.

To investigate the cause of the signal degradation, the switch was again driven with a 10 Gbps NRZ signal, but the primary input SOA was reverse biased to operate the modulator using the delay arm only. Despite driving with the same power at the input, no output signal could be measured due to extra loss from the delay line resulting in insufficient drive power for the SOA. To determine the minimum power required to fully saturate the SOA, input was switched back to the non-delay arm and the power in the SOA was reduced until the signal began to show significant pattern dependence. At 7 dBm or 5 mA of photocurrent, the signal began to show pattern dependence, and by 5 dBm or 3 mA of photocurrent into the SOA, the signal was diminished. As the maximum input power that could be pumped into the delay line was 5 dBm, the delay arm could not be fully driven, and the switch was only able to function in a non-differential configuration for error-free operation. From the photocurrents presented in Table 9.1, devices 2, 3, 5, 7, 8, 9, 11, 12, 13, and 15 would be partially functional due to having greater than 5 mA photocurrent when the input power is doubled to 21 dBm; thus the maximum input photocurrent served as a convenient metric for determining if wavelength converter would operate.

Table 9.1. Summary of photocurrents measured in primary and differential MZI SOAs of each input of the all-optical switch. Input signal generated from a CW external cavity laser amplified to 18 dBm by an EDFA. Signal was further increased to 21 dBm during switch operation. Input power was optimized for

differential or single-ended operation by adjusting the coupling angle into the input splitter to change the resulting power balance at the MZI.

Device Number	Differential		Single	
	$I_{primary}$ (mA)	$I_{differential}$ (mA)	$I_{primary}$ (mA)	$I_{differential}$ (mA)
2	4.1	3.2	N/A	N/A
4	2.1	0.036	10	0.025
6	8.8	1.6	11	0.8
8	4.6	2.5	13	1.2
10	4.3	1.8	11.7	0.6
12	6	3.7	12.5	0.6
14	3.4	2.25	11.8	1.25
16	3	1.4	5.6	1.25
1	5	0.033	12.8	0.015
3	3.4	2.7	14.8	1.65
5	5	2.7	10.1	0.23
7	5	2.8	13.5	0.42
9	3.4	3.4	13.5	0.68
11	3.7	3.5	13.8	0.68
13	3.9	3.25	13.3	0.35
15	3	2.6	12.5	0.85

9.2 Summary and Discussion

Several observations may be made from the results of the MOTOR switch testing. First, the switch successfully demonstrated error-free 16x16 switching with a 10 Gbps signal with the MZM in a single-ended configuration, successfully making use of more than 529 of the 545 components performing 65 of 81 optical functions on a single die and making this one of the largest functional PICs on InP to date. However, the chip's designed 40 Gbps operation was limited by excess loss in the delay lines resulting in insufficient power to differentially operate the modulator. In addition, the MZI SOAs required a minimum of 5 mA of photocurrent to be driven hard enough to generate even a degraded signal; as such, the switch would almost certainly require an EDFA at each port to amplify the input to a sufficiently high level. This large input power was required due to the use of offset quantum wells which have a higher saturation power due to decreased mode overlap with the active region. The switch also had a high idle power consumption, as it required the SOAs to be on no matter which inputs and outputs were in use.

Table 9.2. Comparison of goal performance and actual measured results for the all-optical switch.

Design Attribute	Goal Performance	Measured Performance	Comments
Switching Speed	< 1 ns	Not measured	10-15 ns reported in [60]
Channel Crosstalk	> 20 dB	17 dB single channel, 10 dB 8-channel	Low due to ASE noise from SOAs
Insertion Loss	< 5 dB	18 dB	High loss (~1 dB/mm) in AWGR, can use EDFAs to improve
Wavelength	> 40 nm	40 nm	
Bitrate/Protocol Transparent	> 40 Gbps ASK	10 Gbps ASK	Limited by delay line loss
Nonblocking	Yes	Yes	
Power Dissipation	< 2 W	~2 W, 3W including TEC	Could reduce with smaller SOAs
Physical Size	< 50 mm^2	50 mm^2	50% used by AWGR, use TIR mirrors to reduce footprint

Table 9.2 lists the goal performance of several characteristics of the all-optical switch along with the measured performance. To improve the operation of the MOTOR switch and enable 40 Gbps operation, the optical power required to drive the SOAs must be reduced. Although the OQW approach was chosen for higher yield, a QWI approach has lower input saturation power and would greatly reduce

the optical power required to drive the MZM. Similar to the coherent receiver, the use of TIR mirrors in place of the strip waveguide would reduce the loss in the delay line and further improve the differential operation.

Chapter 10

Conclusions and Future Work

From the work presented in this thesis, it is clear that larger scale monolithic integration of optical systems is not only a viable but an inevitable approach to the advancement of optical communications. The coherent receiver detailed represents the one of the highest bitrates ever demonstrated for a receiver with an on-chip local oscillator with 50 Gbps NRZ-QPSK data reception per channel for a 100 Gbps total capacity, and the MOTOR switch demonstrated one of the largest component counts on a single InP PIC and enabled error-free 16x10 Gbps all-optical switching. In addition to reduced footprint and system complexity, successful integration of more functions on a single chip reduces production costs by enabling components to be fabricated and packaged in a single run. Despite these achievements, there are still several areas in which these two devices could be improved.

10.1 Monolithically Integrated Coherent Receivers

Building upon the successes of the coherent receiver, there are several areas of the device which have noticeable opportunity for immediate improvement. One of the largest limitations of the receiver was the relatively large linewidth of the local oscillator due to the current injection used to tune the mirrors. To overcome the noise from current injection, thermally tuned SG-DBR lasers have been demonstrated with linewidths less than 300 kHz over a 40 nm tuning range [61] that are fully compatible with the integration platform used for the coherent receiver in this dissertation. In addition, the large linewidth generated between the carrier and LO due to slow drift between must also be improved to enable higher modulation formats such as 16 QAM; recent work has been done on integrating an optical phase-lock loop with a heterodyne receiver with an SG-DBR laser [34]; this work could be immediately applied to the coherent receiver developed in this work to eliminate the linewidth limitation.

Another area in which the receiver was limited was the low net responsivity resulting from not only excess loss of the PIC but inherent losses as well. The low photocurrents out of the receiver necessitated the use of RF amplifiers in order to interface with the DSP electronics, increasing the complexity of the receiver setup. Rather than use discrete RF amplifiers to amplify the signal, trans-impedance amplifiers placed directly on the carrier could be wired bonded directly to the photodiodes. This would greatly reduce the footprint and complexity of the coherent receiver. In addition, there are several areas in which the receiver's loss could be reduced. First, a longer photodiode could be used to increase the responsivity back up to 1.24 A/W. To minimize coupling loss, an appropriately designed AR coating would eliminate facet reflections, and a spot size converter would minimize coupling loss due to mode mismatch between the fiber and waveguide. On the LO path, the 90° strip waveguide bends used to route the signal could most certainly be replaced with the much simpler and lower loss TIR mirror designs from [80]. As the round trip loss through the bends also served as an on-chip isolator, this would also require an update to the 90° optical hybrid's design by making use of directional couplers instead of 2x2 MMIs to minimize reflections that could destabilize the on-chip LO.

Finally, the inability to integrate polarization demultiplexing was probably the greatest disappointment in this work. The losses for such a tightly confined mode were simply too high to tolerate any significant roughness on the waveguide sidewall. This roughness could likely be reduced by switching to a lithography system with a narrower wavelength source such as a deep UV system to reduce the roughness produced in the hard mask etch; from there it is possible that the attenuation due to scattering could be sufficiently reduced such that the polarization components could end up with low enough insertion loss for practical use in the receiver.

10.2 Monolithically Integrated All-Optical Switches

The strongest limiting factor in the MOTOR switch was the high input power required to drive the SOAs in the MZ modulator. However, several other approaches have been demonstrated for all-optical switching, including the QWI approach mentioned in Section 5.1 as well as butt-joint regrowth [72]. In a butt-joint regrowth approach, the active areas are completely regrown into etched sections of the chip, allowing for maximum flexibility in active layer design through the use of bulk gain regions that can have much greater mode overlap than that of an OQW structure as well as passive regions left completely undoped. This approach is limited by reflections at the interface between the two regions; any area that is unfilled by the regrowth causes significant reflections resulting in increased instability of the on-chip laser as well as jitter on the produced signal. As such, a QWI approach such as that used in the MOTOR chip demonstrated in [63] is likely the best approach for a large all-optical switch. The regrowth-free approach to this integration scheme developed in [70] makes this process even more attractive, as the regrowth proved to be by far the most difficult and low-yield step in the work of this thesis.

Beyond a change of material structure, the waveguide components of the all-optical switch could also be improved similarly to the coherent receiver. In particular, the use of TIR mirrors in the delay lines and even the AWGR would allow for tighter layouts and higher chip density as well as lower loss. Finally, the use of deep UV lithography could also reduce the propagation loss of the waveguides by reducing the scattering due to sidewall roughness. This would also allow the use of narrower waveguides across the chip without increasing scattering loss; this tighter confinement of the optical mode would allow for less surface area of the chip to be electrically pumped to get the same amount of gain, reducing the power dissipation of the chip by lowering its idle current draw.

Bibliography

[1] "The Zettabyte Era–Trends and Analysis," May 2015.

[2] L. G. Kazovsky, G. Kalogerakis, and W. T. Shaw, "Homodyne Phase-Shift-Keying Systems: Past Challenges and Future Opportunities," *Journal of Lightwave Technology* **24**(12), 4876-4884 (2006).

[3] E. Ip, A. P. T. Lau, D. J. Barros, and J. M. Kahn, "Coherent detection in optical fiber systems," *Optics Express* **16**(2), 753-791, OSA (2008).

[4] *Juniper Networks MX Series Interface Module Reference*, Juniper Networks, Inc. (2016).

[5] M. Seimetz, "Laser Linewidth Limitations for Optical Systems with High-Order Modulation Employing Feed Forward Digital Carrier Phase Estimation," in *Optical Fiber Communication Conference/National Fiber Optic Engineers Conference*, p. OTuM2, Optical Society of America, 2008.

[6] H. Bach, A. Matiss, C. C. Leonhardt, R. Kunkel, D. Schmidt, M. Schell, and A. Umbach, "Monolithic 90° Hybrid with Balanced PIN Photodiodes for 100 Gbit/s PM-QPSK Receiver Applications," in *Optical Fiber Communication Conference and National Fiber Optic Engineers Conference*, p. OMK5, Optical Society of America, 2009.

[7] A. Beling, N. Ebel, A. Matiss, G. Unterbörsch, M. Nölle, J. K. Fischer, J. Hilt, L. Molle, C. Schubert, F. Verluise, and L. Fulop, "Fully-Integrated Polarization-Diversity Coherent Receiver Module for 100G DP-QPSK," in *Optical Fiber Communication Conference/National Fiber Optic Engineers Conference*, p. OML5, Optical Society of America, 2011.

[8] A. Matiss, R. Ludwig, J. K. Fischer, L. Molle, C. Schubert, C. C. Leonhardt, H. G. Bach, R. Kunkel, and A. Umbach, "Novel Integrated Coherent Receiver Module for 100G Serial Transmission," in *National Fiber Optic Engineers Conference*, p. PDPB3, Optical Society of America, 2010.

[9] C. R. Doerr, L. Zhang,P. J. Winzer, "Monolithic InP Multiwavelength Coherent Receiver using a Chirped Arrayed Waveguide Grating," *Journal of Lightwave Technology* **29**(4), 536-541 (2011).

[10] C. R. Doerr, L. Zhang, P. J. Winzer, N. Weimann, V. Houtsma, T. Hu, N. J. Sauer, L. L. Buhl, D. T. Neilson, S. Chandrasekhar, Y. K. Chen, "Monolithic InP Dual-Polarization and Dual-Quadrature Coherent Receiver," *IEEE Photonics Technology Letters* **23**(11), 694-696 (2011).

[11] M. Boudreau, M. Poirier, G. Yoffe, and B. Pezeshki, "An Integrated InP Coherent Receiver for 40 and 100 Gb/Sec Telecommunication Systems," in *Optical Fiber Communication Conference and National Fiber Optic Engineers Conference*, p. OMK6, Optical Society of America, 2009.

.

[12] V. E. Houtsma, N. Weimann, T. Hu, R. Kopf, A. Tate, J. Frackoviak, R. Reyes, Y. Chen, C. R. Doerr, L. Zhang, and D. Neilson, "Manufacturable Monolithically Integrated InP Dual-Port Coherent Receiver for 100G PDM-QPSK Applications," in *Optical Fiber Communication Conference/National Fiber Optic Engineers Conference*, p. OML2, Optical Society of America, 2011.

[13] R. Nagarajan, D. Lambert, M. Kato, V. Lal, G. Goldfarb, J. Rahn, M. Kuntz, J. Pleumeekers, A. Dentai, H. Tsai, R. Malendevich, M. Missey, K. Wu, H. Sun, J. McNicol, J. Tang, J. Zhang, T. Butrie, A. Nilsson, M. Reffle, F. Kish, and D. Welch, "10 Channel, 100Gbit/s per Channel, Dual Polarization, Coherent QPSK, Monolithic InP Receiver Photonic Integrated Circuit," in *Optical Fiber Communication Conference/National Fiber Optic Engineers Conference*, p. OML7, Optical Society of America, 2011.

[14] M. Lu, H. C. Park, A. Sivananthan, J. S. Parker, E. Bloch, L. A. Johanssen, M. J. W. Rodwell, and L. A. Coldren, “Monolithic Integration of a High-Speed Widely Tunable Optical Coherent Receiver,” *IEEE Photonics Technology Letters* **25**(11), 1077-1080 (2013).

[15] S. B. Estrella, L. A. Johansson, M. L. Masanovic, J. A. Thomas, and J. S. Barton, "Widely Tunable Compact Monolithically Integrated Photonic Coherent Receiver," *IEEE Photonics Technology Letters* **24**(5), 365-367 (2012).

[16] K. N. Nguyen, P. J. Skahan, J. M. Garcia, E. Lively, H. N. Poulsen, D. M. Baney, and D. J. Blumenthal, “Monolithically integrated dual-quadrature receiver

on InP with 30 nm tunable local oscillator," *Optics Express* **19**(26), B716-B721, OSA (2011). DOI: 10.1364/OE.19.00B716

[17] K. E. Stubkjaer, "Semiconductor optical amplifier-based all-optical gates for high-speed optical processing.," *IEEE Journal of Selected Topics in Quantum Electronics* **6**(6), 1428-1435 (2000).

[18] X. Ma and G. S. Kuo, "Optical switching technology comparison: optical MEMS vs. other technologies." *IEEE Communications Magazine* **41**(11), S16-S23 (2003).

[19] J. P. P. de Carvalho, "Optical Switching Techniques: Device Development and Implementation in Fibre Optic Technology," Universidade do Porto (2007).

[20] R. Kasahara, M. Yanagisawa, T. Goh, A. Sugita, A. Himeno, M. Yasu, and S. Matsui, "New Structure of Silica-Based Planar Lightwave Circuits for Low-Power Thermooptic Switch and its Application to 8 × 8 Optical Matrix Switch," *Journal of Lightwave Technology* **20**(6), 993- (2002).

[21] N. A. Riza and S. Yuan, "Low optical interchannel crosstalk, fast switching speed, polarisation independent 2× 2 fibre optic switch using ferroelectric liquid crystals," *Electronics Letters* **34**(13), 1341-1342 (1998).

[22] C. M. Gallep and E. Conforti, "Reduction of semiconductor optical amplifier switching times by preimpulse step-injected current technique," *IEEE Photonics Technology Letters* **14**(7), 902-904 (2002).

[23] S. Venkatesh, J. W. Son, J. E. Fouquet, R. E. Haven, D. Schroeder, H. Guo, W. Y. Wang, P. Russell, A. Chow, and P. F. Hoffman, "Recent advances in bubble-actuated photonic cross-connect switches," in *Symposium on Integrated Optoelectronic Devices*, pp. 27-35, International Society for Optics and Photonics, 2002.

[24] P. De Dobbelaere, K. Falta, S. Gloeckner, and S. Patra, "Digital MEMS for optical switching," *IEEE Communications Magazine* **40**(3), 88-95 (2002).

[25] S. C. Nicholes, M. L. Mašanović, B. Jevremović, E. Lively, L. A. Coldren, and D. J. Blumenthal, "The World's First InP 8x8 Monolithic Tunable Optical Router (MOTOR) Operating at 40 Gbps Line Rate per Port," in *Optical Fiber*

Communication Conference and National Fiber Optic Engineers Conference, p. PDPB1, Optical Society of America, 2009.

[26] M. K. Smit, X. Leijtens, E. Bente, J. van der Tol, H. Ambrosius, D. Robbins, M. J. Wale, N. Grote, and M. Schell, "A Generic Foundry Model for InP-based Photonic ICs," in *Optical Fiber Communication Conference*, p. OM3E.3, Optical Society of America, 2012.

[27] M. J. Heck, J. F. Bauters, M. L. Davenport, J. K. Doylend, S. Jain, G. Kurczveil, S. Srinivasan, Y. Tang, and J. E. Bowers, "Hybrid Silicon Photonic Integrated Circuit Technology," *IEEE Journal of Selected Topics in Quantum Electronics* **19**(4), (2013).

[28] J. Sun, E. Timurdogan, A. Yaacobi, Z. Su, E. S. Hosseini, D. B. Cole, and M. R. Watts, "Large-Scale Silicon Photonic Circuits for Optical Phased Arrays," *IEEE Journal of Selected Topics in Quantum Electronics*, **20**(4), 264-278 (2014).

[29] C. Zhang, S. Zhang, J. D. Peters, J. E. Bowers, "8 × 8 × 40 Gbps fully integrated silicon photonic network on chip", *Optica* **3**(7), 785-786 (2016).

[30] A. Yariv and P. Yeh, *Photonics: Optical Electronics in Modern Communications (the Oxford Series in Electrical and Computer Engineering)*, Oxford University Press, Inc. (2006).

[31] *Keysight Infiniium 90000 X-Series Oscilloscope - Data Sheet*, Keysight Technologies, Inc. (2016).

[32] *Keysight N4391A Optical Modulation Analyzer Measure with Confidence - Data Sheet*, Keysight Technologies, Inc. (2015).

[33] *Keysight Kalman Filter Based Estimation and Demodulation of Complex Signals – White Paper*, Keysight Technologies, Inc. (2014).

[34] M. Lu, "Integrated Optical Phase-locked Loops," University of California, Santa Barbara (2013).

[35] *Agilent Vector Signal Analysis Basics – Application Note*, Agilent Technologies, Inc. (2012).

[36] M. Gould, T. Baehr-Jones, R. Ding, and M. Hochberg, "Bandwidth enhancement of waveguide-coupled photodetectors with inductive gain peaking." *Optics Express* **20**(7), 7101-7111 (2012).

[37] J. Bowers and C. Burrus, "Ultrawide-band long-wavelength p-i-n photodetectors," *Journal of Lightwave Technology* **5**(10), 1339-1350 (1987).

[38] T. J. Maloney and J. Frey, "Transient and steady-state electron transport properties of GaAs and InP," *Polar* **12**(9.52), 0-043 (1977).

[39] R. S. Tuley and R. J. Nicholas, "Material parameters and device optimization: supplementary information for bandgap dependent thermophotovoltaic device performance using the InGaAs and InGaAsP material system," *Journal of Applied Physics* **108**(156018), (2010).

[40] M. Seimetz and C. M. Weinert, "Options, Feasibility, and Availability of 2× 4 90° Hybrids for Coherent Optical Systems," *Journal of Lightwave Technology* **24**(3), 1317- (2006).

[41] D. Hoffman, H. Heidrich, G. Wenke, R. Langenhorst, and E. Dietrich, "Integrated optics eight-port 90 degrees hybrid on $LiNbO_3$," *Journal of Lightwave Technology* **7**(5), 794-798 (1989).

[42] K. N. Nguyen, "Receiver and Regenerator Photonic Integrated Circuits for Coherent Optical Communications," University of California, Santa Barbara (2013).

[43] M. C. Larson, Y. A. Akulova, C. W. Coldren, T. Liljeberg, G. A. Fish, S. Nakagawa, A. Dahl, P. Kozodoy, D. Bingo, M. Bai, N. Ramdas, S. Penniman, T. Wipiejewski, and L. A. Coldren, "High performance widely-tunable SG-DBR lasers," in *Proc. SPIE* **4995**, pp. 66-80, International Society for Optics and Photonics, 2003.

[44] E. J. Skogen, "Quantum Well Intermixing for Wavelength-Agile Photonic Integrated Circuits," University of California, Santa Barbara (2003).

[45] M. L. Mašanović, "Wavelength-Agile Photonic Integrated Circuits for All-Optical Wavelength Conversion," University of California, Santa Barbara (2004).

[46] A. Alping, "Waveguide pin photodetectors: theoretical analysis and design criteria," *IEE Proceedings J - Optoelectronics* **136**(3), 177-182 (1989).

[47] F. Van Laere, T. Stomeo, D. Taillaert, G. Roelkens, D. Van Thourhout, T. F. Krauss, and R. Baets, "Efficient Polarization Diversity Grating Couplers in Bonded InP-Membrane," *IEEE Photonics Technology Letters* **20**(4), 318-320 (2008).

[48] D. Dai and J. E. Bowers, “Silicon-based on-chip multiplexing technologies and devices for Peta-bit optical interconnects,” *Nanophotonics* **3**(4-5), 283-311 (2014).

[49] P. Albrecht, M. Hamacher, H. Heidrich, D. Hoffmann, H. P. Nolting, and C. M. Weinert, "TE/TM mode splitters on InGaAsP/InP," *IEEE Photonics Technology Letters* **2**(2), 114-115 (1990).

[50] R. J. Deri, E. C. M. Pennings, A. Scherer, A. S. Gozdz, C. Caneau, N. C. Andreadakis, V. Shah, L. Curtis, R. J. Hawkins, J. B. D. Soole, and J. I. Song, "Ultracompact monolithic integration of balanced, polarization diversity photodetectors for coherent lightwave receivers," *IEEE Photonics Technology Letters* **4**(11), 1238-1240 (1992).

[51] F. Ghirardi, J. Brandon, M. Carre, A. Bruno, L. Menigaux, and A. Carenco, "Polarization splitter based on modal birefringence in InP/InGaAsP optical waveguides," *IEEE Photonics Technology Letters* **5**(9), 1047-1049 (1993).

[52] L. B. Soldano, A. I. de Vreede, M. K. Smit, B. H. Verbeek, E. G. Metaal, and F. H. Green, "Mach-Zehnder Interferometer Polarization Splitter in InGaAsP/InP," *IEEE Photonics Technology Letters* **6**(3), 402-405 (1994).

[53] J. J. G. M. Van der Tol, J. W. Pedersen, E. G. Metaal, J. J. W. Van Gaalen, Y. S. Oei, and F. H. Groen, "A short polarization splitter without metal overlays on InGaAsP-InP," *IEEE Photonics Technology Letters* **9**(2), 209-211 (1997).

[54] L. M. Augustin, J. J. G. M. Van der Tol, R. Hanfoug, W. J. M. De Laat, M. J. E. Van de Moosdijk, P. W. L. Van Dijk, Y. S. Oei, and M. K. Smit, "A Single Etch-Step Fabrication-Tolerant Polarization Splitter," *Journal of Lightwave Technology* **25**(3), 740-746 (2007).

[55] J. M. Hong, H. H. Ryu, S. R. Park, J. W. Jeong, S. G. Lee, E. H. Lee, S. G. Park, D. Woo, S. Kim, and B. H. O, "Design and fabrication of a significantly shortened multimode interference coupler for polarization splitter application," *IEEE Photonics Technology Letters* **15**(1), 72-74 (2003).

[56] H. El-Refaei, D. Yevick, and T. Jones, "Slanted-Rib Waveguide InGaAsP-InP Polarization Converters," *Journal of Lightwave Technology* **22**(5), 1352-1357 (2004).

[57] F. J. Duarte, *Tunable Laser Optics*, 2nd Edition, CRC, New York (2015).

[58] L. M. Augustin, J. J. G. M. van der Tol, E. J. Geluk, and M. K. Smit, "Short Polarization Converter Optimized for Active-Passive Integration in InGaAsP-InP," *IEEE Photonics Technology Letters* **19**(17/20), 1673-1675 (2007).

[59] F. H. Groen, Y. C. Zhu, and J. J. G. M. van der Tol, "Compact Polarisation Converter on InP/InGaAsP using an asymmetrical waveguide," in *11th European Conference on Integrated Optics (ECIO)*, pp. 141-144, Czech Technical University in Prague, 2003.

[60] A. Sivananthan, "Integrated Linewidth Reduction of Rapidly Tunable Semiconductor Lasers," University of California, Santa Barbara (2013).

[61] M. Larson, Y. Feng, P. C. Koh, X. D. Huang, M. Moewe, A. Semakov, A. Patwardhan, E. Chiu, A. Bhardwaj, K. Chan, J. Lu, S. Bajwa, and K. Duncan, "Narrow linewidth high power thermally tuned sampled-grating distributed Bragg reflector laser," in *Optical Fiber Communication Conference/National Fiber Optic Engineers Conference*, p. OTh3I-4, Optical Society of America, 2013.

[62] M. K. Smit and C. Van Dam, "PHASAR-Based WDM-Devices: Principles, Design and Applications," *IEEE Journal of Selected Topics in Quantum Electronics*, **2**(2), 236-250 (1996).

[63] S. C. Nicholes, "Large-Scale Photonic Integration for Advanced All-Optical Routing Functions," University of California, Santa Barbara (2009).

[64] J. F. Bauters, M. J. R. Heck, D. John, D. Dai, M. C. Tien, J. S. Barton, A. Leinse, R. G. Heideman, D. J. Blumenthal, and J. E. Bowers, "Ultra-low-loss high-aspect-ratio Si_3N_4 waveguides," *Optics Express* **19**(4), 3163-3174 (2011).

[65] M. Belt and D. J. Blumenthal, "Erbium-doped waveguide DBR and DFB laser arrays integrated within an ultra-low-loss $Si_3 N_4$ platform," *Optics Express* **22**(9), 10655-10660 (2014).

[66] L. A. Coldren, S. C. Nicholes, L. Johansson, S. Ristic, R. S. Guzzon, E. J. Norberg, and U. Krishnamachari, "High Performance InP-Based Photonic ICs—A Tutorial," *Journal of Lightwave Technology* **29**(4), 554-570 (2011).

[67] T. Komljenovic, M. Davenport, J. Hulme, A. Y. Liu, C. T. Santis, A. Spott, S. Srinivasan, E. J. Stanton, C. Zhang, and J. E. Bowers, "Heterogeneous Silicon Photonic Integrated Circuits," *Journal of Lightwave Technology* **34**(1), 20-35 (2016).

[68] A. W. Fang, H. Park, O. Cohen, R. Jones, M. J. Paniccia, and J. E. Bowers, "Electrically pumped hybrid AlGaInAs-silicon evanescent laser," *Optics Express* **14**(20), 9203-9210 (2006).

[69] B. Mason, J. Barton, G. A. Fish, L. A. Coldren, and S. P. Denbaars, "Design of sampled grating DBR lasers with integrated semiconductor optical amplifiers," *IEEE Photonics Technology Letters* **12**(7), 762-764 (2000).

[70] J. S. Parker, "Integrated Photonic Comb Generation: Applications in Coherent Communication and Sensing," University of California, Santa Barbara (2012).

[71] J. W. Raring, "Advanced Indium Phosphide Based Monolithic Integration using Quantum Well Intermixing and MOCVD Regrowth," University of California, Santa Barbara (2006).

[72] V. Lal, "Monolithic Wavelength Converters for High-Speed Packet Switched Optical Networks," University of California, Santa Barbara (2006).

[73] M. Silver and E. P. O'Rielly, "Optimization of long wavelength InGaAsP strained quantum-well lasers," *IEEE Journal of Quantum Electronics* **31**(7), 1193–1200 (1995).

[74] J. S. Parker, E. J. Norberg, R. S. Guzzon, S. C. Nicholes, and L. A. Coldren, "High verticality InP/InGaAsP etching in $Cl_2/H_2/Ar$ inductively coupled plasma for photonic integrated circuits," *Journal of Vacuum Science and Technology B* **29**(1), 011016-(1-5) (2011).

[75] R. A. Powell, *Dry etching for microelectronics*, Elsevier Science Publishers (1984).

[76] D. H. van Dorp, S. Arnauts, D. Cuypers, J. Rip, F. Holsteyns, S. De Gendt, and J. J. Kelly, "Nanoscale Etching of $In_{0.53}Ga_{0.47}As$ in H_2O_2/HCl Solutions for Advanced CMOS Processing," *ECS Journal of Solid State Science and Technology* **3**(6), 179-184 (2014).

[77] J. S. Yu, S. H. Kim, and T. I. Kim, "PtTiPtAu and PdTiPtAu ohmic contacts to p-InGaAs," in *1997 IEEE International Symposium on Compound Semiconductors*, pp. 175-178, IEEE, 1997.

[78] P. J. Skahan, S. Gundavarapu, K. N. Nguyen, D. M. Baney, and D. J. Blumenthal, “Monolithically integrated dual-channel coherent receiver with widely tunable local oscillator for 100 Gbps dual-polarization quadrature phase shift keying applications,” *Optics Letters* **40**(18), 4313-4316 (2015). DOI: 10.1364/OL.40.004313

[79] A. Shutler, “Investigation of Propagation Loss of Passive Silicon Waveguides Using Two Different Etching Techniques,” *2008 NNIN REU Research Accomplishments*, 114-115 (2008).

[80] J. A. Summers, “Monolithic Multi-Stage Wavelength Converters for Wavelength-Agile Photonic Integration,” University of California, Santa Barbara (2007).

[81] T. N. Huynh, L. Nguyen, K. Shi, and L. P. Barry, "Coherent Phase Modulation Detection for Self-Heterodyne Phase Noise Measurement," in *Proceedings of SPIE* **8309**, p. 830920, Optical Society of America, 2011.

[82] S. Nakagawa, G. A. Fish, A. Dahl, P. C. Koh, C. Schow, M. Mack, L. Wang, and R. C. Yu, "Phase Noise of Widely-Tunable SG-DBR Laser," in *Optical Fiber Communication Conference*, p. ThF2, Optical Society of America, 2003.

---

[83] L. A. Coldren, S. W. Corzine, and M. L. Mashanovitch, *Diode Lasers and Photonic Integrated Circuits*, 2nd edition, John Wiley & Sons, Inc. (2012).

Appendix A

MATLAB Code for Grating Model of SG-DBR Front and Back Mirrors

The following MATLAB code was originally developed by Michael Belt to use T-matrices to simulate the transmission and reflectivity of DFB grating mirrors. It was further adapted to simulate the reflectivity of the front and back mirrors for the SG-DBR laser used in the receiver and all-optical switch presented in this dissertation. Theory behind the T-matrix model of DFB mirrors may be found in [83].

```
%Michael Belt
%4-30-14
%Grating T-Matrix Code
%Calculate transmission and reflection spectra of a grating using T-matrix
%formalism
%All units in m unless otherwise noted
clear all
close all
clc
%Simulation Design Parameters
Bragglambda = 1540*(1e-9); %Bragg wavelength
L1 = 178*(1e-9); %half period length (notch section)
L2 = 58*(1e-9); %half period length (wider section)
biglambda = L1 + L2; %full period length
neff = 3.2627; %effective index of the grating
alphadBm = 0; %assumed grating loss in dB/m
```

```
alpha = alphadBm/(10*log10(exp(1))); %assumed grating loss in 1/m
tuning1 = -0.00;
tuning2 = -0.00;
totallength1 = 3.54e-6; %total grating length for mirror 1 = Lgf
totallength2 = 5.9e-6; %total grating length for mirror 2 = Lgb
cavitylength = 690.2e-6; %total cavity length between mirrors 1 and 2 = Lc
samplelength1 = 87.26e-6; %length of sampled section for mirror 1 = L1
samplelength2 = 93.7e-6; %length of sampled section for mirror 2 = L2
numfrontbursts = 6; %Number of repeating bursts (mirror + sampling length) for
front mirror
numbackbursts = 10; %Number of repeating bursts (mirror + sampling length)
for back mirror
kappacm1 = 338; %coupling constant in cm-1 for mirror 1
kappa1 = kappacm1.*100;%coupling constant in m-1 for mirror 1
kappacm2 = kappacm1; %coupling constant in cm-1 for mirror 2
kappa2 = kappacm2.*100;%coupling constant in m-1 for mirror 2
%Simulation Functional Parameters
%Coldren Chapter 3, page 116
%Loop where calculations are performed wavelength by wavelength
numpoints = 16001; %number of data points
lambda = (1e-9)*linspace(1490,1590,numpoints); %wavelength
m1 = floor(totallength1/biglambda);
m2 = floor(totallength2/biglambda);
for k = 1:length(lambda)
   for n = 1:length(kappacm1)
      effectivelength1(n) = (1./(2.*kappa1(n))).*tanh(kappa1(n).*totallength1);
%effective grating length for mirror 1
      effectivelength2(n) = (1./(2.*kappa2(n))).*tanh(kappa2(n).*totallength2);
%effective grating length for mirror 2

      deltan1(n) = [0.028]; %index difference for mirror 1 Coldren Chapter 3 page
121
      deltan2(n) = [0.028]; %index difference for mirror 1 Coldren Chapter 3 page
121
      %Propagation Constants
      %Propagation Constant at the Bragg Wavelength
```

```
    beta(k) = (2*pi.*neff)./(lambda(k)); %propagation constant at all wavelengths (assume 0 disperion so that n(lambda) = n(Bragg))
    beta0 = (2*pi.*neff)./(Bragglambda); %propagation constant at Bragg wavelength
    delta(k) = beta(k) - beta0; %detuning parameter
    %Index Values for Mirror 1
    n1k1(n,k) = neff + tuning1 - deltan1(n)/2; %assumed index of notch section using index difference from fitted Kappa value
    beta1k1(n,k) = ((2*pi.*n1k1(n,k))./(lambda(k))) - 1j.*alpha./2; %assumed propagation constant of notch section with loss
    n2k1(n,k) = neff + tuning1 + deltan1(n)/2; %assumed index of wider section using index difference from fitted Kappa value
    beta2k1(n,k) = ((2*pi.*n2k1(n,k))./(lambda(k))) - 1j.*alpha./2; %assumed propagation constant of wider section with loss
    rk1(n,k) = -(n1k1(n,k) - n2k1(n,k))./(n1k1(n,k) + n2k1(n,k)); %field reflection coefficient
    tk1(n,k) = sqrt(1-(rk1(n,k).^2)); %field transmission coefficient
    %Index Values for Mirror 2
    n1k2(n,k) = neff + tuning2 - deltan2(n)/2; %assumed index of notch section using index difference from fitted Kappa value
    beta1k2(n,k) = ((2*pi.*n1k2(n,k))./(lambda(k))) - 1j.*alpha./2; %assumed propagation constant of notch section with loss
    n2k2(n,k) = neff + tuning2 + deltan2(n)/2; %assumed index of wider section using index difference from fitted Kappa value
    beta2k2(n,k) = ((2*pi.*n2k2(n,k))./(lambda(k))) - 1j.*alpha./2; %assumed propagation constant of wider section with loss
    rk2(n,k) = -(n1k2(n,k) - n2k2(n,k))./(n1k2(n,k) + n2k2(n,k)); %field reflection coefficient
    tk2(n,k) = sqrt(1-(rk2(n,k).^2)); %field transmission coefficient
    %Phase terms phiplus and phiminus are:
    phiplusk1(n,k) = beta1k1(n,k).*L1 + beta2k1(n,k).*L2; %positive phase term
    phiplusk2(n,k) = beta1k2(n,k).*L1 + beta2k2(n,k).*L2; %positive phase term
    phiminusk1(n,k) = beta1k1(n,k).*L1 - beta2k1(n,k).*L2; %negative phase term
    phiminusk2(n,k) = beta1k2(n,k).*L1 - beta2k2(n,k).*L2; %negative phase term
    %T Matrix Segments for Grating 1
```

```
    T11k1(n,k) = (1./(tk1(n,k).^2)).*( exp(1j.*phiplusk1(n,k)) - (rk1(n,k).^2).*exp(-1j.*phiminusk1(n,k)) );
    T21k1(n,k) = (rk1(n,k)./(tk1(n,k).^2)).*( exp(1j.*phiplusk1(n,k)) - exp(-1j.*phiminusk1(n,k)) );
    T12k1(n,k) = (rk1(n,k)./(tk1(n,k).^2)).*( exp(-1j.*phiplusk1(n,k)) - exp(1j.*phiminusk1(n,k)) );
    T22k1(n,k) = (1./(tk1(n,k).^2)).*( exp(-1j.*phiplusk1(n,k)) - (rk1(n,k).^2).*exp(1j.*phiminusk1(n,k)) );
    %Entire Grating 1 T Matrix
    Tgk1 = [T11k1(n,k) T12k1(n,k); T21k1(n,k) T22k1(n,k)]^m1;
    %Grating 1 T Matrix Individual Portions
    Tg11k1(n,k) = Tgk1(1,1);
    Tg21k1(n,k) = Tgk1(2,1);
    Tg12k1(n,k) = Tgk1(1,2);
    Tg22k1(n,k) = Tgk1(2,2);
    %T Matrix Segments for Grating 2
    T11k2(n,k) = (1./(tk2(n,k).^2)).*( exp(1j.*phiplusk2(n,k)) - (rk2(n,k).^2).*exp(-1j.*phiminusk2(n,k)) );
    T21k2(n,k) = (rk2(n,k)./(tk2(n,k).^2)).*( exp(1j.*phiplusk2(n,k)) - exp(-1j.*phiminusk2(n,k)) );
    T12k2(n,k) = (rk2(n,k)./(tk2(n,k).^2)).*( exp(-1j.*phiplusk2(n,k)) - exp(1j.*phiminusk2(n,k)) );
    T22k2(n,k) = (1./(tk2(n,k).^2)).*( exp(-1j.*phiplusk2(n,k)) - (rk2(n,k).^2).*exp(1j.*phiminusk2(n,k)) );
    %Entire Grating 2 T Matrix
    Tgk2 = [T11k2(n,k) T12k2(n,k); T21k2(n,k) T22k2(n,k)]^m2;
    %Grating 2 T Matrix Individual Portions
    Tg11k2(n,k) = Tgk2(1,1);
    Tg21k2(n,k) = Tgk2(2,1);
    Tg12k2(n,k) = Tgk2(1,2);
    Tg22k2(n,k) = Tgk2(2,2);
    %T Matrix Segments for Cavity Section
    TCavity11(n,k) = exp(1j.*beta2k1(n,k).*(cavitylength));
    TCavity21(n,k) = 0;
    TCavity12(n,k) = 0;
    TCavity22(n,k) = exp(-1j.*beta2k1(n,k).*(cavitylength));
    %Entire Cavity Section T Matrix
```

```
    TCavity = [TCavity11(n,k) TCavity12(n,k); TCavity21(n,k) TCavity22(n,k)];
    %T Matrix Segments for Sample Length 1 Section
    TSample111(n,k) = exp(1j.*beta2k1(n,k).*(samplelength1));
    TSample121(n,k) = 0;
    TSample112(n,k) = 0;
    TSample122(n,k) = exp(-1j.*beta2k1(n,k).*(samplelength1));

    %Entire Sample Length 1 Section T Matrix
    TSample1 = [TSample111(n,k) TSample112(n,k); TSample121(n,k) TSample122(n,k)];
    %T Matrix Segments for Sample Length 2 Section
    TSample211(n,k) = exp(1j.*beta2k1(n,k).*(samplelength2));
    TSample221(n,k) = 0;
    TSample212(n,k) = 0;
    TSample222(n,k) = exp(-1j.*beta2k1(n,k).*(samplelength2));
    %Entire Sample Length 1 Section T Matrix
    TSample2 = [TSample211(n,k) TSample212(n,k); TSample221(n,k) TSample222(n,k)];
    %-----Cavity Structure-----%
    %I know it's for a SG-DBR, but leave the variable as TDFB to save work
    %Start at front mirror when entering cavity sections
    TDFB = ((Tgk1*TSample1)^(numfrontbursts-1));
    TDFB2 = ((Tgk2*TSample2)^(numbackbursts-1))*Tgk2;
    %DFB T Matrix Individual Portions
    TDFB11(n,k) = TDFB(1,1);
    TDFB21(n,k) = TDFB(2,1);
    TDFB12(n,k) = TDFB(1,2);
    TDFB22(n,k) = TDFB(2,2);
    %Grating 1 S Matrix Individual Portions
    Sg11k1(n,k) = (1./(Tg11k1(n,k))).*Tg21k1(n,k);
    Sg21k1(n,k) = (1./(Tg11k1(n,k))).*1;
    Sg12k1(n,k) = (1./(Tg11k1(n,k))).*det(Tgk1);
    Sg22k1(n,k) = (1./(Tg11k1(n,k))).*(-1.*Tg12k1(n,k));
    %Grating 2 S Matrix Individual Portions
    Sg11k2(n,k) = (1./(Tg11k2(n,k))).*Tg21k2(n,k);
    Sg21k2(n,k) = (1./(Tg11k2(n,k))).*1;
    Sg12k2(n,k) = (1./(Tg11k2(n,k))).*det(Tgk2);
```

```
Sg22k2(n,k) = (1./(Tg11k2(n,k))).*(-1.*Tg12k2(n,k));
%Entire DFB S Matrix Individual Portions
SDFB11(n,k) = (1./(TDFB11(n,k))).*TDFB21(n,k);
SDFB21(n,k) = (1./(TDFB11(n,k))).*1;
SDFB12(n,k) = (1./(TDFB11(n,k))).*1;
SDFB22(n,k) = (1./(TDFB11(n,k))).*(-1.*TDFB12(n,k));
%Grating 1 Reflection and Transmission Spectra
GratingReflectk1Mag(n,k) = Sg11k1(n,k).*conj(Sg11k1(n,k));
GratingTransk1Mag(n,k) = Sg21k1(n,k).*conj(Sg21k1(n,k));
%Grating 2 Reflection and Transmission Spectra
GratingReflectk2Mag(n,k) = Sg11k2(n,k).*conj(Sg11k2(n,k));
GratingTransk2Mag(n,k) = Sg21k2(n,k).*conj(Sg21k2(n,k));
%DFB Reflection and Transmission Spectra
DFBReflectMag1(n,k) = SDFB11(n,k).*conj(SDFB11(n,k));
DFBTransMag(n,k) = SDFB21(n,k).*conj(SDFB21(n,k));
TDFB11(n,k) = TDFB2(1,1);
TDFB21(n,k) = TDFB2(2,1);
TDFB12(n,k) = TDFB2(1,2);
TDFB22(n,k) = TDFB2(2,2);
%Grating 1 S Matrix Individual Portions
Sg11k1(n,k) = (1./(Tg11k1(n,k))).*Tg21k1(n,k);
Sg21k1(n,k) = (1./(Tg11k1(n,k))).*1;
Sg12k1(n,k) = (1./(Tg11k1(n,k))).*det(Tgk1);
Sg22k1(n,k) = (1./(Tg11k1(n,k))).*(-1.*Tg12k1(n,k));
%Grating 2 S Matrix Individual Portions
Sg11k2(n,k) = (1./(Tg11k2(n,k))).*Tg21k2(n,k);
Sg21k2(n,k) = (1./(Tg11k2(n,k))).*1;
Sg12k2(n,k) = (1./(Tg11k2(n,k))).*det(Tgk2);
Sg22k2(n,k) = (1./(Tg11k2(n,k))).*(-1.*Tg12k2(n,k));

%Entire DFB S Matrix Individual Portions
SDFB11(n,k) = (1./(TDFB11(n,k))).*TDFB21(n,k);
SDFB21(n,k) = (1./(TDFB11(n,k))).*1;
SDFB12(n,k) = (1./(TDFB11(n,k))).*1;
SDFB22(n,k) = (1./(TDFB11(n,k))).*(-1.*TDFB12(n,k));
%Grating 1 Reflection and Transmission Spectra
GratingReflectk1Mag(n,k) = Sg11k1(n,k).*conj(Sg11k1(n,k));
```

```
        GratingTransk1Mag(n,k) = Sg21k1(n,k).*conj(Sg21k1(n,k));
        %Grating 2 Reflection and Transmission Spectra
        GratingReflectk2Mag(n,k) = Sg11k2(n,k).*conj(Sg11k2(n,k));
        GratingTransk2Mag(n,k) = Sg21k2(n,k).*conj(Sg21k2(n,k));
        %DFB Reflection and Transmission Spectra
        DFBReflectMag2(n,k) = SDFB11(n,k).*conj(SDFB11(n,k));
        DFBTransMag(n,k) = SDFB21(n,k).*conj(SDFB21(n,k));

    end
end
%Plotting
color = colormap(cool(length(kappacm1)));
for n = 1:length(kappacm1)
    Fig1 = figure(1);
    set(gca, 'FontSize', 24)
    xlabel('Wavelength (nm)', 'FontSize', 32)
    ylabel('Reflection', 'FontSize', 32)
    xlim([1490 1590])
    grid on
    hold all
    plot(lambda*(1e9),((DFBReflectMag2(n,:))),'r','Linewidth',3)
    plot(lambda*(1e9),((DFBReflectMag1(n,:))),'k','Linewidth',3)
    set(Fig1,'Position',[1700 150 1280 800])
end
```

Appendix B

MATLAB Code for Circuit Response Model of a Waveguide Photodiode

The following MATLAB code was developed to model the bandwidth of the waveguide photodiode using the equations found in Section 2.6. This was used to determine the required parameters for the elements of the photodiode circuit to meet a 30 GHz operating bandwidth.

```
numpoints = 1e3; %number of data points
w = linspace(0 ,2500*10^9, numpoints); %frequency
f = w./2./pi;
r_load = 50;
r_contact = 30;
l_wire = 0.05*10^-9;
c_pad = 8*10^-15;
c_diode = 10*10^-15;
x = (r_load./1i./w./c_pad)./(r_load + 1./1i./w./c_pad);
v_out=-
w.^2.*l_wire.*c_pad+1i.*w.*c_pad.*r_load+(1+1i.*w.*c_diode.*r_contact)./(1+c_di
ode./c_pad + 1i.*w.*c_diode.*r_contact);
v_out = 1./v_out;
x = (1./1i./w./c_diode./(r_contact + r_load + 1./1i./w./c_diode));
y = (r_load + 1i.*w.*l_wire)./r_load;
z=r_load.*c_diode./(r_load.*c_diode+r_load.*c_pad+1i.*w.*(r_contact.*c_pad.*c_di
ode + c_diode.*l_wire + c_pad) - w.^2*r_contact.*c_pad.*c_diode.*l_wire);
 10*log10(abs(v_out(2)))
hold all;
plot(f./10.^9, 10*log10(abs(v_out/v_out(2))));
```